NUMERICAL STUDIES IN ONE AND INFINITE DIMENSIONAL QUANTUM SYSTEMS

BY SRIVENKATESWARA SARMA KANCHARLA

A dissertation submitted to the
Graduate School—New Brunswick
Rutgers, The State University of New Jersey
in partial fulfillment of the requirements
for the degree of
Doctor of Philosophy
Graduate Program in Physics and Astronomy
Written under the direction of
Professor Gabriel B. Kotliar
and approved by

New Brunswick, New Jersey
Oct, 2002

ABSTRACT OF THE DISSERTATION

Numerical studies in one and infinite dimensional quantum systems

by Srivenkateswara Sarma Kancharla

Dissertation Director: Professor Gabriel B. Kotliar

The interplay between interactions and dimensionality is an important issue for strongly correlated electronic materials and is central to this thesis. We present insights that have been obtained into the optical response, charge gap and excitonic behavior in one-dimensional Mott insulators utilizing the density matrix renormalization group (DMRG) method. We show how a Mott-Hubbard exciton, a bound state between a double occupancy and an empty site in a background of singly occupied sites, can be formed due to a nearest-neighbor Coulomb repulsion V within the one-dimensional Hubbard model. The interaction not only binds the exciton, but also renormalizes the spectral gap and strongly couples the exciton to other electrons. We show that this leads to a non-monotonic behavior of the excitonic properties as a function of V, and eventually to a charge-density wave instability. The excitonic binding energy is comparable to the optical gap itself making the problem non-perturbative. This should be contrasted with excitons in conventional band insulators which exhibit a monotonic behavior as a function of Coulomb repulsion.

Next, we consider the limit of infinite dimensionality, in particular, the cellular dynamical mean field theory (CDMFT), wherein clusters of sites are embedded in

ii

a self-consistent medium. This method incorporates short range correlations and k-dependence of the self energy which are missing in the original single impurity DMFT. We solve the CDMFT self-consistent equations in the worst case scenario, viz., the one-dimensional extended Hubbard model using the exact diagonalization method. We compare with DMRG and find that even the smallest cluster sizes provide an accurate description of the onsite correlations, while the offsite quantities improve systematically with increasing cluster size. We also extend the CDMFT equations to describe broken symmetry and investigate the convergence as a function of bath size for clusters of different sizes.

Lastly, we observe that both DMRG and CDMFT involve the embedding of a finite size system in a larger one to describe the smaller system as part of a large or infinite lattice. Based on this, we propose a new approach that blends the CDMFT and DMRG ideas to perform calculations for realistic systems in two and three dimensions.

Acknowledgements

I am grateful to my advisor, Gabi Kotliar, for his patience and valuable guidance over these years.

Special thanks go to my friend and collaborator Carlos Bolech with whom were spent many long nights discussing and chatting.

I also thank Gunnar Palsson for sharing his knowledge on computing and Harald Jeshcke for a careful reading of the manuscript.

Dedication

To memories that don't ever leave me

Table of Contents

A٦	ostra	ct	ii
A	knov	wledgements	iv
De	edica	tion	v
Li	st of	Figures	ix
1.	Nur	merical Methods - From brute force to RG	1
	1.1.	Introduction	1
	1.2.	Numerical Quantum Many Body Methods	1
		1.2.1. The Lanczos method	3
	1.3.	The Numerical Renormalization Group (NRG) method	6
	1.4.	Failure of NRG for 1D Lattice models: Free particle on a chain	8
	1.5.	The Density Matrix Renormalization Group (DMRG) method	10
		1.5.1. Infinite Chain Algorithm	14
		1.5.2. Finite Chain Algorithm	15
	1.6.	Dynamical Correlation Functions using DMRG	18
		1.6.1. Lanczos vector method	20
		1.6.2. Correction vector method	21
	1.7.	Extension to two dimensions	23
2.	Opt	ical response and excitons in one dimensional Mott insulators .	26
	2.1.	Introduction	26
	2.2.	Wannier and Mott Excitons	26
	2.3.	Model Hamiltonian	27
	2.4.	Phase diagram	29

	3.2.	Introduction	42
	3.3.	The routines	43
4.	The	Dynamical Mean Field Method	50
		Introduction	50
	4.2.	Classical spin models	50
	4.3.	Itinerant quantum mechanical models	51
	4.4.	Local self energy	52
	4.5.	Impurity model parametrization and Exact Diagonalization algorithm .	55
	4.6.	Limitations of single impurity approach	56
5.	Cell	ular Dynamical Mean Field Theory for the Hubbard Model	59
5.	Cell 5.1.	ular Dynamical Mean Field Theory for the Hubbard Model Introduction	
5.		·	59
5.	5.1.	Introduction	59 59
5.	5.1.	Introduction	59 59 60 61
5.	5.1.	Introduction	59 59 60 61
5.	5.1.	Introduction	59 59 60 61 63
5.	5.1. 5.2.	Introduction	59 59 60 61 63
5.	5.1.5.2.5.3.	Introduction	599 599 600 611 633 644 666
5.	5.1.5.2.5.3.5.4.5.5.	$ \begin{array}{cccccccccccccccccccccccccccccccccccc$	599 600 611 633 644 666
	5.1.5.2.5.3.5.4.5.5.5.6.	$ \begin{array}{cccccccccccccccccccccccccccccccccccc$	59 59 60 61 63 64 66 67 72

References	90
Vita	95

List of Figures

1.1.	To remove the kink, one needs to keep almost all the states in each block	10
1.2.	One full sweep of the finite size algorithm	17
1.3.	A 2D DMRG algorithm obtained by mapping onto a 1D lattice	23
2.1.	Local spectral functions for different values of the coupling V . Note the	
	abrupt change in particle–hole symmetry between the two phases	32
2.2.	Optical and Raman response functions for different values of the coupling	
	V. The vertical dotted line indicates the magnitude of the single–particle	
	spectral gap in each case	33
2.3.	Excitonic weight as a function of the coupling V	34
2.4.	Gaps for different values of the coupling V	35
4.1.	Collapse of the second order contribution to the irreducible self energy in	
	the limit $d \to \infty$	53
4.2.	Only the Hartree contribution survives the limit $d \to \infty$ for near neighbor	
	Coulomb repulsion	57
5.1.	A schematic illustration of the cluster dynamical mean field algorithm .	66
5.2.	Spectral gap as a function of U/t for the half filled Hubbard model	68
5.3.	Imaginary part of the onsite Green's function (left column) and real part	
	of the nearest neighbor Green's function (right column) on the Matsubara	
	axis for different values of U (in units of t)	69
5.4.	Deviation of LISA and CDMFT Green's functions from the DMRG re-	
	sults as a function of the bath size N_b	70
5.5.	From left to right we show the local spectral functions for sites one	
	through three in a cluster of size $N_c=3$ with $U=12t$. The bath	
	size is fixed at $N_b = 6$	71

5.6.	Imaginary part of the onsite Green's function (left column) and real part	
	of the nearest neighbor Green's function (right column) on the Matsubara	
	axis for different values of V in the SDW phase	73
5.7.	Real part of the onsite Green's function in the CDW phase	74
5.8.	Imaginary part of the onsite Green's function in the CDW phase	74
5.9.	Real part of the nearest neighbor Green's function in the CDW phase	75
5.10.	Schematic representation of an RG procedure intended to reach large	
	cluster sizes	76

Chapter 1

Numerical Methods - From brute force to RG

1.1 Introduction

Strongly correlated electronic systems, typified by materials such as heavy fermion compounds, high temperature superconductors and manganates, amongst several others, continue to challenge existing methods in many body physics. Except for special cases, controlled analytical approaches are scarcely available. In the physically interesting parameter regime these systems do not have a suitable small parameter and therefore perturbative treatments are largely inappropriate. Although mean field approaches have yielded a wealth of information, their role is limited by the fact that many of the materials are characterized by low dimensionality and strong fluctuations. The aforesaid challenges have stimulated huge advances in the development and use of computational methods for strongly correlated systems.

1.2 Numerical Quantum Many Body Methods

Amongst the numerical methods available to study quantum models for correlated electrons, the least sophisticated approach is the exact diagonalization method (see [1] for a review). In this method, the Hamiltonian for a finite sized cluster, along with the operators of interest, are represented by a matrix. Using a special basis such as the Lanczos basis, it is possible to obtain with large precision the ground state wavefunction, energy and other expectation values of interest. A recursion procedure permits access to dynamical correlation functions as well. In order to investigate finite temperature properties, one can diagonalize the Hamiltonian matrix in full using numerical library routines. The primary constraint in applying matrix methods such as the above

on a computer to study many body Hamiltonians is the exponentially increasing sizes of the Hilbert space as the cluster size increases. This, combined with the finite precision available, drastically reduces the sizes that can be dealt with.

For example, the size of the Hilbert space for a Hubbard model (with four states per site, viz., $|0\rangle,|\uparrow\rangle$, $|\downarrow\rangle$ and $|\uparrow\downarrow\rangle$) on a finite cluster of N_s sites scales as 4^{N_s} . It is easy to see that the associated memory requirements and CPU time are enormous even for a two dimensional lattice of size $N_s=4\times 4$. The matrix sizes can be reduced by invoking symmetries specific to the Hamiltonian and the boundary conditions. The symmetries range from the obvious ones such as the number of particles and S_{total}^z , to more involved ones (in terms of implementation) such as translational invariance, spin inversion, rotation about a lattice site for square lattices, reflections with respect to the lattice axes and so on. Another circumstance which is often exploited to advantage, is the sparseness of matrices when operators are expressed in the local basis. Memory requirements are relaxed, because only the non-zero matrix elements are stored. In efficient exact diagonalization programs, the Hamiltonian matrix is usually not explicitly generated. Instead, a procedure to multiply a vector by H is used which generates the Hamiltonian matrix elements as they are needed. Inspite of the exploitation of symmetries and sparsity, full diagonalization of the Hamiltonian to get finite temperature properties, except for very small system sizes, is beyond the reach of present day computers and algorithms. Therefore, the term exact diagonalization refers largely to the use of the Lanczos technique to deal with ground state properties and zero temperature correlations.

Apart from direct applications to the study of model Hamiltonians, the exact diagonalization approach has proved valuable in conjunction with another non-perturbative method, namely, the Dynamical Mean Field theory [2]. We shall discuss this in detail in chapter 4. Exact diagonalization is also a valuable tool aiding comparative studies of analytic approximation schemes and development of new methods.

1.2.1 The Lanczos method

The basic idea behind this method is that a special basis can be chosen where the Hamiltonian has a tridiagonal representation [3]. The iterative procedure starts with selecting a normalized random vector $|\phi_0\rangle$ in the Hilbert space of the model Hamiltonian. This choice is made in order to have a non-zero overlap between the actual ground state $|\phi_0\rangle$, and the initial state $|\phi_0\rangle$.

We then define a new vector by applying the Hamiltonian \hat{H} to $|\phi_0\rangle$ and subtracting the projection over $|\phi_0\rangle$,

$$|\phi_1\rangle = \hat{H}|\phi_0\rangle - \frac{\langle\phi_0|\hat{H}|\phi_0\rangle}{\langle\phi_0|\phi_0\rangle}|\phi_0\rangle, \tag{1.1}$$

Clearly, $\langle \phi_0 | \phi_1 \rangle = 0$. We can further build a state that is orthogonal to both $|\phi_0\rangle$ and $|\phi_1\rangle$ using,

$$|\phi_2\rangle = \hat{H}|\phi_1\rangle - \frac{\langle\phi_1|\hat{H}|\phi_1\rangle}{\langle\phi_1|\phi_1\rangle}|\phi_1\rangle - \frac{\langle\phi_1|\phi_1\rangle}{\langle\phi_0|\phi_0\rangle}|\phi_0\rangle. \tag{1.2}$$

This procedure can be generalized to obtain the following orthogonal basis recursively,

$$|\phi_{n+1}\rangle = \hat{H}|\phi_n\rangle - a_n|\phi_n\rangle - b_n^2|\phi_{n-1}\rangle,\tag{1.3}$$

where $n = 0, 1, 2, \dots$, and the coefficients a_n and b_n are given by

$$a_n = \frac{\langle \phi_n | \hat{H} | \phi_n \rangle}{\langle \phi_n | \phi_n \rangle}, \qquad b_n^2 = \frac{\langle \phi_n | \phi_n \rangle}{\langle \phi_{n-1} | \phi_{n-1} \rangle}.$$
 (1.4)

In this basis, it can be shown that the Hamiltonian matrix becomes tridiagonal,

$$H = \begin{pmatrix} a_0 & b_1 & 0 & 0 & \cdots \\ b_1 & a_1 & b_2 & 0 & \cdots \\ 0 & b_2 & a_2 & b_3 & \cdots \\ 0 & 0 & b_3 & a_3 & \cdots \\ \vdots & \vdots & \vdots & \vdots & \ddots \end{pmatrix}$$
 (1.5)

Once in this form, the matrix can be diagonalized easily using standard library routines. However, it is impractical to completely diagonalize the model being studied on a finite cluster by performing Lanczos iterations equal to the size of the Hilbert space. The key advantage of this technique is that sufficiently accurate information about the ground

state of the problem can be obtained after a small number of iterations (typically of the order of ~ 100 or less). Thus the method is suitable for the analysis of low temperature properties of the models of correlated electrons.

The most remarkable feature of the Lanczos method is that, apart from the groundstate eigenvalues and eigenvectors, it provides accurate information about the dynamical correlation functions for the given finite size system [4]. We define the zero temperature correlation function for an operator \hat{O} as:

$$C_{\hat{O}}(t-t') = \langle \psi_0 | \hat{O}^{\dagger}(t) \hat{O}(t') | \psi_0 \rangle \tag{1.6}$$

The spectral function associated with this correlation is often related to an experimental observable. It's Fourier transform in frequency space is given by,

$$I(\omega) = -\frac{1}{\pi} \text{Im}[\langle \psi_0 | \hat{O}^{\dagger} \frac{1}{\omega + E_0 + i\epsilon - \hat{H}} \hat{O} | \psi_0 \rangle]. \tag{1.7}$$

 $|\psi_0\rangle$ and E_0 are the ground state eigenvector and eigenvalue of the Hamiltonian \hat{H} , respectively. ω is the frequency, and ϵ is a small real number introduced in the calculation to shift the poles of the Green's function into the complex plane. Introducing a complete set of basis states, and using the well-known distribution property, $\frac{1}{x+i\epsilon} = P(\frac{1}{x}) - i\pi\delta(x)$, we obtain

$$I(\omega) = \sum_{n} |\langle \psi_n | \hat{O} | \psi_0 \rangle|^2 \delta(\omega - (E_n - E_0)). \tag{1.8}$$

Here, $|\psi_n\rangle$ are eigenvectors of the Hamiltonian with eigenvalues E_n . In practice, the δ -functions are smeared by a finite ϵ , i.e., they are replaced by Lorentzians according to $\delta(x) \to \frac{1}{\pi} \frac{\epsilon}{x^2 + \epsilon^2}$.

In order to numerically evaluate Eq. 1.7, it is convenient to write the Hamiltonian matrix in a special basis. As before, we will apply the Lanczos method to write \hat{H} in a tridiagonal form but instead of starting the iterations with a random state, we choose

$$|\phi_0\rangle = \frac{\hat{O}|\psi_0\rangle}{\sqrt{\langle\psi_0|\hat{O}^{\dagger}\hat{O}|\psi_0\rangle}}.$$
(1.9)

Consider the matrix $(z - \hat{H})$ and the identity $(z - \hat{H})(z - \hat{H})^{-1} = I$, where $z = \omega + E_0 + i\epsilon$. This identity can be decomposed in the Lanczos basis $\{|\phi_n\rangle\}$, with $|\phi_0\rangle$ as given by Eq. 1.9, to obtain, $\sum_n (z - \hat{H})_{mn} (z - \hat{H})_{np}^{-1} = \delta_{mp}$. For the special case p = 0,

 $\sum_{n}(z-\hat{H})_{mn}x_{n}=\delta_{m0}$, where $x_{n}=(z-\hat{H})_{n0}^{-1}$. This represents a system of linear equations for the unknown x_{n} . The particular case of n=0 corresponds to $\langle \phi_{0}|\frac{1}{z-\hat{H}}|\phi_{0}\rangle$ which is the quantity we wish to study. We can solve these linear equations using the Cramer's rule,

$$x_0 = \frac{\det B_0}{\det(z - \hat{H})},\tag{1.10}$$

where, the matrices can be written in the $\{|\phi_n\rangle\}$ basis as,

$$z - \hat{H} = \begin{pmatrix} z - a_0 & -b_1 & 0 & 0 & \cdots \\ -b_1 & z - a_1 & -b_2 & 0 & \cdots \\ 0 & -b_2 & z - a_2 & -b_3 & \cdots \\ 0 & 0 & -b_3 & z - a_3 & \cdots \\ \vdots & \vdots & \vdots & \vdots & \ddots \end{pmatrix}$$
(1.11)

and

$$B_{0} = \begin{pmatrix} 1 & -b_{1} & 0 & 0 & \cdots \\ 0 & z - a_{1} & -b_{2} & 0 & \cdots \\ 0 & -b_{2} & z - a_{2} & -b_{3} & \cdots \\ 0 & 0 & -b_{3} & z - a_{3} & \cdots \\ \vdots & \vdots & \vdots & \vdots & \ddots \end{pmatrix}. \tag{1.12}$$

The coefficients a_n and b_n were defined before when the Lanczos method was introduced. The determinants of these matrices can be expanded to give $\det(z - \hat{H}) = (z - a_0) \det D_1 - b_1^2 \det D_2$, and $\det B_0 = \det D_1$, where in general the matrix D_n is obtained from Eq. 1.11 by removing the first n rows and columns. Then, it can be shown that

$$x_0 = \frac{1}{z - a_0 - b_1^2 \frac{\det D_2}{\det D_1}}. (1.13)$$

The ratio of determinants in the above equation can be expanded in turn as

$$\frac{\det D_2}{\det D_1} = \frac{1}{z - a_1 - b_2^2 \frac{\det D_3}{\det D_2}} \tag{1.14}$$

This procedure can be repeated until a full continued fraction is constructed. Recalling the definition of the spectral intensity $I(\omega)$, finally it can be shown that

$$I(\omega) = -\frac{1}{\pi} \Im \left(\frac{\langle \psi_0 | \hat{O}^{\dagger} \hat{O} | \psi_0 \rangle}{\omega - a_0 - \frac{b_1^2}{\omega - a_1 - \frac{b_2^2}{\omega - a_2 - \dots}}} \right). \tag{1.15}$$

Recalling that $z = \omega + E_0 + i\epsilon$, we can obtain the spectral function for any value of the frequency ω and the width ϵ , with a knowledge of the ground state energy of the system. The only known way to test the convergence of the continued fraction expansion is to plot the spectral function with a particular ϵ , and observe that the results remain essentially unchanged with additional poles.

1.3 The Numerical Renormalization Group (NRG) method

Exact diagonalization and Lanczos methods firmly established the trend of computational approaches to deal with the complexity of strongly correlated electronic models. Nevertheless, the limitation of small cluster sizes leaves a substantial doubt in one's mind as to the validity of the results for real systems in the thermodynamic limit. In practice, the spin-1/2 Heisenberg model can be diagonalized on up to about 36 sites and the Hubbard model on up to about 20 sites. The exponentially increasing Hilbert space with increasing system size is an uphill battle and contains largely insignificant states as far as the low energy properties of interest are concerned. Therefore, a smarter algorithm would involve a systematic truncation scheme. Historically, the first successful algorithm to implement such a truncation was the numerical renormalization group (NRG) developed by Wilson [5] to solve the Kondo problem. The idea of the NRG for a quantum mechanical Hamiltonian H is to obtain the many-body eigenstates and eigenvalues on all energy scales in a sequence of steps, with each step corresponding to a distinct energy or length scale. Formally the procedure involves tracing out the high energy states to give effective Hamiltonians H_N , describing the physics at successively lower energy scales ω_N . The renormalization group (RG) transformation R relates effective Hamiltonians describing the physics on successive energy scales: $H_{N+1} = R[H_N]$. Although the idea is straightforward, it's efficacy as a tool to compute experimentally relevant quantities lies in the ability to integrate out the non-essential degrees of freedom and that turns out to be a difficult task.

The Kondo model describes a local magnetic moment (impurity) embedded in an uncorrelated metal and interacting antiferromagnetically with the conduction electron spin-density at the impurity (for a detailed discussion of physics of this model we refer

the reader to the monograph by Hewson [6]. The problem is highly non-perturbative in the coupling J and the system changes qualitatively over many energy scales as it passes through a crossover between a high temperature fixed point with well defined magnetic moment to a Fermi liquid fixed point at temperatures below the crossover scale. In order to describe this crossover the idea is to separate out the many energy scales in the problem and to set up a procedure for treating each scale in turn. Wilson's numerical RG for impurity models achieves this by a logarithmic discretization of the conduction band with intervals $[\Lambda^{-(n+1)}, \Lambda^{-n}]$ and $\Lambda > 1$ and a crucial mapping of the original spherically symmetric Kondo problem onto a one-dimensional quantum lattice model. The impurity is represented by the first site, and the spherically symmetric momentum shells, following a logarithmic discretization of the conduction band, are represented by a semi-infinite lattice with only near-neighbor hopping. Each successive site added along the chain corresponds to adding lower energy degrees of freedom, measured relative to the Fermi level.

After the mapping onto a 1D quantum lattice problem, the RG procedure proceeds as follows:

- 1. The first step is to break up the 1D chain into finite identical blocks (say, of size L) and create the block Hamiltonian H_B containing all terms of H involving only sites within B. Information regarding the block is stored by enumerating the quantum numbers of many-body states on the block and matrix elements of operators between these states. Let m be the number of states kept in each block.
- 2. In the second step, we isolate two such blocks and create the 'superblock' Hamiltonian H_{BB} (of size $m^2 \times m^2$) which comprises both intrablock and interblock terms. In order to do so, one needs to store $m \times m$ representations of the operators near the edges of the block.
- 3. Next, we diagonalize H_{BB} , and obtain the m lowest energy eigenvectors u^{α} .
- 4. We form matrix representations of the edge operators for the superblock BB from the corresponding matrices for B.

- 5. We change basis to the u^{α} , keeping only the lowest m states, using $H_{B'} = OH_{BB}O^{\dagger}$ (O is an $m \times m^2$ matrix with the rows made up of the eigenvectors u^{α}). The same transformation is used to obtain new operators at the edges of the superblock. Since $O(m \times m^2)$ is not a square matrix, the transformation truncates away high energy states.
- 6. Finally, we replace B with B' and go back to step 2 for the next iteration. The iterative procedure is continued until the system is large enough to represent the properties of the infinite system.

Although Wilson's approach to the Kondo problem is very similar to the algorithm described above, there is one important difference. Rather than doubling the system size with each iteration, a single site is added to the block at a time. The size of the superblock is nm (rather than m^2), n being the number of degrees of freedom per site. This allows for keeping a much larger number of states per block.

For a generic 1D lattice model, the neglect of the higher energy states at each iteration step does not guarantee that it will not lead to inaccuracy in the low energy part of the spectrum calcuated in subsequent iterations. However, in the Kondo and other quantum impurity models, the addition of an energy shell is a perturbation of relative strength $\Lambda^{-1/2} < 1$ and the coupling between successive "sites" decreases exponentially. It is to be noted here that the perturbation is independent of the size of the running couplings. Thus, due to the intrinsic separation of the energy scales and the logarithmic discretization of the conduction band, Wilson's RG works well for impurity models.

1.4 Failure of NRG for 1D Lattice models: Free particle on a chain

Following the success of NRG as applied to the Kondo problem, attempts were made to use the technique to study a number of quantum lattice models such as the Hubbard and Heisenberg models in one dimension. But it was observed that the method proved to be rather unreliable even for a computation of static properties such as the ground state energy. This result was not completely unanticipated because of a crucial difference between the Kondo problem and 1D quantum lattice models. The solution of the Kondo

problem relies on a trick whereby the Hamiltonian can be put into a special form, a chain with the impurity at one end and an exponentially decreasing hopping along the chain. On the other hand, in the case of 1D quantum lattice models, the coupling remains constant between adjacent sites all along the system. Another way to view the difficulty with NRG is in terms of boundary conditions. At any stage in the iteration procedure, the lowest lying states that are kept have inappropriate features at the ends of the block, because the block has no connections to the rest of the lattice. The best way to appreciate the inadequacy of the NRG idea for quantum lattice systems is to consider its application to the case of a free particle on a chain. The Hamiltonian clearly scales as the size of the chain L rather than an exponential of L as in an interacting system. It was observed that NRG does poorly in computing even the ground state energy as soon as the number of states per block m is less than L. It is easy to understand why. The eigenfunction of a particle on a chain of length L with fixed boundary conditions vanishes at both ends. If one imagines a system of size L to be constituted of two blocks at an earlier stage in the NRG iteration, each of size L/2, the ground states of the two blocks have nodes at their ends. Clearly a combination of the ground states of two blocks of size L/2 cannot reproduce a finite value at L/2for the ground state eigenfunction of the full system of size L as depicted in the figure below. Thus a treatment of the boundaries of the block is crucial in formulating an accurate RG procedure. White and Noack [7] formulated two types of RG procedures which solve these problems in the non-interacting case. The first procedure is called combination of boundary conditions (CBC) wherein the new truncated basis is made up of low lying eigenstates of several different block Hamiltonians with differing boundary conditions (for example, fixed and free, or periodic and anti-peridic). Although this procedure works very well by simulating a sufficiently general set of boundary conditions for the blocks, it is difficult to conceive a generalization to interacting Hamiltonians. For example, the many-body wavefunction for a system of non-interacting fermions is a Slater determinant of the single particle wavefunctions of the individual particles. Some of these particles may have nodes and some others may have antinodes at the boundaries of a block. Clearly, finding differing sets of boundary conditions which produce different

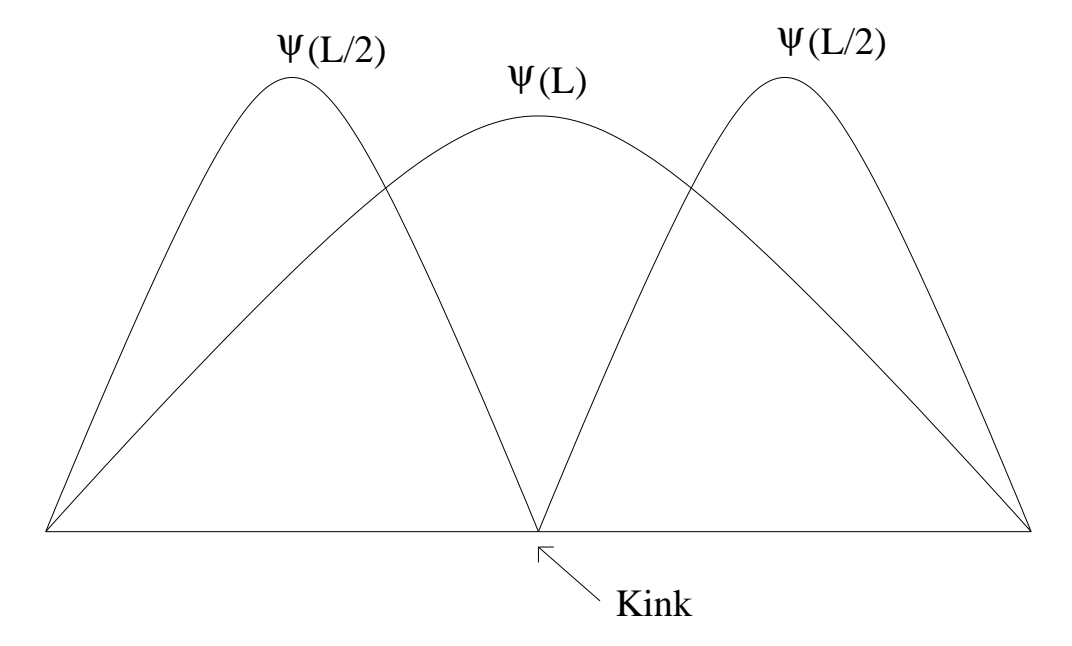


Figure 1.1: To remove the kink, one needs to keep almost all the states in each block behavior for different particles is very difficult.

An alternative procedure is to diagonalize a larger system than that contained in a block. The truncated basis for the block is then chosen by projecting the wavefunction of the superblock onto the system block. This projection is expected to provide the conditions at the boundaries that the transformed blocks would see as part of a larger system, which is the one of interest. This procedure is called the superblock method. Although the aforementioned projection is single-valued in the non-interacting system, it becomes multivalued for the interacting case. The Density Matrix Renormalization Group proposed by S.R. White [8,9], which we discuss in the next section, is based on choosing an optimal way of carrying out this projection.

1.5 The Density Matrix Renormalization Group (DMRG) method

The DMRG algorithm allows for a systematic truncation of the Hilbert space by keeping the most probable states of a subsystem required to accurately describe a set of states (usually, just the ground state) of the full system (for a review we refer the reader to the book [10]). This should be contrasted with the NRG method where just the lowest energy states of the subsystem are kept. The use of the density matrix to choose the

states to keep can be justified as follows.

Consider an isolated finite block at finite temperature. The probability that the block is in an eigenstate α of the block Hamiltonian H_B is proportional to the Boltzmann weight $\exp(-\beta E_{\alpha})$. The Boltzmann weight is an eigenvalue of the density matrix $\exp(-\beta H_B)$, and an eigenstate of the Hamiltonian is also an eigenstate of the density matrix. Since lowest energy corresponds to highest probability in the Boltzmann weight, the NRG approach amounts to choosing the most probable eigenstates to represent the block under the assumption that the block is isolated. However, the block is not isolated from the rest of the system, but is in fact strongly coupled to it. The block density matrix is no longer $\exp(-\beta H_B)$ and hence, the eigenstates of the Hamiltonian are not eigenstates of the block's density matrix. So it is more appropriate to describe the block using the density matrix rather than the eigenstates of the block Hamiltonian.

Incorporating the density matrix idea discussed above into a numerical renormalization group algorithm involves a fundamental departure from the NRG approach. Let us consider a quantum mechanical system in a definite pure state, and look at the properties of a part of the system. We label the entire system as the 'superblock'. The part that we are interested in constructing a truncated basis for will be called the 'system block' and the remainder of the system the 'environment block'. Let $|i\rangle$ label the states of the system block, and $|j\rangle$ label the states of the environment block, i.e., the rest of the superblock. If $|\psi\rangle$ is a state of the superblock,

$$|\psi\rangle = \sum_{i,j} \psi_{ij} |i\rangle \otimes |j\rangle,$$
 (1.16)

The reduced density matrix for the system block is defined as

$$\rho_{ii'} = \sum_{i} \psi_{ij}^* \psi_{i'j} \tag{1.17}$$

By normalization, $\text{Tr}\rho = 1$. The density matrix contains all the information needed from the wavefunction ψ to calculate any property restricted to the system block. If operator A acts only on the system block, then

$$\langle A \rangle = \sum_{ii'} A_{ii'} \rho_{ii'} = \text{Tr}\rho A$$
 (1.18)

In terms of the eigenvalues $w_{\alpha} \geq 0$ and the eigenvectors u^{α} of the density matrix,

$$\langle A \rangle = \sum_{\alpha} w_{\alpha} \langle u^{\alpha} | A | u^{\alpha} \rangle. \tag{1.19}$$

If for a particular α , $w_{\alpha} \approx 0$, we make no error in $\langle A \rangle$, for any A, if we discard u^{α} . This naturally suggests a renormalization group procedure.

In particular it can be shown precisely that keeping the most probable eigenstates of the density matrix gives us the most accurate representation of the state of the superblock, i.e., the system block plus the environment block. We wish to construct an accurate expansion for a state $|\psi\rangle$ of the form

$$|\psi\rangle \approx |\bar{\psi}\rangle = \sum_{\alpha,j} a_{\alpha,j} u^{\alpha} |j\rangle$$
 (1.20)

with $\alpha = 1, ..., m$ labeling the truncated states and m less than the actual number l of system block states. The error,

$$S = ||\psi\rangle - |\bar{\psi}\rangle|^2 \tag{1.21}$$

is to be minimized by varying over all $a_{\alpha,j}$ and u^{α} , subject to $\langle u^{\alpha}|u^{\alpha'}\rangle=\delta_{\alpha\alpha'}$. Defining $v^{\alpha}_{j}=\langle j|v^{\alpha}\rangle=N_{\alpha}a_{\alpha,j}$, with N_{α} chosen to set $\sum_{j}|v^{\alpha}_{j}|^{2}=1$, the error becomes,

$$S = \sum_{ij} (\psi_{ij} - \sum_{\alpha=1}^{m} a_{\alpha} u_i^{\alpha} v_j^{\alpha})^2$$

$$(1.22)$$

This error has to be minimized over all u^{α} , v^{α} , and a_{α} , given the specified value of m. The solution to this minimization problem can be obtained by using a singular value decomposition of $|\psi\rangle$,

$$\psi = UDV^T \tag{1.23}$$

where U and D are $l \times l$ matrices, V is an $l \times J$ matrix, with J denoting the number of states in the environment block. Here U is orthogonal, V is column-orthogonal, and the diagonal matrix D contains the singular values of ψ . With this decomposition the u^{α} , v^{α} , and a_{α} which minimize S are given as follows: the m largest magnitude diagonal elements of D are the a_{α} , and the corresponding columns of U and V are the u^{α} and v^{α} .

The reduced density matrix as defined earlier can be written as

$$\rho = UD^2U^T, \tag{1.24}$$

i.e., U diagonalizes ρ . The eigenvalues of ρ are $w_{\alpha} = a_{\alpha}^2$ and the optimal states u^{α} are the eigenstates of ρ with the largest eigenvalues. Each w_{α} represents the probability of the block being in the state u^{α} , with $\sum_{\alpha} w_{\alpha} = 1$. The deviation of $\sum_{\alpha=1}^{m} w_{\alpha}$ from unity, i.e., the 'discarded weight' of the density matrix eigenvalues, measures the accuracy of the truncation to m states.

To summarize, when the superblock is in a pure state, the optimal states to keep are the m most significant eigenstates of the reduced density matrix of the system block, obtained from the wavefunction of the superblock. The conclusion is found to be identical even when the superblock is in a mixed state, as is the natural assumption for a system at finite temperature.

The effectiveness of the truncation of the Hilbert space of the system block via the density matrix depends crucially on the distribution of the density matrix eigenvalues w_{α} . For certain exactly solvable systems, it is possible to show that the distribution of the density matrix eigenvalues decays exponentially. It is generally found that the convergence of the discarded weight (and thus the ground state energy) as a function of m for periodic boundary conditions is much slower than for open boundary conditions. Therefore, bulk properties of a system are best obtained by treating large lattices with open boundary conditions, rather than systems with periodic boundary conditions.

There are three main ingredients needed to define a DMRG algorithm: first, we have to decide how to add degrees of freedom to the system, second, we have to determine the configuration of the superblock and finally, we must choose which superblock eigenstate or eigenstates to use to construct the density matrix. The most efficient density matrix algorithms use one eigenstate, usually just the ground state or the lowest excited state to form the density matrix. The state used to form the block density matrix is usually called the 'target state'. The fewer the number of target states, the higher is the accuracy of their representation in terms of the block states. A density matrix algorithm is defined mainly by the form of the superblock and the manner in which the blocks are enlarged.

The typical superblock configuration used in most calculations is as shown below.

$$B_j^L \qquad \qquad B_{j'}^R \\ \blacksquare \cdots \bullet \cdots \bullet \cdots \blacksquare$$

 B_j^L represents a block composed of j sites and $B_{j'}^R$ is a block of j' sites. The symbol \bullet represents a single site. The total number of sites in the superblock is therefore L=j+j'+2. In the next iteration, the new block is formed from the left block plus one site, i.e., B_{j+1}^L . The right hand block and site $\bullet B_{j'}^R$ are only used to form the density matrix for B_{j+1}^L ; the states on $\bullet B_{j'}^R$ are traced over. The same configuration above is used in two different algorithms: the infinite and finite chain algorithms, which we discuss in detail further below.

1.5.1 Infinite Chain Algorithm

- 1. Start with a superblock configuration $B_j^L \bullet \bullet B_j^R$, having an equal number of sites in the left and right blocks. Represent the blocks by listing the quantum numbers of their states and set up matrices for the block Hamiltonian and other operators in that basis.
- 2. Build the Hamiltonian matrix in sparse matrix form for the superblock. If there are two states per site, then the superblock has $4m^2$.
- 3. Using the Lanczos method, diagonalize the superblock Hamiltonian to find the target state; typically just the ground state. At this stage one can measure the expectation values of any operators using the ground state wavefunction, $|\psi\rangle$.
- 4. Form the reduced density matrix for the left block plus the single site $B_j^L \bullet$ using the target state. To do this, the target state is decomposed as,

$$|\psi\rangle = \sum_{k \, l} \psi_{kl} \, |k\rangle \otimes |l\rangle \,,$$
 (1.25)

Here, k and l label the set of the basis states on the left block plus one site, $B_j^L \bullet$ and the right block plus one site $\bullet B_j^R$ respectively. We can regard $B_j^L \bullet$ as the 'system' and $\bullet B_j^R$ as the 'environment'. The reduced density matrix for the

system is obtained by tracing over the degrees of freedom within the environment.

$$\rho = \sum_{l} \psi_{kl} \psi_{k'l}^* \tag{1.26}$$

- 5. Diagonalize ρ to find a set of eigenvectors u^{α} and eigenvalues w_{α} . Discard all but the m largest eigenvalues and associated eigenvectors.
- 6. Form matrix representations of operators such as H for the $B_j^L \bullet \bullet B_j^R$ configuration from operators for each separate block.
- 7. Form a new left block by changing basis to the u^{α} and truncating to the m states using $H'_{B^L_{j+1}} = OH_{B^L_{j+1}}O^{\dagger}$. O is an $m \times m^2$ matrix with the rows made up of the eigenvectors u^{α} . The new right block is formed by reflecting the left block. Also we obtain new operators at the edges of the superblock using the same transformation.
- 8. Start a new iteration with the configuration $B_{j+1}^L \bullet \bullet B_{j+1}^R$. One continues in this manner, adding two sites at each step of the iteration, until each block represents one half of an infinite chain.

The infinite chain algorithm converges from two separate causes: increase in the left block size approaching an infinite chain and also in the sense that the left block states are better adapted to an infinite sized environment to the right. This algorithm is typically used for a quick and pretty accurate study of the ground state properties of a system.

1.5.2 Finite Chain Algorithm

This algorithm is used to study the properties of a finite sized system of size, say L, (we assume L to be even . It consists of the following steps:

1. During what is referred to as the first sweep, we start with a superblock configuration $B_1^L \bullet \bullet B_1^R$, with B_1^L and B_1^R representing a single site. Then, we use the infinite size algorithm to grow the superblock until it reaches the size $LB_{L/2-1}^L \bullet \bullet B_{L/2-1}^R$, the next step is to use $B_{L/2}^L \bullet \bullet B_{L/2-2}^R$ to form $B_{L/2+1}^L$. This and all other superblocks to follow have L sites. We continue to increase the size of the left block

until it reaches L-3, using the superblock $B_{L-3}^L \bullet \bullet B_1^R$. Unlike the infinite size algorithm, where the the block B_l^L is not required after the formation of B_{l+1}^L , all the L-3 blocks and the operators on them are stored. The blocks are labelled by their size. During the sequence of iterations above, it is common to refer to the left block plus one site to its right as the "system" and the right block plus one site to its left as the "environment". At each step the degrees of freedom within the environment are traced over to obtain the reduced density matrix for the system.

- 2. In the next half of what is referred to as the first sweep, the meanings of the environment and system are reversed. The starting superblock B^L_{L-3} •B^R₁ (B^R₁ being a single site is represented exactly) is used to obtain B^L_{L-4} ••B^R₂. In this step, B^L_{L-4} from the previous iteration is read from the stored version and its degrees of freedom are traced out to obtain B^R₂. This sequence of steps is continued, until at the end of the first sweep we reach the configuration, B^L₁ ••B^R_{L-3}. At each stage the new blocks formed are written to disk for use during the next sweep.
- 3. The second sweep begins with $B_2^L \bullet \bullet B_{L-4}^R$, the right blocks now being read from the disk at each iteration to form a reduced density matrix for the left block until we reach $B_{L-3}^L \bullet \bullet B_1^R$. The second half of this sweep comprises the iterations taking the system from $B_{L-3}^L \bullet \bullet B_1^R$ back to $B_2^L \bullet \bullet B_{L-4}^R$, with now the left blocks being read from disk.
- 4. The sweeps are continued until a convergence criterion is satisfied. The criterion typically used is a comparison of the ground state energy in successive sweeps.

 Usually a convergence is achieved in two or three sweeps.
- 5. On the very last sweep we usually stop after the diagonalization of $B_{L/2-1}^L \bullet B_{L/2-1}^R$, and then use the ground state wave function (or the target state) of the L-site system to measure various properties such as static averages.

The steps in one full sweep of the finite size algorithm are schematically represented in Fig 1.2. For a given system of size L, the finite size algorithm is more accurate than

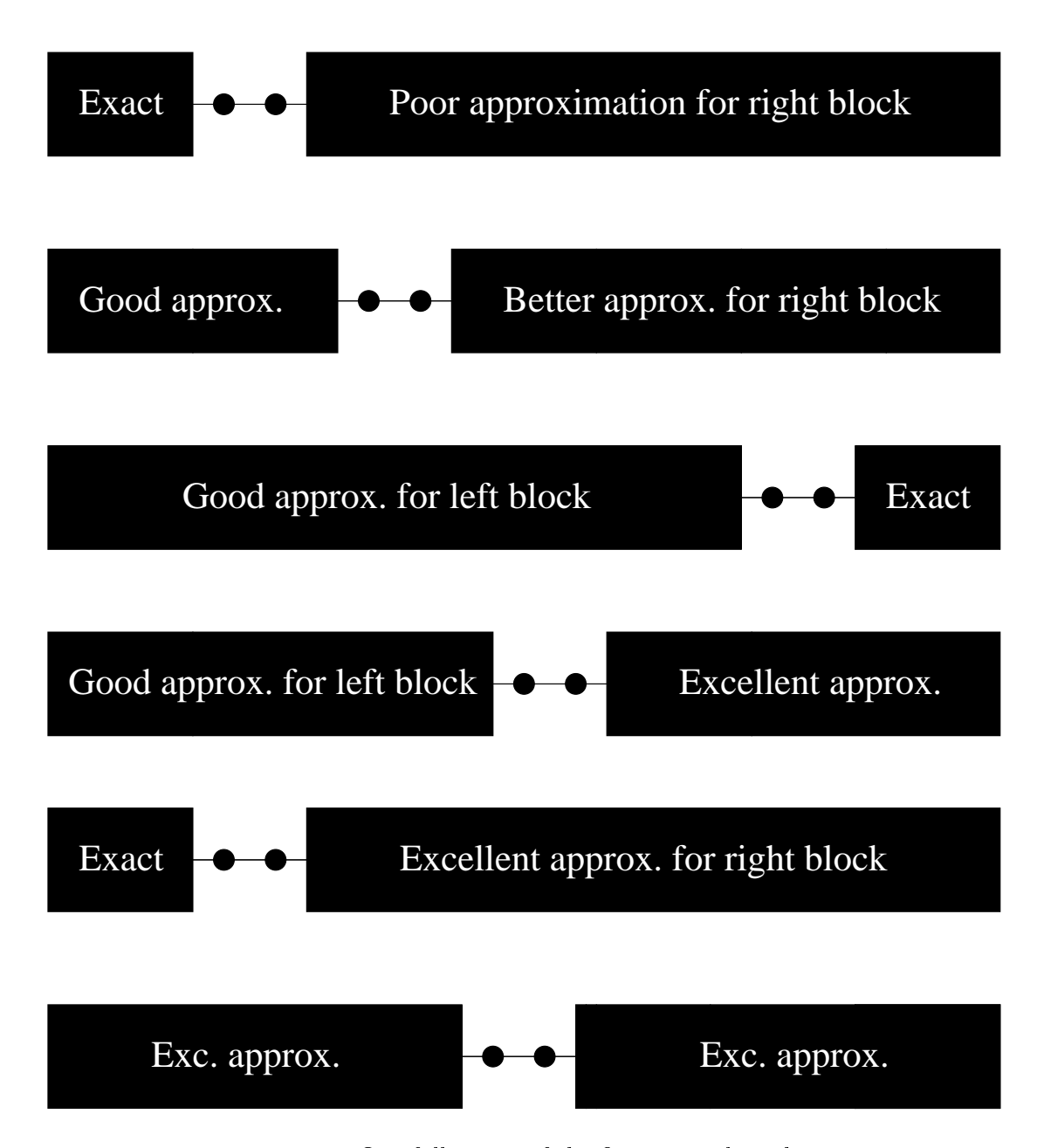


Figure 1.2: One full sweep of the finite size algorithm

the infinite chain algorithm, because both the left and right blocks of the superblock, alternatively assume the role of the system and environment and are thereby equally well adapted to represent the other. On the other hand, in the infinite size algorithm only the system is adapted to respond to the environment. The higher accuracy of the finite size algorithm comes at the price of a more complicated algorithm and also a higher computational cost in terms of both CPU time and memory.

A detailed examination of the truncation error (or the error in the ground state energy) as a function of m and number of finite size sweeps is useful. It is found that there is virtually no dependence of the accuracy of the energy on m in the zeroth iteration, the infinite system phase. After two or three sweeps, the error in the energy saturates for a given m, with the saturation occurring after a larger number of sweeps for larger m. Therefore, it makes sense not to have a uniform value of m for all the sweeps, but to increase m rapidly with each iteration such that most of time is spent in the last and most important sweep. Another noteworthy feature is that convergence is completely independent of coupling parameters in the Hamiltonian such as U in the Hubbard model. For a fixed number m of states retained, the discarded weight is higher as you increase the range of the interaction in the Hamiltonian. One can get an idea of the performance of the DMRG algorithm by considering a typical example, such as the case of the spin-1 Heisenberg chain. The ground state energy for the infinite system is obtained accurately up to seven decimal places, with as little as m=100 states kept and a discarded weight of 10^{-11} .

1.6 Dynamical Correlation Functions using DMRG

Some of the most significant insights into the properties of materials are obtained by an investigation of dynamical observables. These are probed by several experiments which include neutron scattering, optical absorption and photoemission, amongst others. Although it has been possible to solve for the exact spectra of several one-dimensional quantum systems using Bethe ansatz, calculation of dynamical properties within this framework are difficult and rare. Given that the DMRG method performs remarkably

well in calculating ground state energies and static properties of low dimensional systems, it is natural to ask whether it can provide a reliable framework for the study of dynamical properties. Since the original idea of the DMRG method involves a strong truncation of the Hilbert space at each step using a reduced density matrix, typically built out of just the ground state, much information of the excited states vital to a computation of dynamical properties is lost. It is clear that we need to 'target' more states than just the ground state to build correlation functions. There are two fundamental questions to be addressed in this context.

- 1. To what extent does the density of states for the superblock, which is constructed by targeting only a few states, approach the true one for the full Hilbert space in a wide energy range?
- 2. In order to describe dynamical properties reliably, what is the criterion to select more target states?

The first question can only be addressed by making a comparative study with known results for low dimensional systems. The second question leads naturally to different methods within DMRG for studying correlation functions. In the ensuing discussion we focus entirely on zero temperature dynamics. At finite temperature, it is possible to evaluate local imaginary-time correlations quite accurately within the transfer matrix renormalization group (TMRG) approach and we refer to [11] for details. In principle one can extract real frequency information from imaginary-time correlation functions using the maximum entropy method, but the quality is not as good as the source data because of the intrinsically ill-conditioned inverse problem. The TMRG method as such involves a diagonalization of the transfer matrix rather than the Hamiltonian. The free energy and other thermodynamic quantities are determined by the maximum eigenvalue of the transfer matrix.

1.6.1 Lanczos vector method

We saw earlier that the zero temperature Green's function for an operator A could be written in the form of a continued fraction expansion using the Lanczos vector method.

$$G_A(z) = \langle \Psi_0 | A^{\dagger}(z - H)^{-1} A | \Psi_0 \rangle \tag{1.27}$$

$$= \frac{\langle \psi_0 | A^{\dagger} A | \psi_0 \rangle}{z - a_0 - \frac{b_1^2}{z - a_0 - \frac{b_2^2}{z - a_0 - \dots}}}$$
(1.28)

In this equation the coefficients a_n and b_n are defined through the recursion relation Eq. 1.3 and Eq. 1.4. In practice, the continued fraction often converges to a limit already for finite $n \approx 100 - 120$ since b_n goes to zero and a_n becomes very large.

The first reliable DMRG scheme to compute zero temperature correlation functions, proposed by K. Hallberg [12], is based on this continued fraction representation. The key idea of the method is to use the Lanczos basis states $\{|\phi_n\rangle\}$ as additional target states along with the ground state while building the density matrix at every DMRG iteration. It is expected that the states in the reduced Hilbert space relevant to the excited states connected to the ground state via the operator A, are included in this set. The full density matrix used to truncate the Hilbert space is then a weighted average of the density matrices for each target vector.

$$\rho_{ii'} = \sum_{l=1}^{M} p_l \sum_{i} \phi_{ij}^l \phi_{i'j}^l$$
 (1.29)

where M is the total number of target states, i and j denote the states of the system and the environment, respectively, and p_l ($\sum_l p_l = 1$ to keep a unitary trace in ρ) is the weight of the target state ϕ^l . Here ϕ^1 is the ground state and $\phi^l(l=2,..M)$ represent the Lanczos basis states. There is no known optimal way of assigning a relative weight between the ground state density matrix and the density matrices built from the Lanczos basis states. Typically, 50% of the weight is assigned to the ground state, and the remaining is distributed amongst the Lanczos target states. The weight of a Lanczos vector ϕ^l in the spectrum is given by

$$p_l = \sum_{m} (\langle \phi^2 | \psi_m \rangle)^2 (\langle \phi^n | \psi_m \rangle)^2$$
 (1.30)

Here $|\psi_m\rangle$ represents the eigenvector of the Hamiltonian with eigenvalue E_m . The actual calculation of the correlation function is made when the system block is the same size as the environment block, since the truncation errors are smallest in that step. To do this, one not only uses the Lanczos vectors that were target states, but keeps calculating new Lanczos vectors until orthogonality breaks down due to the finite numerical precision. With the number m of states retained per block fixed, the more the number of target states considered, the less is the precision of each one of them. The prime source of error stems from the approximation of the identity in terms of the small number of Lanczos basis vectors that can be used as target states in practical calculations. Every additional Lanczos vector adds another peak, typically at high energy, and so higher energy excitations will become inaccurate. Therefore, an optimal number of target states M and of retained states per block m has to be found in each case. Proper sum rules have to be calculated to determine the errors involved.

The convergence of the Lanczos procedure depends crucially upon the level spacing of a given system, getting worse with reducing level spacing. Since the DMRG technique treats much larger systems than exact diagonalization, the level spacing is much smaller, naturally making the algorithm less accurate for extremely large systems.

1.6.2 Correction vector method

Since the Lanczos vector method represents the correlation function with discrete poles, it works very well when the spectrum consists of a few sharp features at low energy. Therefore it is ill-suited to reproduce higher energy properties, such as the shape of a broad excitation band. Since increasing the number of target states merely reduces the quality of targeting for each state, a different method is required. This method [13] proposes the targeting of the ground state plus another state called the correction vector, to reproduce the spectrum at a fixed frequency, $z = \omega + i\eta$. The target states include:

$$|\psi_0\rangle$$
 the ground state
$$|A\rangle = A|\psi_0\rangle$$
 the first Lanczos vector
$$|x(z)\rangle = \frac{1}{z-H}|A\rangle$$
 the correction vector (1.31)

Since a finite broadening η is used, the correction vector can be split into it's real and imaginary part. The imaginary part is obtained by solving the following linear set of equations, typically using the conjugate gradient method:

$$((H - \omega)^2 + \eta^2)|\operatorname{Im}(x(z))\rangle = -\eta|A\rangle \tag{1.32}$$

This equation becomes singular as ω gets closer to an eigenenergy of the Hamiltonian, and as the broadening factor η becomes smaller. Naturally, the conjugate gradient algorithm converges much faster for larger η 's, but that clearly limits the resolution of the spectrum. Therefore, a suitable compromise between resolution of the spectrum and computation time for the conjugate gradient algorithm has to be reached empirically. The real part of the correction vector is calculated using

$$|\operatorname{Re}(\mathbf{x}(\mathbf{z}))\rangle = \frac{1}{\eta}(\mathbf{H} - \omega)|\operatorname{Im}(\mathbf{x}(\mathbf{z}))\rangle$$
 (1.33)

In terms of the correction vector the Green's function can be written directly as:

$$G_A(z) = \langle A|x(z)\rangle \tag{1.34}$$

The use of the above three vectors as target states, optimizes the DMRG basis to represent them and allows for a direct computation of the Green's function at a given frequency ω with a broadening factor η . In practice, the correlation function is still computed as in the Lanczos vector method, except that the spectrum is accurate only near ω . Extremely precise results for the spectra can be obtained by using two correction vectors close in frequency and using them to compute the Green's function for frequencies between them. Clearly, the correction vector method is more costly in terms of computation time as compared to the Lanczos vector method which provides the Green's function over the entire frequency range in one DMRG run. Nevertheless, it is better suited for the study of broad excitation bands. In practice, depending on the problem at hand, one would first use the Lanczos vector method and then ascertain the necessity of using the correction vector method to obtain the Green's function in a particular frequency range more accurately.

1.7 Extension to two dimensions

The issue of how to optimally extend the DMRG to two or more dimensional quantum systems is difficult and is a subject of active development. It is instructive to first consider the extension of the one-dimensional algorithm to one of finite width, i.e., a ladder. A simple extension of DMRG to solve for this system would be to replace the single sites added between the blocks with rows of sites. However, the extra degrees of freedom added to the system would make the Hilbert space prohibitively large. The most straightforward way to have a two dimensional algorithm which adds only a single site to a system block at a time is to map the 2D system onto a 1D system, viz., to choose a path to order all the lattice sites. Therefore, the 2D procedure differs from the 1D one in that there are additional connections between the system and environment blocks. A typical path running up and down the width of the system is illustrated in the figure below. The number of states needed to maintain a certain truncation

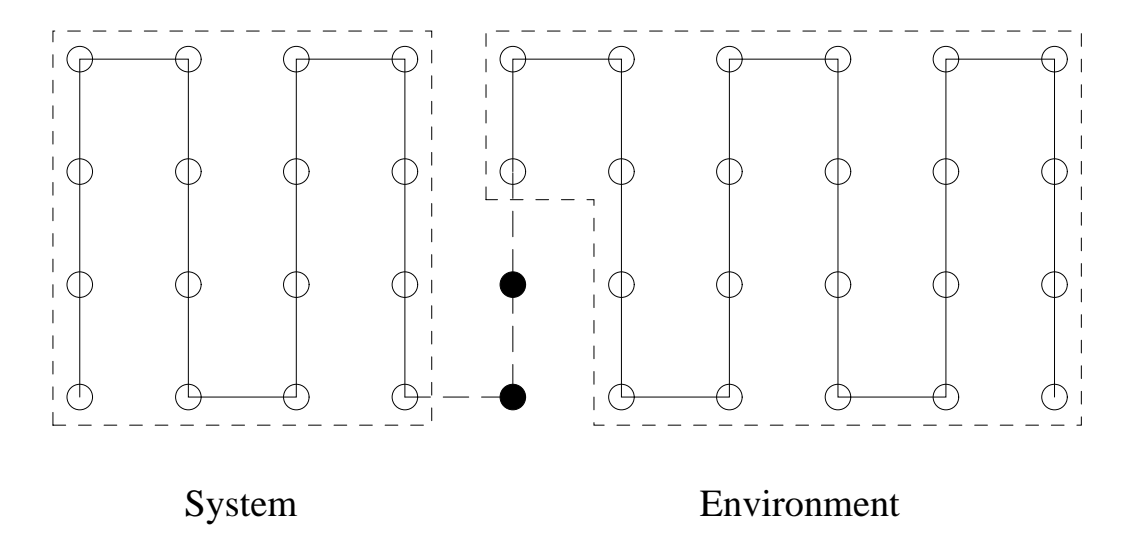


Figure 1.3: A 2D DMRG algorithm obtained by mapping onto a 1D lattice

error in the density matrix projection procedure depends strongly on the number of operators connecting the two system and environment. Best accuracy is obtained when the number of connections between the two is minimized. Therefore it is common to study open systems or periodic only along the width of the ladder. It was found by Liang and Pang [14] that the number of states needed to maintain a certain accuracy

grows exponentially with the width of the lattice. Although the system studied by them was a gas of non-interacting spinless fermions, it is expected that the above statement is probably valid for any 2D DMRG calculation performed by using the 1D mapping. Thus this algorithm, is not a true 2D DMRG algorithm.

The momentum space DMRG provides an alternative way to implement the DMRG in two or more dimensions. In this representation, the momentum is conserved and kinetic energy is treated rigorously since it is diagonal. However, interactions such as the Hubbard term are non-diagonal in momentum space. The Hubbard interaction in momentum space involves a sum over three momenta leading to N^3 terms in the Hamiltonian. Therefore, a straightforward implementation is not possible for realistic calculations. It was observed in [15] that the three-fold summations in the interaction can be reduced to a sum containing an order N number of terms by defining certain composite operators. To carry out the DMRG iterations, one needs to order the $(k\sigma)$ points. In general, all $(k\sigma)$ points are connected to each other by interactions, and the rate of convergence of the ground state energy depends strongly on the ordering. A rule of thumb for ordering the $(k\sigma)$ points is that those $(k\sigma)$ pairs which have the strongest interaction should be arranged as close as possible in the ordered $(k\sigma)$ chain. In the Hubbard model, however, the interaction strength does not depend on k and one may choose any ordering. This is not the case, for example, with the extended Hubbard model with nearest neighbor Coulomb repulsion. Results obtained in both one and two dimensions for the Hubbard model using the momentum space DMRG, although reasonable, show that the method is good only at weak coupling. For the one dimensional half filled Hubbard model a comparison to real space DMRG shows that momentum space DMRG performs poorer. This is because the Hubbard interaction is local in real space and electrons tend to be localized in space at half filling. In two dimensions the method performs better than in one dimension, but only because the relative contribution of the kinetic energy term to the ground state energy, which is treated rigorously, compared with the potential energy, is larger in two dimensions than in one. Therefore, although it is a step towards a true 2D DMRG algorithm, the momentum space DMRG is not quite one, because its performance depends on the strength of the interactions.

We shall discuss in Chapter 5 an approach to combine the DMRG idea with dynamical mean field theory in order to obtain a 'better candidate' for a 2D RG algorithm.

Chapter 2

Optical response and excitons in one dimensional Mott insulators

2.1 Introduction

In recent years, several materials have been discovered that allow the investigation of the properties of the 1D electronic state under the influence of both strong electron-lattice and electron-electron correlation. These quasi one dimensional systems include materials such as SrCuO₂, Sr₂CuO₃, conjugated polymers and Ni halides [16–18] amongst several others. These systems, well described as Mott insulators, remain a challenge to existing theoretical methods. In this chapter we shall discuss some insights that have been obtained into the optical response, charge gap and the behavior of excitons in one dimensional Mott insulators utilizing the density matrix renormalization group (DMRG) method.

2.2 Wannier and Mott Excitons

Excitons in conventional band insulators are well described by Wannier theory. A Wannier exciton is a charge neutral optical excitation made of an electron in the conduction band and a hole in the valence band, bound together by the Coulomb attraction between them. In inorganic semiconductors like GaAs, the typical binding energy, as defined by the energy difference between the exciton and the band edge of the particle hole continuum, is several meV. This should be compared with the band gap itself, which is of the order of one eV. The typical size of a Wannier exciton at 100Å is almost two orders of magnitude larger than the lattice spacing. We also note that although the

total spin of an optically excited exciton is necessarily zero, it is composed of two quasiparticles carrying spin-1/2. In Wannier theory, exciton properties, such as size, binding energy, effective mass, or optical weight, are related by simple equations and exhibit a monotonic behavior as a function of the Coulomb repulsion strength. This simplicity is due to a drastic assumption of this theory: optical excitations are represented by electron-hole pairs which are independent from the system's other degrees of freedom. The interaction with these degrees of freedom is taken into account only through renormalized parameters such as effective masses for the electron and hole, and an effective background dielectric constant for the Coulomb interaction between electron and hole.

In the case of Mott insulators, the situation is quite different and the exciton properties show a more complex behavior. Although a Mott-Hubbard exciton can be described as a bound pair of excitations with opposite charges, the Coulomb interaction at the same time determines the size of the Mott gap, the exciton properties, and the coupling of the exciton to the other electrons in the system. Therefore, an increase of the Coulomb interaction strength does not simply bind the exciton more tightly, but also renormalizes the gap and couples the particle-hole excitation more strongly to the other electrons. This leads to a non-monotonic behavior of Mott-Hubbard exciton properties as a function of the Coulomb repulsion strength, and even to instabilities toward the formation of charge-density wave droplets. The exciton binding energy, in e.g., polydiacetylenes [19, 20]is found to be of the order of 0.5 eV and is comparable to the optical gap which is of the order of 2.4 eV. The exciton size has been estimated to be as small as 12Å and hence comparable to the length of the unit cell at 5Å. These facts naturally suggest that electron-electron interactions will play an important role in any theoretical description of excitons in these materials.

2.3 Model Hamiltonian

Realistic models for the aforementioned systems must account for the effects of both electron-electron and electron-phonon interactions. Given the complexity of the task, as a first step it is natural to investigate the effects of the two mechanisms separately. We focus entirely on the effects of electron-electron interaction and study the Extended

Hubbard Model (EHM) defined by

$$H = -t\sum_{j,\sigma} \left(c_{j+1\sigma}^{\dagger} c_{j\sigma} + \text{h.c.} \right) + U\sum_{j} \left(n_{j\uparrow} - \frac{1}{2} \right) \left(n_{j\downarrow} - \frac{1}{2} \right) + V\sum_{j} \left(n_{j} - 1 \right) \left(n_{j+1} - 1 \right)$$

$$(2.1)$$

The first two terms corresponding to hopping between nearest neighbor sites and the onsite Coulomb repulsion provide the competition between itineracy and localization in the regular Hubbard model. The third term represents Coulomb repulsion between electrons occupying nearest neighbor sites. The Hamiltonian as written above guarantees an insulating ground state with a filling of one electron per site.

Although this model has been widely studied, many questions remain unanswered. The Bethe Ansatz method provides an exact solution, but only when V=0 [21]. The method has been used to obtain the energy spectrum and thermodynamics, but a reliable computation of dynamical quantities such as the optical response remains elusive. Non-perturbative analytic studies of the dynamical response in these systems have largely been restricted to the continuum limit [22,23]. We discuss the relevance of these studies later in this chapter.

Numerical methods such as exact diagonalization, although valuable in providing real frequency information, are limited to small system sizes [24]. Quantum Monte Carlo methods can treat large finite size clusters, but analytic continuation from imaginary to real frequencies is an unreliable procedure.

The renormalization group idea has helped with some of the toughest problems in physics in which, typically, a large number of degrees of freedom play an essential role. The efficacy of this idea as a tool to compute experimentally relevant quantities lies in the ability to integrate out the non-essential degrees of freedom. This has been brought to fruition with tremendous success in a numerical algorithm for low dimensional interacting systems, namely the Density Matrix Renormalization Group (DMRG) [8,9], which was discussed in detail in the previous chapter. The standard DMRG method coupled with the "Lanczos vector method" is expected to be very efficient in capturing sharp features at low energies such as excitons in the optical spectrum. Although excitonic features in multi-particle correlation functions have been reported in the EHM in

previous studies, there has been no reliable non-pertubative computation of the optical conductivity over the entire range of frequency and coupling parameters [25–27].

2.4 Phase diagram

The EHM at half-filling shows an interesting phase diagram. In the weak coupling limit $(U \ll t)$ the system undergoes a second order transition from a spin density wave (SDW) phase to a charge density wave (CDW) state as a function of increasing V, at $V = U/2 + \delta(U)$. For intermediate values of U the SDW and CDW phases are separated by a narrow region with a bond charge density wave (BCDW) order. As one approaches strong coupling $(U \gg t)$, the transition is again from an SDW to a CDW phase at $V = U/2 + \delta(U)$, but it is now first order. The small correction $\delta(U)$ is positive and approaches zero at both the weak and strong coupling ends. The precise location of a tricritical point at the crossover between the first and second order transitions has been a subject of much investigation [22, 28–31] and is complicated by the existence of the BCDW order.

2.5 Optical response and spectral functions

In this section we look at the optical response and local spectral function of the EHM in the strong coupling regime. We fix U at a realistic value of 12t (eg. $SrCuO_2$). The first order transition between the SDW and CDW phases is manifest in the optical properties as well as in the ground state energy. All the results presented here were obtained from computations performed with finite size chains of $N_s = 50$ sites with open boundary conditions using the Lanczos vector method. Studying other sizes ($N_s = 18, 34, 66$) shows that the results for $N_s = 50$ are fairly representative of the thermodynamic limit. We use the finite size version of the DMRG algorithm and choose m = 300 for the largest system sizes we consider. Selected runs performed with higher values of m did not introduce significant changes in the results. Typical discarded weights were $O(10^{-6})$. To validate our code, we compared our results for the static and dynamic properties with exact diagonalization for short chains.

We use the following definition for the response function:

$$\chi_{AB}(\omega) = \frac{i}{L} \int_0^\infty dt \ e^{i(\omega + i\epsilon)t} \langle 0 \left| \left[A^{\dagger}(t), B(0) \right] \right| 0 \rangle$$
 (2.2)

The real part of the optical conductivity is defined through the imaginary part of the current–current response with $\epsilon \to 0$,

$$\sigma'(\omega) = \frac{1}{\omega} \chi''_{jj}(\omega) \tag{2.3}$$

where

$$j = -it \sum_{j,\sigma} \left(c_{j+1\sigma}^{\dagger} c_{j\sigma} - c_{j\sigma}^{\dagger} c_{j+1\sigma} \right) \tag{2.4}$$

is the paramagnetic current operator. The non-resonant Raman spectrum in a Mott-Hubbard system is given by the response function of the stress energy tensor [32],

$$\tau = -t \sum_{j,\sigma} \left(c_{j+1\sigma}^{\dagger} c_{j\sigma} + c_{j\sigma}^{\dagger} c_{j+1\sigma} \right) \tag{2.5}$$

In the case of an insulator, $\chi_{\tau\tau}$ is not the dominant contribution to the total Raman spectrum. But it is interesting for a comparison with χ_{jj} because, j and τ are odd and even respectively under parity conjugation, apart from an overall phase.

Apart from the particle-hole symmetry, the Hamiltonian has two other discrete symmetries relevant to the computation of optical excitations: a spin-flip symmetry and a spatial reflection symmetry through the lattice center. Therefore each eigenstate of the Hamiltonian has a well-defined parity under charge conjugation $(P_c = \pm 1)$ and spin-flip $(P_s = \pm 1)$, and belongs to one of the irreducible representations, A_g or B_u , of a one-dimensional lattice reflection symmetry group. We note here that the current operator is invariant under the spin-flip transformation, but antisymmetric under charge conjugation and spatial reflection. Therefore, if the ground state belongs to the symmetry subspace (A_g, P_c, P_s) , only excited states belonging to the symmetry subspace $(B_u, -P_c, P_s)$ contribute to the optical conductivity.

A very useful consistency check of the method we use to compute dynamical correlation functions is to test various sum rules, relating the moments of the function $\sigma(\omega)$ or the spectral function $A(\omega)$ to ground state expectation values, which can be evaluated with great accuracy using the standard DMRG method. For instance, for a Hamiltonian with open boundary conditions we can write the following sum rules:

$$\int_0^\infty d\omega \ \omega \sigma(\omega) = \frac{1}{L} \langle 0|\hat{j}^2|0\rangle \tag{2.6}$$

$$\int_0^\infty d\omega \sigma(\omega) = \frac{e^2 t}{2L} \langle 0| \sum_{j\sigma} \left(c_{j+1\sigma}^{\dagger} c_{j\sigma} + c_{j\sigma}^{\dagger} c_{j+1\sigma} \right) |0\rangle$$
 (2.7)

$$\int_{-\infty}^{\infty} d\omega A(\omega) = 1 \tag{2.8}$$

In Fig. 2.1 we show the local spectral function for various values of V ranging from 0 to 9t. In the SDW phase, the single particle gap (Δ_s) stays constant until a threshold value of V around 3t is reached and then starts reducing (cf. Fig. 2.4). Here and further in this letter when we refer to the gap in a correlation function we measure the position of the lowest energy peak. We ignore the tail part which originates from the small finite broadening that is used to represent the Lanczos continued fraction. This implies that our values for the gaps are tight upper bounds to the actual ones. At the SDW-CDW transition, the spectral gap reduces abruptly, reaches a finite value, jumps up and then starts increasing again in the CDW phase. Note that in the CDW phase, the site on which we compute the spectral function is empty in the ground state. In Fig. 2.2 we report the current-current and non-resonant Raman response functions in the left and right columns respectively. A systematic change in the optical response in the odd (χ_{jj}) and even $(\chi_{\tau\tau})$ channels is discernible as we sweep through V across the SDW and into the CDW phase. For V=0 we see a broad feature centered at around U, in good agreement with a recent calculation for the standard Hubbard model within the DMRG approach [33]. Our method does not allow a resolution of the tiny bump seen in the middle of the broad optical absorption band by Jeckelmann et al [33]. But, as V is increased we do notice the formation of a resonance which gradually gains in weight and shifts towards lower frequencies [26,27,34]. This constitutes a precursor of the excitonic feature that we describe further below.

For small values of V the optical (Δ_{jj}) and Raman $(\Delta_{\tau\tau})$ gaps would be expected to coincide with the spectral gap, Δ_s . We find them to be slightly larger because it is not possible to create fully non-interacting electron-hole pairs in a finite size chain.

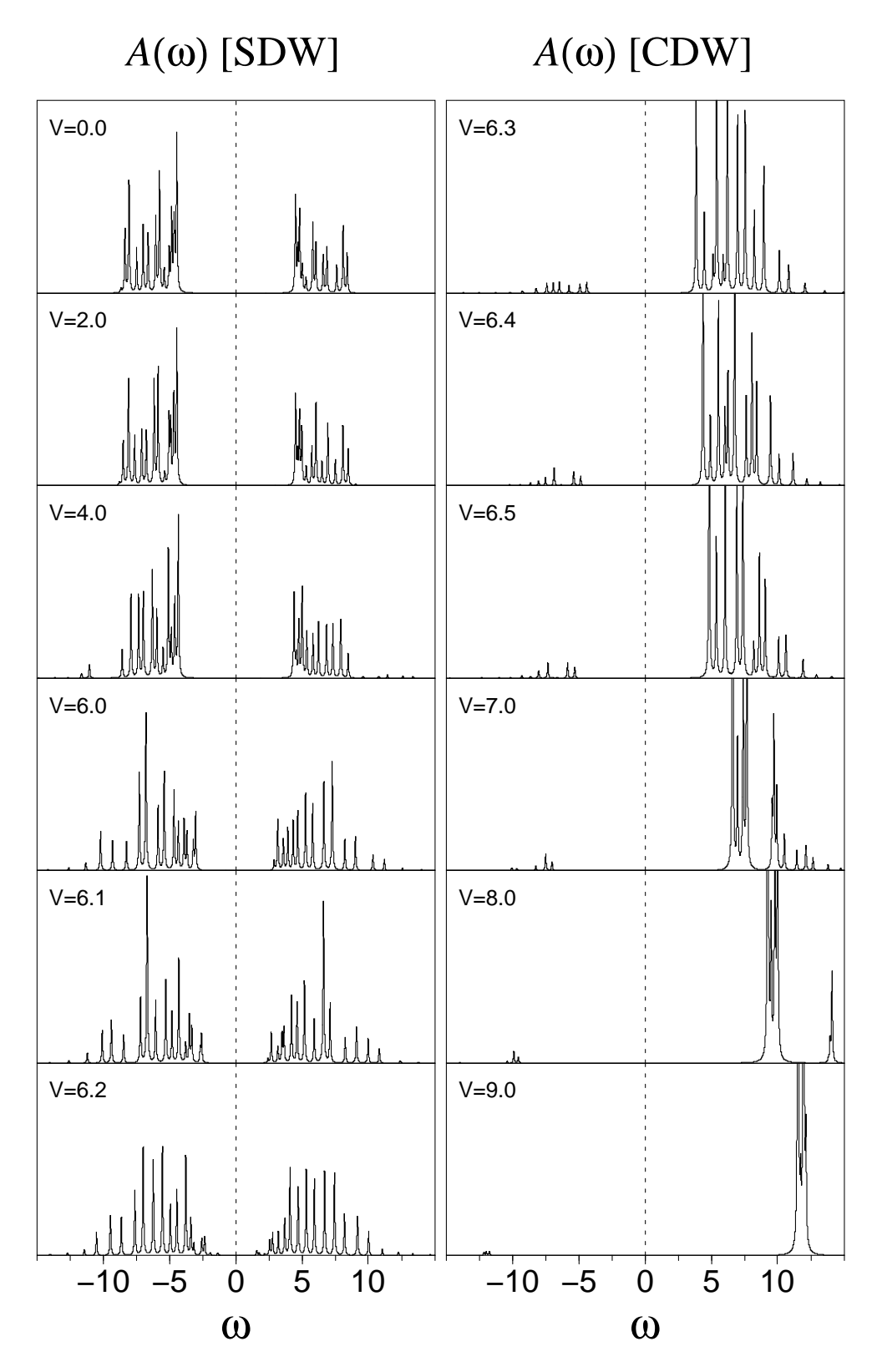


Figure 2.1: Local spectral functions for different values of the coupling V. Note the abrupt change in particle—hole symmetry between the two phases.

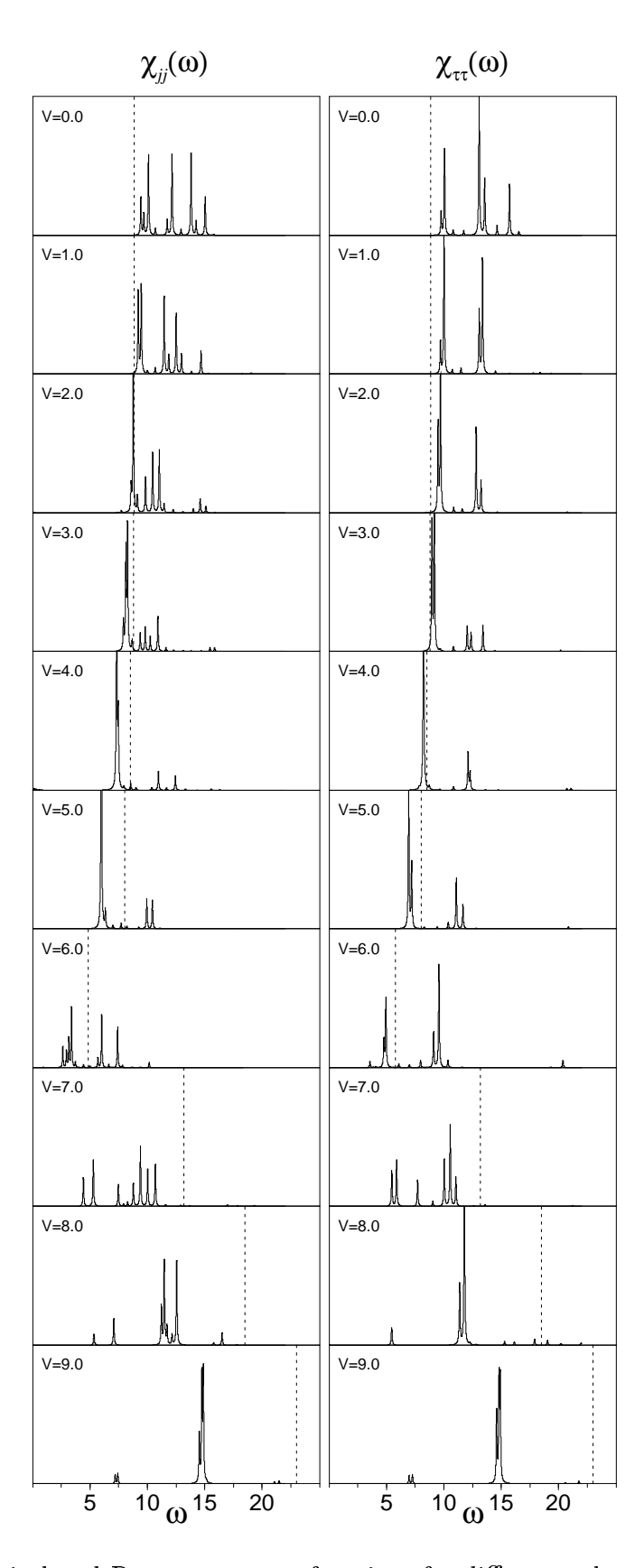


Figure 2.2: Optical and Raman response functions for different values of the coupling V. The vertical dotted line indicates the magnitude of the single–particle spectral gap in each case.

Around $V \sim 1.5t$, the optical gap falls below the spectral gap in agreement with previous work [25]. The same happens for the Raman gap at $V \sim 3t$. We define a quantity that we will call the excitonic weight $(W_{jj(\tau\tau)})$ as the fraction of the weight in the optical (Raman) spectrum below Δ_s ;

$$W_{jj(\tau\tau)} = \frac{\int_0^{\Delta_s} d\omega \ \chi_{jj(\tau\tau)}(\omega)}{\int_0^{\infty} d\omega \ \chi_{jj(\tau\tau)}(\omega)}$$
 (2.9)

In Fig. 2.3 we plot this excitonic weight as a function of V. In the case of both response

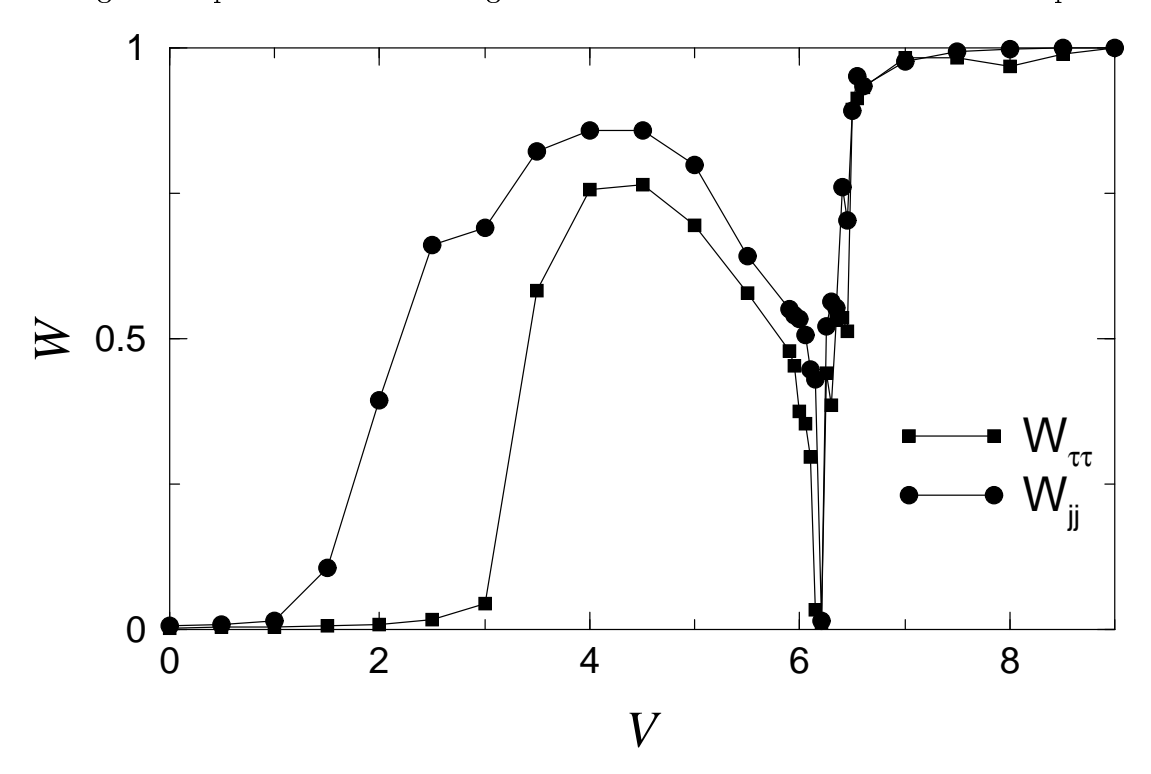


Figure 2.3: Excitonic weight as a function of the coupling V.

functions it is seen that the excitonic weight is zero until the above mentioned crossing of gaps occurs (cf. Fig. 2.4). As V is increased further, the excitonic weight starts appearing and a resonance begins separating from the rest of the spectrum. When $W_{jj(\tau\tau)}$ reaches a maximum around $V\sim 4t$, the spectrum is dominated by a sharp excitonic feature carrying most of the weight, 86% and 77% for the optical and Raman response. This peak, well differentiated from the rest of the spectrum, is clearly located inside the single-particle spectral gap while the rest of the weight falls outside. The Lanczos method is rather well suited to describe these excitonic features, but it is not so good in capturing detail at the higher end of the spectrum. The optical bands inside

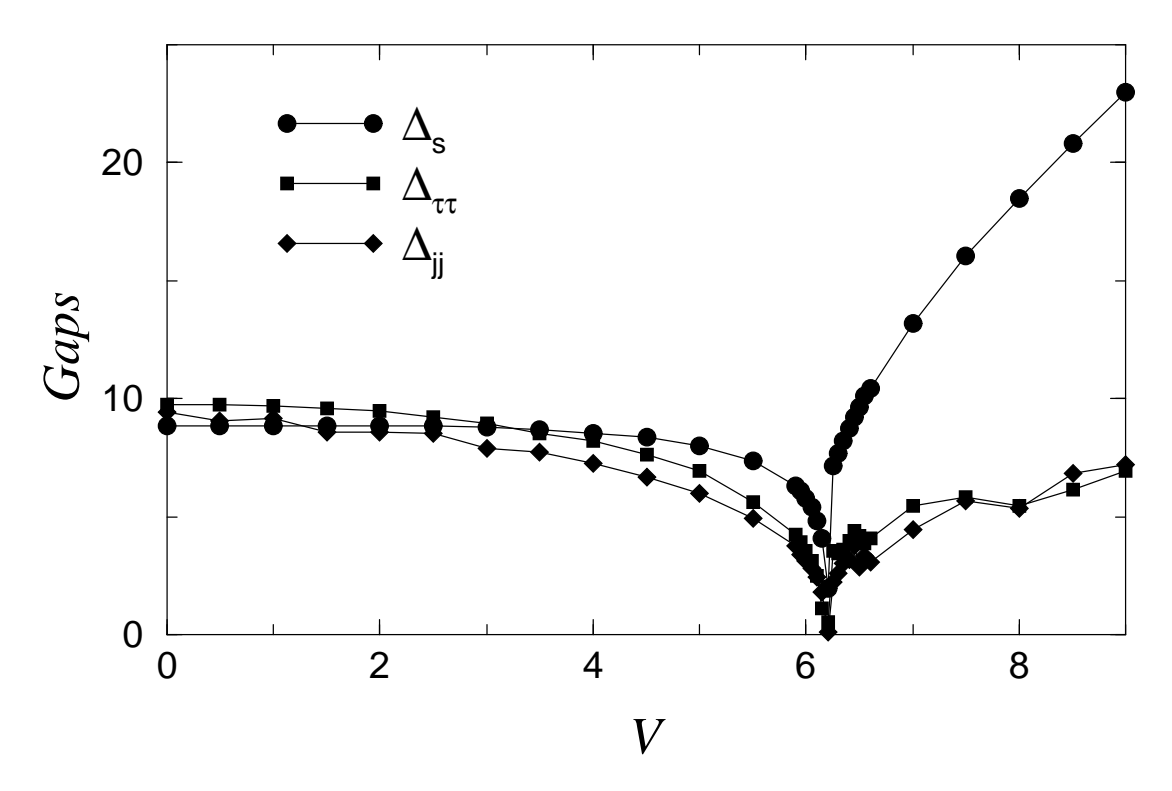


Figure 2.4: Gaps for different values of the coupling V.

the one–particle continuum tend to be shifted towards higher energies. At the same time the relative weight in the excitonic features is accurately represented, since we find that the sum rule for the optical conductivity in terms of kinetic energy is obeyed with 1% accuracy or better (except very close to the transition). As V is increased further beyond $V \sim 4t$, the excitonic feature starts loosing weight and at the same time moves towards zero frequency. At the precise point of the SDW-CDW transition, the excitonic mode reaches the lowest frequencies we can resolve ($\omega \sim 1/L$).

In a Mott insulator represented by the half-filled Hubbard model, creation of an independent double occupancy and an empty lattice site in a background of singly occupied sites (or a holon-antiholon pair in the Bethe ansatz language) has a finite energy threshold; namely the spectral gap. This threshold is lowered in the presence of an attractive force by the binding energy of the double occupancy and empty site, which we call a Mott-Hubbard exciton. This attraction is due to the increased range of Coulomb repulsion in the EHM and is significantly absent in the standard Hubbard model. To some extent, this is reminiscent of the situation encountered in Wannier

theory for a band insulator. However, unlike in Wannier theory, the double occupancy and the hole are not fermionic quasi-particles, but spinless hard-core bosons. Even more importantly, there is a critical value of V below which no exciton appears under the threshold of the particle-hole continuum. As we increase V, the binding energy of the exciton keeps growing continuously, and the excitonic feature moves closer and closer to zero frequency. At the same time, the density of electron and hole states available for binding first increases, reaches a maximum and then goes to zero at the SDW-CDW boundary. This non-monotonic behavior of Mott-Hubbard exciton as a function of the Coulomb repulsion strength is a consequence of the fact that an increase of the Coulomb interaction strength does not simply bind the exciton more tightly, but also renormalizes the gap and couples the particle-hole excitation more strongly to the other electrons. When the energy gained from binding the electron-hole pairs equals the energy cost of creating them across the single particle gap, the optical gap vanishes in both the odd (χ_{jj}) and even $(\chi_{\tau\tau})$ channels.

As one of the examples of 1D Mott insulators mentioned earlier, let us consider the case of Sr_2CuO_3 to indicate the experimental relevance of our results. From previous literature [35, 36], the values of the parameters for this material are estimated to be: $t \approx 0.55 - 0.6$ eV, $U \approx 7.2$ eV and $V \approx 0.8$ eV. Therefore the material lies right near the boundary where excitonic weight in χ_{jj} begins to appear. Nevertheless, the exciton or its precusor in the form of a narrow peak distinguished from the rest of the spectrum should already be seen in the optical conductivity.

2.6 Weak Coupling: Field theoretic approach

The regime of small Mott gaps can be addressed by studying the field theoretical limit (or scaling limit), which corresponds to having the bandwidth as the largest scale in the problem. It is defined by choosing

$$t \to \infty$$
, $U/t \to 0$, $M = \frac{8t}{\pi} \sqrt{\frac{U}{4t}} \exp(-2\pi t/U)$ fixed. (2.10)

and has been studied by many authors [22, 23, 37–39]. On an operator level the field theory is constructed by splitting the electron operators into fast and slow components

$$c_{l,\sigma} \longrightarrow \sqrt{a_0} \left[\exp(ik_F x) \ R_{\sigma}(x) + \exp(-ik_F x) \ L_{\sigma}(x) \right].$$
 (2.11)

Here k_F is the Fermi momentum (it is $\pi/2$ for the half-filled band), R_{σ} and L_{σ} are right and left moving electron fields and $x = la_0$, where a_0 is the lattice spacing. Inserting this prescription into the extended Hubbard Hamiltonian one obtains

$$\mathcal{H}_{\text{ext}} = \mathcal{H}_{c} + \mathcal{H}_{s} ,$$

$$\mathcal{H}_{c} = \frac{2\pi v_{c}}{3} \int dx \left[: \mathbf{I} \cdot \mathbf{I} : + : \bar{\mathbf{I}} \cdot \bar{\mathbf{I}} : \right] + \int dx \left[g_{\perp} \left(I^{+} \bar{I}^{-} + I^{-} \bar{I}^{+} \right) + g_{\parallel} I^{z} \bar{I}^{z} \right] ,$$

$$\mathcal{H}_{s} = \frac{2\pi v_{s}}{3} \int dx \left[: \mathbf{J} \cdot \mathbf{J} : + : \bar{\mathbf{J}} \cdot \bar{\mathbf{J}} : \right] - 2g_{\perp} \int dx \, \mathbf{J} \cdot \bar{\mathbf{J}} .$$
(2.12)

where

$$g_{\perp} = (U - 2V)a_0$$
 , $g_{\parallel} = (2U + 12V)a_0$, (2.13)

$$v_c = v_F + \frac{(U+4V)a_0}{2\pi}$$
 , $v_s = v_F - Ua_0/2\pi$. (2.14)

Furthermore, $v_F = 2ta_0$ is the Fermi velocity, and **J** and **I** are the chiral components of SU(2) spin and pseudospin currents

$$I^{3} = \frac{1}{2} \sum_{\sigma} : L_{\sigma}^{\dagger} L_{\sigma} : , \quad I^{+} = L_{\uparrow}^{\dagger} L_{\downarrow}^{\dagger} ,$$

$$\bar{I}^{3} = \frac{1}{2} \sum_{\sigma} : R_{\sigma}^{\dagger} R_{\sigma} : , \quad \bar{I}^{+} = R_{\uparrow}^{\dagger} R_{\downarrow}^{\dagger} ,$$

$$J^{3} = \frac{1}{2} \left(L_{\uparrow}^{\dagger} L_{\uparrow} - L_{\downarrow}^{\dagger} L_{\downarrow} \right) , \quad J^{+} = L_{\uparrow}^{\dagger} L_{\downarrow} ,$$

$$\bar{J}^{3} = \frac{1}{2} \left(R_{\uparrow}^{\dagger} R_{\uparrow} - R_{\downarrow}^{\dagger} R_{\downarrow} \right) , \quad \bar{J}^{+} = R_{\uparrow}^{\dagger} R_{\downarrow} . \tag{2.15}$$

There is a clear spin-charge separation, and the two parts of the Hamiltonian (2.12) can be bosonized separately. In the field theory limit, the electric current operator of the lattice model is given by

$$j = \frac{4et}{\hbar} \int dx \left[I^3(x) - \bar{I}^3(x) \right]$$
 (2.16)

The current couples only to the charge part of the Hamiltonian and therefore we can ignore the spin part. It is worthwhile to note here that the spin sector is gapless if

U>2V and gapped otherwise. Applying the standard bosonization rules to \mathcal{H}_c one arrives at the Hamiltonian of the Sine-Gordon model (SGM) (2.17) [40]. given by

$$\mathcal{H}_{c} = \frac{1}{16\pi} \left[(\partial_{t}\phi)^{2} + (v_{c}\partial_{x}\phi)^{2} \right] + 2\mu\cos\beta\phi, \tag{2.17}$$

where μ and β are functions of U and V.

$$\beta^2 = \frac{4\pi v_{\rm F}}{4\pi v_{\rm F} + \sqrt{g_{\parallel}^2 - g_{\perp}^2}} \tag{2.18}$$

The pure Hubbard model corresponds to the limit $\beta \to 1$ and the effect of increasing V is to decrease the value of β . The SGM possesses a conserved (topological) charge

$$Q = \int_{-\infty}^{\infty} j^0 dx = -\frac{\beta}{2\pi} \int_{-\infty}^{\infty} \frac{\partial \phi}{\partial x} dx , \qquad (2.19)$$

where

$$j^{\mu} = -\frac{\beta}{2\pi} \epsilon^{\mu\nu} \partial_{\nu} \phi \tag{2.20}$$

is the Noether current. The electric current (2.16) is proportional to the Noether current j^1

$$j = \sqrt{A} \,\partial_0 \phi \,\,, \tag{2.21}$$

where A is some nonuniversal constant ¹. The SGM is integrable and has been studied in great detail over the last 25 years [37,38,41]. The spectrum of the SGM depends on the value of the coupling constant β^2 or, alternatively, on

$$\xi = \frac{\beta^2}{1 - \beta^2}.\tag{2.22}$$

For $\beta^2 < 1$ the cosine term is relevant in the renormalization group (RG) sense and dynamically generates a spectral gap M in the excitation spectrum. In the repulsive regime $1 < \xi < \infty$ the spectrum contains only charged particles of charge $Q = \pm 1$, which are called *solitons* and *antisolitons*. In this regime the spectral gap M is related to the "optical gap" Δ , i.e., the gap seen in the optical absorption spectra through the relation, $\Delta = 2M$. At the so-called "Luther-Emery" [42] (LE) point $\xi = 1$ the SGM

 $^{^{1}}$ It is assumed that A is nonuniversal because the electric current is not a conserved quantity for the lattice model.

is equivalent to a free massive Dirac fermion. In this limit the solitons become non-interacting particles and the Mott insulator turns into a conventional band insulator. In the limit $\xi \to \infty$, the Sine-Gordon model acquires an SU(2) symmetry and describes the charge sector of the Hubbard model at half-filling in the limit of weak interactions as discussed above. In the attractive regime $0 < \xi < 1$ soliton-antisoliton bound states called "breathers" are formed and they correspond to the excitons which we observe in our lattice model.

2.7 Summary and conclusions

To conclude, we have shown that sharp excitonic features dominate the transport behavior in a particular regime of the EHM at half-filling. This is a direct consequence of the inclusion of non-local Coulomb interaction in this model. These excitons are of fundamentally different origin as compared to those in semiconductors formed by the binding of electron-hole pairs. Although a Mott-Hubbard exciton can be described as a bound pair of excitations with opposite charges, the Coulomb interaction at the same time determines the size of the Mott gap, the exciton properties, and the coupling of the exciton to the other electrons in the system. Therefore, an increase of the Coulomb interaction strength does not simply bind the exciton more tightly, but also renormalizes the gap and couples the particle-hole excitation more strongly to the other electrons. This leads to a non-monotonic behavior of Mott-Hubbard exciton properties as a function of the Coulomb repulsion strength, and even to instabilities toward the formation of charge-density wave droplets. Due to strong correlation and low dimensionality, electrons decouple into new elementary excitations, namely, spinons and holons [43]. This necessitates a careful treatment of the full many-body problem. The Lanczos method combined with the DMRG approach is a powerful non-perturbative tool for computing the dynamical correlation functions of a non-trivial system like this. Our numerical approach permits us to easily include other ingredients such as explicit dimerization and interchain hopping which are present in these materials in order to allow for a better quantitative comparison with experiments in the future.

A closely related problem of much interest, on which the DMRG approach may

shed light and which is under investigation, is that of the phase diagram of quasione dimensional organic compounds TMTTF and TMTSF and their unusual metallic
behavior [44–46]. These materials are believed to be quarter filled Mott Insulators and
close to the Mott transition point. By varying the anistropy of the system and the
energy scale at which it is probed, a wide range of behaviors has been reported. The
metallic phase shows a broad feature representative of the Mott insulating gap, carrying
a majority of the spectral weight and a very narrow Drude peak. Thus, these compounds
are very far from being Fermi liquids and present interesting challenges.

Chapter 3

The DMRG Program

3.1 Why Fortran 90?

The DMRG algorithm to solve for a one dimensional extended Hubbard model (EHM) was implemented in a computer program which we describe in this chapter. The program is close to 3000 lines, and was written in Fortran 90 which allows for greater flexibility and modularity than standard Fortran 77. We list below the key advantages and features of Fortran 90 which make it conducive for scientific programming:

- Fortran 90 allows for a free format, with no reliance on specific positioning of special characters and up to 132 columns per line. In-line comments are allowed, making it easier to annotate code.
- Arithmetic may now be performed on whole arrays and array sections. This makes the code shorter and much more readable. Operations in an array valued expression are potentially performed in parallel.
- It allows for dynamic memory allocation. This is key to programming the DMRG algorithm where memory requirements can be demanding.
- It is possible to specify the desired precision of an object in a portable way. Type specifications can be parametrized, meaning that the precision of a particular type of variables can be changed by altering the value of one constant.
- Modules replace many unreliable features of Fortran 77 open to inadvertent abuse such as the common block. They can be used for global definitions of types, objects, operators and procedures, and can be used to provide functionality whose internal details can be hidden from the user.

- Interfaces between procedures allow for efficient passing of arrays. Array bounds do not have to be passed as arguments and array shape can be inherited from the actual argument.
- There is a vastly improved set of intrinsic functions, especially useful in the algebraic manipulation of arrays.

3.2 Introduction

As in all computer programs there is a compromise to be made between generality and length. We have written the DMRG program sufficiently general that it can solve for both the static and dynamical properties of a 1D quantum system with arbitrary hopping, local and nearest neighbor interactions along the length of the chain. The program is easily generalizable to other model Hamiltonians with more complicated interactions. We use the finite size algorithm with open boundary conditions since it is much more accurate than the infinite size one. Dynamical properties have been computed using the Lanczos vector method, which was discussed in Chapter 1. Again it is possible to modify the program to target other vectors to obtain dynamical properties with reasonable ease. To reduce the sizes of matrices of operators, symmetries associated with the conservation of S_z and particle number are implemented throughout.

The program uses certain library routines for linear algebra and other purposes which can be obtained from various sources such as LAPACK, Numerical recipes or NAG program libraries. These include:

- A routine to obtain the lowest eigenvalue and eigenvector of a real symmetric tridiagonal matrix. This is used after the Lanczos procedure is performed on the Hamiltonian (consisting of the system plus environment and two sites in the middle) to reduce it to a tridiagonal form and obtain the ground state.
- A routine to fully diagonalize the density matrix and obtain all it's eigenvalues and eigenvectors.
- A routine to sort the eigenvalues of the density matrix.

The first step in the procedure is to rewrite the original Hamiltonian in a notation of spinless sites, by separating the up and down spin degrees of freedom. The basis then looks as follows:

$$(\uparrow \otimes \downarrow)_1 \otimes (\uparrow \otimes \downarrow)_2 \otimes (\uparrow \otimes \downarrow)_3 \otimes (\uparrow \otimes \downarrow)_4 \otimes (\uparrow \otimes \downarrow)_5 \cdots$$

The advantage of this step is that at each DMRG iteration a spin up or down site with two degrees of freedom is added to the system block as it grows, rather than a full site with four degrees of freedom on it. This makes the total system size $2m \times 2m$ rather than $4m \times 4m$ and thereby allows for more states to be kept in the system and environment block.

3.3 The routines

Now we discuss the details of individual subroutines, their inputs and outputs and the tasks they perform. The first routine of importance is a module, called global.f90.

• global.f90: As the name implies this module is used to declare variables and arrays along with their shape and make them accessible everywhere they are needed. These global variables are accessed in each routine with the command USE global. A parameter, named DBL, used to fix the precision of all real and complex variables in the program is declared and assigned here. Other variables include the size of the lattice, N_s , the number of states to be kept in a DMRG truncation m, the location of the site where the local spectral function is computed, the number of finite size DMRG sweeps and the tolerance to be achieved in the Lanczos procedure. Then follow the various arrays storing the left and right blocks, superblocks and the operators at the edges of the blocks out of which the Hamiltonian is constructed. For the extended Hubbard model, the operators at the edges of blocks include the creation or destruction operator and the number operator for building the nearest-neighbor and local Coulomb interaction. A logical variable called firstgrow is used to distinguish between the different procedures to be adopted in the first DMRG sweep when the system size is growing and the later sweeps when the full system size has been attained. The logical variable grow is used to distinguish the cases when the left block is the system and the right block is the environment and vice versa.

Much efficiency is gained in the algorithm by storing the quantum numbers of the states rather than the states themselves. So the various arrays denoting the quantum numbers, viz., the number of up and down spin electrons (nup and ndo) of states on the system and environment blocks and the entire system are also declared in module global.

Other miscellaneous variables include the number of Lanczos basis states to be targetted (Nlanc) for building the dynamical correlation functions and the relative weight (weightgs) to be assigned for the ground state density matrix. The last variables to be accessible everywhere are the parameters in the Hamiltonian such as the Hubbard interaction U, the nearest-neighbor coupling V, the hopping t and the chemical potential.

- input.f90: This routine is the first one to be called from the main program, dmrg.f90. Again as the name suggests, all the inputs to the program are provided through this routine. Typically, three finite DMRG sweeps are needed to attain convergence. 50% of the weight in the full density matrix is assigned to the ground state and the rest to the Lanczos basis states.
- dmrg.f90: This is the main program which controls the sequence of calls to the various routines. The first call is to the subroutine input.f90. The spinless sites along the chain are labelled from left to right with integers. With each DMRG iteration, two spinless sites in between system and environment slide along the length of the chain to the right and then to the left. Each DMRG step is labelled by the integer variable LL denoting the location of the first of the two sites between system and environment. A call is then made to the program superblock.f90 to build the left and right blocks and the edge operators with the argument LL (see description of superblock.f90 for details of this procedure).

With the help of these block and edge operators, the Hamiltonian is constructed in each sector with fixed S_z . The ground state eigenvalue and eigenvector is then

obtained by a call to lanc. f90. The next step involves building the density matrix out of the ground state and any other states to be targetted. This is achieved through a call to the subroutine buildrho.f90 (for details see the description below of this routine). The full density matrix is stored in the array called rho. The quantum numbers of the basis states in which rho is written are either those on the left or right superblock depending upon whether one is sweeping to the right or left, respectively. The density matrix is diagonalized in each subsector of fixed up and down spin on the system block. After obtaining all the eigenvectors and eigenvalues, a routine eigsrt is used to sort the eigenvalues of the density matrix across all spin sectors. The m eigenvectors with the largest eigenvalues are stored in a rectangular array called OT. One minus the sum of the m largest eigenvalues stored in the array 'W alfa' gives the discarded weight, DscWght. Depending on whether one is sweeping to the right or the left, the left superblock or the right superblock (i.e., the system block) is truncated by using the m eigenstates of the density matrix stored in OT. This truncation is carried out for the Hamiltonian as well as other operators situated on the edge of the block and any other operators whose ground state expectation values are sought. All the operators on the block are of size $m \times m$ and we are now ready to begin a new DMRG iteration.

• supblock.f90: In our notation the left and right superblock denote the left block plus a spinless site and the right block plus a spinless site respectively. At the beginning, supblock.f90 makes calls to routines left_block and right_block (see description of block.f90) with argument LL to build the left and right blocks. Next, by using the stored operators at the edges of the left and right blocks, the right and left superblock are constructed. This involves tensor products which are performed using a routine called dirpsum. The edge operators are then transformed to the superblock basis and their quantum numbers in the new basis are created. Using the quantum numbers in the left and right superblock, quantum

numbers for the full system plus environment are now built using:

$$q^L \oplus q^R = \left[\begin{array}{c} q_1^L + q^R \\ q_2^L + q^R \\ \vdots \end{array} \right]$$

This tensor summation is achieved by defining an operator .QN. (in a module called direct_product.f90) to be inserted in between the two arrays of quantum numbers.

- block.f90: This consists of two routines left_block and right_block. It takes the argument LL and it's action depends crucially on the variable 'firstgrow' and 'grow'. These routines are responsible for building the left and right block Hamiltonians as well as their quantum numbers. Initially when LL is the lowest value and firstgrow is true, the left and right block are constructed with four spinless sites each. So the starting size of the Hamiltonian that is diagonalized exactly is 10 sites, with four in each block and two in the middle. At each stage as you grow the chain, the left block plus a spinless site act as the system and the associated operators are written to disk to be read again while sweeping to the left. If one is sweeping to the left, then the left block is read from the disk from the previous sweep. The right block is constructed exactly of four spinless sites during the first sweep to the right and each time one reaches the right end during the sweeps. From the second sweep onwards when one is sweeping to the right, the right block is read from the disk as saved from the first sweep. When one is sweeping to the left, the right block plus a spinless site acts as the system, and therefore the right block is written to disk. Note that the superblocks of one iteration form the blocks for the next DMRG iteration.
- buildrho.f90: This routine builds the density matrix out of the ground state or other states such as the Lanczos basis when correlation functions are desired. The input to this routine is the ground state vgs, the ground state quantum numbers and the sizes of the system and the environment. Once the system grows to its full size, the system and the environment are equally represented by 2m

states each. In order to build the density matrix, the ground state eigenvector which is in the full basis of the system plus the environment needs to be projected onto the states residing entirely on the system and entirely on the environment. This is performed by an intrinsic function called RESHAPE. Given the sizes of the system and environment, and the ordering convention in the tensor summation of quantum numbers, RESHAPE rearranges the one-dimensional array consisting of the ground state eigenvector into a 2D array, psi in the left and right superblock basis. This projection followed by a trace over the states of the environment gives the density matrix.

If dynamical correlations are being computed then, for example, in the case of the local spectral function, the destruction operator has to be acted on the ground state eigenvector. This matrix multiplication has to be done with much care because the operator could exist on either the left superblock or the right superblock depending on the DMRG iteration step. Since the destruction or creation operator itself is defined on the superblock basis, the multiplication is performed on the projected ground state psi. The intrinsic function PACK, which performs the exact reverse task of the intrinsic RESHAPE, is used to build the first Lanczos vector in the full basis of the system plus the environment. This Lanczos vector is then fed to the routine lanc to build the rest of the Lanczos basis. After building the Lanczos basis, each of them is reshaped to project onto the left and right superblock just as was done for the ground state, to build a density matrix. The full density matrix is a weighted sum of the ground state density matrix and the density matrices obtained from the Lanczos basis vectors.

• buildham.f90: This routine builds the Hamiltonian in a subsector with fixed quantum number S_z for the entire system plus the environment. The inputs to this subroutine include, LL, the sizes of the left and right superblocks and the quantum number S_z . Only the upper triangle of the matrix and non-zero off-diagonal matrix elements are stored. We use the following sparse matrix notation

to store the Hamiltonian as illustrated by the following example:

$$H_{
m ex} = \left(egin{array}{ccccccc} 0 & 1 & 0 & 2 & 0 & 0 \ 1 & 2 & 0 & 3 & 0 & 5 \ 0 & 0 & 0 & 0 & 1 & 0 \ 2 & 3 & 0 & 1 & 0 & 0 \ 0 & 0 & 1 & 0 & 1 & 0 \ 0 & 5 & 0 & 0 & 0 & 0 \end{array}
ight)$$

would be represented using:

hdiag =
$$(0, 2, 0, 1, 1, 0)$$

hoffdiag = $(1, 2, 3, 5, 1)$
hpos = $(2, 4, 4, 6, 5)$
nrow = $(2, 2, 1, 0, 0, 0)$

hdiag stores all the diagonal elements. hoffdiag stores all the non-zero off diagonal matrix elements in the upper triangular part. hpos stores the column number of each offdiagonal element. nrow contains the number of non-zero off-diagonal matrix elements in each row. In order to pick the matrix elements of the Hamiltonian, one has to consider all possible combinations of quantum numbers in the left and right superblock which give rise to the fixed value of S_z . The matrix elements themselves are constructed by calling a function called hamil. This function hamil takes as arguments the basis states on the left and right superblock to give a matrix element in the full basis.

To ensure that the DMRG procedure is always stable and convergent, the system ground state usually has to be determined to a rather high accuracy. It also happens to be the most time-consuming part of a DMRG calculation. A substantial amount of CPU time can be saved by having a very good initial guess for either the Lanczos or Davidson algorithm to determine the ground state. An ideal initial guess, for the case of the finite system DMRG algorithm, is the final wavefunction from the previous DMRG step. This wavefunction, although corresponding to a different system configuration,

can be transformed into the current configuration. Use of this initial state reduces the number of iterations by almost a factor of two and also the chances of converging onto an incorrect low-lying eigenstate. Measurements of ground state expectation values and dynamical correlation functions are most accurate when the DMRG iterations terminate at the geometric center of the 1D lattice. This is because the system and environment blocks consist of the same number of sites and are equally well represented by 2m states.

Chapter 4

The Dynamical Mean Field Method

4.1 Introduction

It is a well-known fact that theoretical investigations of quantum-mechanical many body systems are faced with severe technical challenges, particularly in those dimensions which are most interesting, i.e., d=2,3. In the absence of exact methods in this domain there is clearly a great need for reliable, controlled approximation schemes. There exist several approximation techniques which make use of the simplifications that occur when some parameter, e.g., the length of spins S or the spin degeneracy N are taken to be large. Investigations in this limit, supplemented by an expansion in the inverse of the large parameter, can provide insight into the fundamental properties of systems where this parameter is not large.

In the last decade a new approach to fermionic systems, based on the limit of $d \to \infty$ has been used successfully to describe several aspects of strongly correlated systems, most notably the Mott transition (for reviews see [2,47]). Presently, a lot of research is focussed on applications of this method to the study of real materials. In this chapter we present an overview of this method called the Dynamical Mean Field Theory (DMFT).

4.2 Classical spin models

The limit of infinite coordination number, $Z \to \infty$, allows for the construction of a mean field theory (MFT) in the case of classical spin models such as the Ising model. For instance, the ferromagnetic Ising model Hamiltonian (J > 0)

$$H = -J \sum_{\langle ij \rangle} S_i S_j \tag{4.1}$$

can be replaced by a single site mean field Hamiltonian, if we assume that each spin S_i interacts with a *static local* field produced by its nearest neighbors at the site i:

$$H^{MF} = -h_{MF} \sum_{i} S_i + \frac{1}{2} NJZ \langle S \rangle^2, \tag{4.2}$$

where $h_{MF} = JZ\langle S \rangle$ and N is the total number of lattice sites. This corresponds to neglecting the correlated fluctuations of spins at sites i and j, i.e.,

$$\langle [S_i - \langle S \rangle][S_j - \langle S \rangle] \rangle = 0 \tag{4.3}$$

For h_{MF} to remain constant in the limit $Z \to \infty$, J has to be rescaled as

$$J \to \frac{J^*}{Z}$$
, with J^* held constant. (4.4)

The mean field parameter h_{MF} is determined self-consistently using

$$\langle S \rangle = \tanh(\beta J^* \langle S \rangle), \quad \beta = 1/T.$$
 (4.5)

The scaling of the coupling constant J above is typical for isotropic spin models with a non-zero spatial average, $\bar{J}_{ij}=J$. In the case of random spin models, such as spin glass systems with $\bar{J}_{ij}=0$, the appropriate scaling to achieve a mean field theory can be shown to be $J\to J^*/\sqrt{Z}$.

4.3 Itinerant quantum mechanical models

The limit $Z \to \infty$ leads to significant simplifications in the investigation of quantum lattice models such as the Hubbard model and is much more subtle than the case of classical spin models [48]. The Hubbard model is defined by the following Hamiltonian:

$$H = -t \sum_{\langle ij \rangle, \sigma} \left(c_{i\sigma}^{\dagger} c_{j\sigma} + \text{h.c.} \right) + U \sum_{j} n_{j\uparrow} n_{j\downarrow}$$
 (4.6)

The first and second terms correspond to hopping between nearest neighbor sites and the onsite Coulomb repulsion, respectively and provide a competition between itineracy and localization. This model was first introduced independently by Hubbard and Gutzwiller in an attempt to describe the physics of transition metals with partially filled d-bands. These systems show both a band-like delocalised and an atom-like localised behavior

depending on the strength of the Coulomb interactions which can be controlled by the application of pressure.

The Fourier transform of the kinetic energy term on a d-dimensional hypercubic lattice with unit lattice spacing involves a dispersion ϵ_k given by

$$\epsilon_k = -2t \sum_{i=0}^{d} \cos k_i. \tag{4.7}$$

The density of states (DOS) corresponding to this dispersion in the limit of infinite dimensions is a sum of independent random numbers and is given by the central limit theorem as a Gaussian,

$$\lim_{d \to \infty} N_d(E) = \lim_{d \to \infty} \sum_k \delta(E - \epsilon_k) = \frac{1}{2t\sqrt{\pi d}} \exp\left[-\left(\frac{E}{2t\sqrt{d}}\right)^2\right]. \tag{4.8}$$

A non-trivial DOS is obtained under the scaling,

$$t \to \frac{t^*}{\sqrt{Z}}, \quad t^* \text{ held constant}, \quad Z = 2d.$$
 (4.9)

The interaction term in Eq. 4.6 is purely local and independent of the surrounding sites and consequently remains the same irrespective of the dimension of the system. Thus, the scaled Hamiltonian

$$H = -\frac{t^*}{\sqrt{Z}} \sum_{\langle ij \rangle, \sigma} \left(c_{i\sigma}^{\dagger} c_{j\sigma} + \text{h.c.} \right) + U \sum_{j} n_{j\uparrow} n_{j\downarrow}$$
 (4.10)

has a non-trivial $Z \to \infty$ limit, such that both the kinetic energy and interaction terms can compete on an equal footing as in finite dimensions.

4.4 Local self energy

In order to visualize the implications of the limit $Z \to \infty$, we consider a perturbation theory in terms of U. At T = 0 and U = 0, the kinetic energy may be written as

$$E_{kin}^{0} = -t \sum_{\langle ij\rangle\sigma} g_{ij,\sigma}^{0} \tag{4.11}$$

where $g_{ij,\sigma}^0 = \left\langle c_{i\sigma}^{\dagger} c_{j\sigma} \right\rangle_0$ is the free one particle density matrix. For E_{kin}^0 to remain constant in the limit $d \to \infty$ we find

$$g_{ij,\sigma}^0 \sim O(\frac{1}{\sqrt{d}}),\tag{4.12}$$

since $t \sim 1/\sqrt{d}$ and there are O(d) nearest neighbor sites j to the site i. The same dependence holds for the full one particle Green's function of the non–interacting system, $G_{ij,\sigma}^0(\omega)$,

$$E_{kin}^{0} = -\frac{t}{2\pi i} \sum_{\langle ij\rangle\sigma} \int_{-\infty}^{\infty} d\omega G_{ij,\sigma}^{0}(\omega)$$
 (4.13)

It is to be noted that although the propagator $G^0_{ij,\sigma} \sim 1/\sqrt{d}$ vanishes as $d \to \infty$, the particles are still mobile, since a particle may hop to d nearest neighbors with reduced amplitude $t^*/\sqrt{2d}$. In general, if $||R_{ij}||$ represents the so called "Manhattan distance" (distance measured only along horizontal and vertical lines connecting i and j) it can be shown that

$$G_{ij,\sigma}^0 \sim O(1/d^{||R_{ij}||/2}).$$
 (4.14)

This property is an essential consequence of the scaling of the hopping parameter t and leads to all simplifications arising in the limit $d \to \infty$. In particular, it implies the collapse of all connected, irreducible perturbation diagrams in position space as illustrated below. We consider the second order contribution to the perturbation series of the irreducible self energy $\sum_{ij}^{(2)}$ in U. By considering the scaling of the individual Green's functions and the summation over R_{ij} it can be seen that $\sum_{ij}^{(2)} \sim 1/\sqrt{d}$, and it vanishes, unless i = j. Hence, in the limit $d \to \infty$ any two vertices which are connected

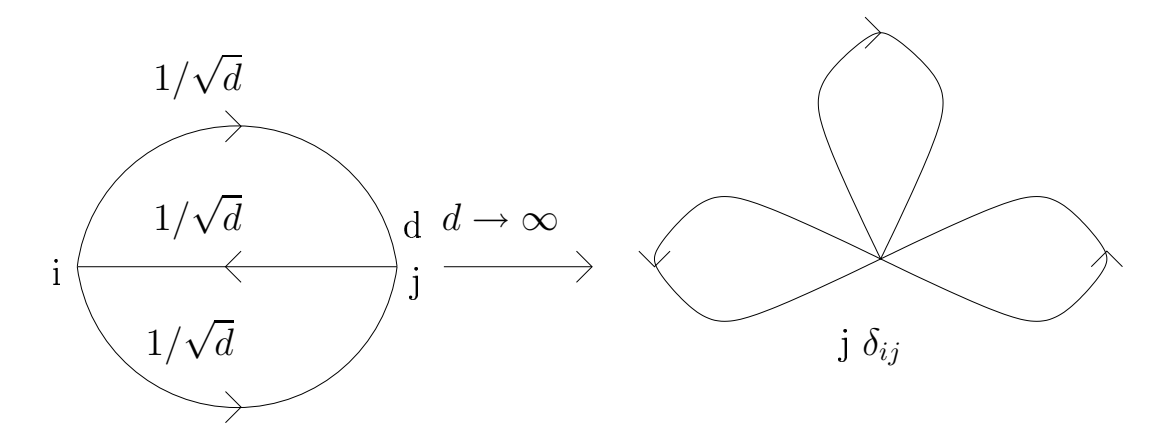


Figure 4.1: Collapse of the second order contribution to the irreducible self energy in the limit $d \to \infty$.

by more than two separate paths will collapse on the same site. Since the external

vertices of any irreducible self energy diagram are always connected by at least three separate paths, they always collapse to give a local self energy,

$$\lim_{d \to \infty} \Sigma_{ij,\sigma}(\omega) = \Sigma_{ij,\sigma}(\omega)\delta_{ij} \tag{4.15}$$

Consequently, the Fourier transform of $\Sigma_{ij,\sigma}$ becomes momentum independent.

$$\lim_{d \to \infty} \Sigma_{\sigma}(k, \omega) = \Sigma_{\sigma}(\omega) \tag{4.16}$$

This simplification is physically justifiable as an excellent approximation in several circumstances, for example, in d=3 the coordination number Z is already quite large (Z=12 for a face centered cubic lattice). One of the most prominent examples contrary to this, is the case of the high temperature superconductors which have a strongly anisotropic 2D character. We shall revisit this issue in the next chapter when we discuss cluster methods to incorporate short range correlations within DMFT. The most important obstacle which makes the problem of performing diagrammatic calculations in finite dimensions intractable is the integration over intermediate momenta with the constraint of momentum conservation. This is no longer the case for $d=\infty$, where one can replace the multidimensional integrals over momentum by one dimensional integrals over the DOS. At the same time it should be noted that the limit $d\to\infty$ retains the full dynamics of the system as there is no collapse in the frequency variables and time is always unidimensional.

The simplifications introduced by the limit $d \to \infty$ can be used to derive a single site effective action by tracing out all the degrees of freedom external to the site in analogy to the classical Ising model. The original action of the Hubbard model

$$S = \int_0^\beta d\tau \left(\sum_{i\sigma} c_{i\sigma}^\dagger \partial_\tau c_{i\sigma} - \sum_{ij\sigma} t_{ij} c_{i\sigma}^\dagger c_{j\sigma} - \mu \sum_{i\sigma} n_{i\sigma} + U \sum_i n_{i\uparrow} n_{i\downarrow} \right), \tag{4.17}$$

can be split into three parts, $S^{(o)} + S_o + \Delta S$, where $S^{(o)}$ is the lattice action with the site 'o' removed, S_o consists of terms purely on the site 'o' and ΔS consisting of terms connecting the site 'o' to the rest of the lattice. By using the scaling of the propagator discussed in the previous section, it is possible to formally integrate the degrees of

freedom $i \neq 0$, to obtain a purely local action of the form [2]:

$$S_{\text{eff}} = -\int_0^\beta d\tau \int_0^\beta d\tau' \sum_{\sigma} c_{o\sigma}^{\dagger}(\tau) G_0^{-1}(\tau - \tau') c_{o\sigma}(\tau') + U \int_0^\beta d\tau n_{o\uparrow}(\tau) n_{o\downarrow}(\tau). \quad (4.18)$$

where

$$G_0^{-1}(i\omega_n) = \Sigma(i\omega_n) + \left(\int_{-\infty}^{\infty} d\epsilon \frac{D(\epsilon)}{i\omega_n + \mu - \epsilon - \Sigma(i\omega_n)}\right)^{-1}$$
(4.19)

Here, $D(\epsilon)$ is the bare lattice density of states. This provides a closed set of mean field equations relating the Weiss field $G_0(i\omega_n)$ to a quantity computable from the local effective action itself.

4.5 Impurity model parametrization and Exact Diagonalization algorithm

Although the interaction between the electrons on different lattice sites has been reduced to an interaction of electrons with a mean field, the dynamics of the latter interaction is still non-trivial. The many-body nature of the Hubbard model survives even in $d=\infty$, making an analytic evaluation of the local propagator generally impossible. In this context, it was pointed out by Georges and Kotliar [49] that the single site action derived in the earlier section corresponds to the action for an auxiliary impurity problem. In particular, the action can be viewed to be that of an Anderson impurity model,

$$H_{AIM} = \sum_{k\sigma} \epsilon_k a_{k\sigma}^{\dagger} a_{k\sigma} + \sum_{k\sigma} V_k (a_{k\sigma}^{\dagger} d_{\sigma} + d_{\sigma}^{\dagger} a_{k\sigma}) - \mu \sum_{\sigma} d_{\sigma}^{\dagger} d_{\sigma} + U n_{d\uparrow} n_{d\downarrow}$$
 (4.20)

This mapping has the advantage that the form of the effective propagator (Weiss field) is already known:

$$G_0^{-1}(i\omega_n)^{AIM} = i\omega_n + \mu - \int_{-\infty}^{\infty} d\omega \frac{\Delta(\omega)}{i\omega_n - \omega},$$
(4.21)

where

$$\Delta(\omega) = \sum_{k\sigma} V_k^2 \delta(\omega - \epsilon_k) \tag{4.22}$$

is the hybridization function characterizing the bath of conduction electrons. This fact together with the extensive numerical and analytical experience that has been accumulated in the treatment of impurity models has made the numerical solution of the self-consistency problem generally tractable.

We now describe a method of solving the DMFT self-consistency equations based on the exact diagonalization approach to the impurity model. In this method, the Weiss function defined above in Eq. 4.21, is approximated by a discretized version:

$$G_0^{-1}(i\omega_n)^{N_b} = i\omega_n + \mu - \sum_{l=1}^{N_b} \frac{V_l^2}{i\omega_n - \epsilon_l}$$
(4.23)

with N_b bath orbitals. This discretization of the bath should be thought of as a functional projection for the Weiss field and should not be confused with a finite-size lattice for the original model.

The Hamiltonian corresponding to this discrete bath is diagonalized exactly, either at finite temperature using exact diagonalization or at zero temperature using the Lanczos method to obtain the local Green's function $G(i\omega_n)$. The self consistency condition leads to a new Weiss function, which needs to be projected onto a function with a discrete number of parameters ϵ_k and V_k . This projection is best carried out on the Matsubara axis by defining a distance function to be minimized.

$$d = \frac{1}{(n_{\text{max}} + 1)} \sum_{n=0}^{n_{\text{max}}} \left\| \hat{\Delta}(i\omega_n)^{\text{new}} - \hat{\Delta}(i\omega_n)^{N_b} \right\|$$
(4.24)

Here, n_{max} denotes the number of points on the Matsubara grid. The minimization is typically carried out using the conjugate gradient minimization algorithm. This distance converges rapidly as a function of N_s , signifying that the solution of the DMFT self-consistent equations within the restricted subspace used for the discretized Anderson model is indeed representative of the 'actual' solution. This method of solving for the impurity model within DMFT is valuable, because it provides real frequency information directly, unlike Quantum Monte Carlo (QMC), and is also more efficient in comparison.

4.6 Limitations of single impurity approach

The dynamical mean field theory (DMFT) [2] has been successful in accessing certain aspects of the non-perturbative phenomena in strongly correlated electron systems. For

example, it has given new insights and predicted various qualitative trends in the redistribution of spectral weight as temperature, pressure and doping are varied in optical and photoemission experiments near the Mott transition.

Single site DMFT extracts physical quantities such as the self energy from a local impurity model with a self consistent bath (also referred to as LISA for local impurity self-consistent approximation) and by construction, this approach misses the effects of short range correlations, such as the k-dependence of the self energy, which are bound to become important at low temperatures.

In the case of more general interactions than the Hubbard interaction, such as near neighbor Coulomb repulsion V, the interaction has to be scaled too, in the limit of $d \to \infty$. It is easy to see that the interaction V has to be scaled in the form

$$V \to \frac{V^*}{Z} \tag{4.25}$$

to be of the same order in d as the hopping and local interaction terms. Since the propagator scales as before as $1/\sqrt{d}$, the self-energy is of the general form shown below.

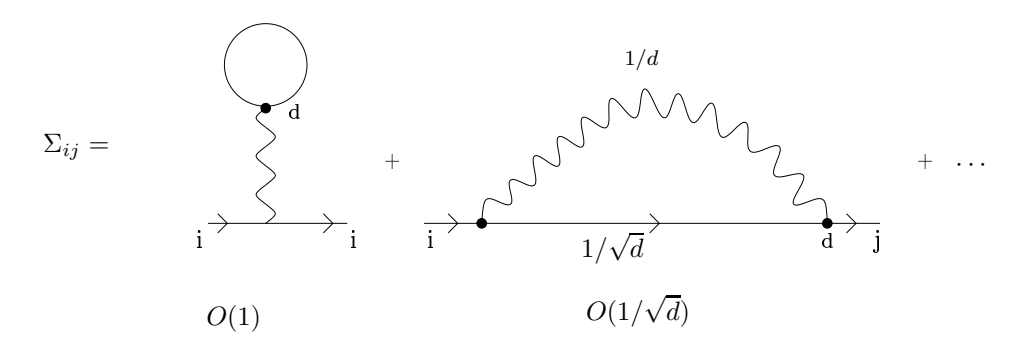


Figure 4.2: Only the Hartree contribution survives the limit $d\to\infty$ for near neighbor Coulomb repulsion.

Due to the scaling in Eq. 4.25, all contributions, except for the Hartree term, are found to vanish in $d \to \infty$. Hence, nonlocal interactions only contribute via their Hartree-contribution, which is purely static. This implies that, of all the interactions for fermionic lattice models, only the Hubbard interaction remains dynamical in the limit $d \to \infty$. This is clearly a limitation of the single impurity approach. In the next

chapter we discuss a method to incorporate these missing short range interactions.

Chapter 5

Cellular Dynamical Mean Field Theory for the Hubbard Model

5.1 Introduction

There have been significant efforts to extend the DMFT methodology to address the limitations that were discussed in the last section of the previous chapter [2, 46, 50–55]. Many of the elements of the DMFT method can be traced back to the coherent potential approximation (CPA) [56] which has been very successful in disordered systems. In this context, the search for extensions of the CPA was fraught with many difficulties, and extensions of DMFT should be scrutinized carefully in this light. The DMFT equations, while having a similar spirit to those of CPA for determining the effective medium, are considerably more complex because they involve the solution of a quantum impurity model, which plays the role of the effective Hamiltonian for the local degrees of freedom treated in the DMFT. To analyse these equations, new concepts and numerous techniques have been developed over the last decade. Their incorporation into cluster methods is promising but requires substantial new work.

In this chapter, we focus on one cluster extension of DMFT, the Cellular Dynamical Mean Field Theory (CDMFT) [53,57]. The aim of this work [58] is to investigate how the exact diagonalization approach which was so successful in the context of the single site DMFT [59–61], can be used in the CDMFT context.

We solve the self-consistent cluster equations for the one dimensional Hubbard and extended Hubbard models using exact diagonalization of the effective underlying cluster impurity. We choose these models because of their generic nature, as well as the fact that DMFT, which becomes exact in the limit of infinite coordination number [48], faces the worst case scenario in one dimension. Furthermore, in one dimension fairly

reliable computations of static as well as dynamic quantities can be made using the Density Matrix Renormalization Group (DMRG) [8, 9, 12, 13] approach to carry out a comparative study.

The exact diagonalization approach, within the single site DMFT context, leads to the development of a technique inspired by renormalization group ideas which resulted in the first quantitative study of the critical properties near the Mott transition [62]. With a view towards the future, we discuss the possibility of combining renormalization group ideas and CDMFT to develop a new numerical method in the spirit of the DMRG method.

The Extended Hubbard Model (EHM) is defined by the following Hamiltonian:

$$H = -t \sum_{j,\sigma} \left(c_{j+1\sigma}^{\dagger} c_{j\sigma} + \text{h.c.} \right) + U \sum_{j} n_{j\uparrow} n_{j\downarrow}$$

$$+ V \sum_{j} n_{j} n_{j+1} - \mu \sum_{j} n_{j}$$

$$(5.1)$$

The two terms corresponding to hopping between nearest neighbor sites and to the onsite Coulomb repulsion provide the competition between itineracy and localization in the regular Hubbard model. The third term represents the Coulomb repulsion between electrons occupying nearest neighbor sites. The Hamiltonian as written above with $\mu = U/2 + 2V$ guarantees an insulating ground state with a filling of one electron per site.

In the following section we introduce and discuss the CDMFT self-consistency equations and show how they can be generalized to treat non-local Coulomb interactions even in the presence of broken symmetries. In the next and subsequent sections we present results for the regular and the extended Hubbard models respectively.

5.2 The CDMFT Method

The CDMFT [53] method is a straightforward generalization of the single site DMFT, in which local degrees of freedom within a cluster are treated exactly and those outside the cluster are replaced by a bath of non-interacting electrons determined self-consistently.

This approach, formulated with realistic studies in mind, deals in principle with overlapping cells and with clusters which are not necessarily defined in real space and could even be defined by non-orthogonal orbitals. In this paper, we ignore these complications and work with real space clusters using an orthogonal basis. It is worth pointing out that if we apply the approach to non-interacting disordered alloys, the self-consistency condition of CDMFT becomes identical to that used in the molecular CPA approximation of Ducastelle [63]. This is analogous to the way the self-consistency condition in single site DMFT becomes identical to the single site CPA and the two-impurity approximation proposed by Ingersent and Schiller [64] and by Georges and Kotliar [2], becomes identical to the pair CPA. However, unlike the single site case, where the transition from real space to momentum space is unambiguous, one has to be careful in interpreting the results of the CDMFT equations in k-space. This is because the goal of CDMFT is to obtain the best possible estimates of local quantities that live within a cluster. For this purpose, a cluster self energy is introduced. Long distance properties such as the ones contained in the lattice Green's function and the lattice self energy are then inferred from the cluster Green's function or the cluster self energy while maintaining causality [53].

5.2.1 The Cavity Construction

The most economical way to arrive at the concepts of a dynamical mean field theory is via the cavity construction, which stresses the point made above, that the focus of the method is in extracting local quantities. The original lattice is divided into equal clusters of size N_c . Integrating out the degrees of freedom external to a chosen cluster (labelled 0), we can formally write an effective action which would allow the computation of local quantities as

$$\frac{1}{Z_{\text{eff}}} e^{-S_{\text{eff}} \left[c_{0\mu\sigma}^{\dagger}, c_{0\mu\sigma} \right]} \equiv \frac{1}{Z} \int \prod_{j \neq 0, \mu\sigma} \mathcal{D} c_{j\mu\sigma}^{\dagger} \mathcal{D} c_{j\mu\sigma} e^{-S}. \tag{5.2}$$

Here j labels individual clusters and μ is an index labelling sites within each cluster. We can split the original action into three parts,

$$S = S^{(0)} + S_0 + \Delta S, (5.3)$$

where $S^{(0)}$ includes terms outside the chosen cluster (the full action with the cluster replaced by a cavity), S_0 comprises terms solely within the cluster, and finally, ΔS includes those terms that couple the cluster with its environment. Explicitly, in the case of the EHM,

$$S_{0} = \int_{0}^{\beta} d\tau \sum_{\mu\nu,\sigma\rho} c_{0\mu\sigma}^{\dagger} (\delta_{\mu\nu}\delta_{\sigma\rho}\partial_{\tau} + E_{\mu\nu,\sigma\rho}^{00}) c_{0\nu\rho}$$

$$+ \sum_{\mu} U n_{0\mu\uparrow} n_{0\mu\downarrow} + V \sum_{\langle\mu,\nu\rangle} n_{0\mu} n_{0\nu}$$

$$(5.4)$$

$$\Delta S = \int_{0}^{\beta} d\tau \sum_{\langle j\mu,0\nu\rangle,\sigma\rho} E_{\mu\nu,\sigma\rho}^{j0} c_{j\mu\sigma}^{\dagger} c_{0\nu\rho} + E_{\nu\mu,\rho\sigma}^{0j} c_{0\nu\rho}^{\dagger} c_{j\mu\sigma}$$

$$+ V \sum_{\langle j\mu,0\nu\rangle} n_{j\mu} n_{0\nu}$$
(5.5)

Here \hat{E}^{00} includes the hopping matrix as well as the chemical potential within the zeroeth cluster and $\langle j\mu,0\nu\rangle$ denotes all intercluster nearest neighbors. It is to be noted that, while the onsite Coulomb interaction U contributes only to S_0 , a nonlocal interaction such as the nearest neighbor Coulomb repulsion V contributes to both S_0 as well as ΔS . This cavity construction is so far merely a relabeling of terms in the original action and is exact. However approximations need to be made to actually access the local properties within the cluster. We approximate the effective action of the cluster by keeping only the renormalization of the quadratic terms obtained after integrating out the degrees of freedom of the surrounding environment [2]. Notice that this approximation violates the translational symmetry of the original lattice. But this is not a problem, since the spirit of the approach is to estimate local quantities. The Gaussian approximation for the effects of the environment seen by the cluster becomes exact in the limit of large coordination [2], and therefore, our test case in one dimension constitutes the most difficult case. The effective action for the cluster can then be approximated as,

$$S_{\text{eff}} \left[c_{0\mu\sigma}^{\dagger}, c_{0\mu\sigma} \right] = \int_{0}^{\beta} d\tau \sum_{\mu\nu,\sigma\rho} c_{0\mu\sigma}^{\dagger} \left[\hat{\mathcal{G}}_{0}^{-1} \right]_{\mu\nu,\sigma\rho} c_{0\nu\rho}$$

$$+ \sum_{\mu} U n_{0\mu\uparrow} n_{0\mu\downarrow} + V \sum_{\langle \mu,\nu \rangle} n_{0\mu} n_{0\nu}.$$

$$(5.6)$$

Here, the time dependent Weiss field $\hat{\mathcal{G}}_0^{-1}$ is now a matrix in the cluster variables and is a functional of the EHM Green's function with the cluster replaced by a cavity.

Suppressing spin indices, it can be written on the Matsubara axis as

$$\begin{split} \left[\hat{\mathcal{G}}_{0}^{-1}\left(i\omega_{n}\right)\right]_{\mu\nu} &= i\omega_{n}\delta_{\mu\nu} - E_{\mu\nu}^{00} - V\,\delta_{\mu\nu}\sum_{\langle j\mu',0\nu\rangle}\left\langle n_{j\mu'}\right\rangle_{(0)} \\ &- \sum_{\langle i\mu',0\mu\rangle}\sum_{\langle j\nu',0\nu\rangle} E_{\mu\mu'}^{0i}G_{i\mu',j\nu'}^{(0)}\left(i\omega_{n}\right)E_{\nu'\nu}^{j0}. \end{split}$$

Relating the cavity Green's function, $G^{(0)}$, to the full Green's function of the EHM, the following self-consistency condition to determine the Weiss field can be obtained:

$$\hat{\mathcal{G}}_0^{-1}(i\omega_n) = \hat{G}_{loc}^{-1}(i\omega_n) + \hat{\Sigma}_c(i\omega_n), \tag{5.7}$$

where the local Green's function on the cluster in one dimension is defined as (with an obvious generalization to higher dimensions)

$$\hat{G}_{loc}(i\omega_n) = \int_{-\pi/N_c}^{\pi/N_c} \frac{1}{i\omega_n + \mu - \hat{\Sigma}_c(i\omega_n) - \hat{t}(k)} \frac{dk}{2\pi/N_c}.$$
 (5.8)

 $\hat{\Sigma}_c$ is the cluster self energy as obtained from $S_{\rm eff}$, $\hat{t}(k)$ is the Fourier transform of the cluster hopping matrix of the EHM and k is a vector in the reduced Brillouin zone of the superlattice $(-\frac{\pi}{N_c}, \frac{\pi}{N_c}]$. Explicitly for a one dimensional model with only nearest neighbor hopping,

$$t^{\mu\nu}(k) = -t[\delta_{\mu-\nu\pm 1} + e^{-ikN_c}\delta_{N_c+\mu-\nu\pm 1} + e^{ikN_c}\delta_{-N_c+\mu-\nu\pm 1}]$$
(5.9)

5.2.2 A functional interpretation

A second approach to derive the above approximation is via the construction of a functional of the quantities of interest, say the Green's function restricted to a local cluster and its supercell translations, such that the stationary point of the functional yields those quantities [65, 66]. In principle such a functional can be constructed order by order in a perturbative expansion in the hopping or the interactions while constraining the Green's function to a fixed value. In practice, sensible approximations to the exact functional are contructed by starting with the full Baym-Kadanoff functional $\Phi[G]$ and restricting its argument from the full Green's function to the Green's function defined only inside the cluster and its periodic supercell repetitions. This constraint is realized

by the cluster self energy which plays the role of the Lagrange multiplier [65–68]. Differentiation of this functional gives the CDMFT equations. Viewed as an approximation to the Baym-Kadanoff functional for the full lattice, this procedure may seem a bad approximation [69]. However, this construction of the functional should be viewed as an approximation to the exact effective action for local quantities, and CDMFT uses it precisely for such a purpose.

The functional approach is useful because it clarifies the level of approximation used in treating the broken symmetry state. In the case that we consider, all the Hartree graphs are added to the functional (see Eq. 5.11). The E-DMFT [54, 55, 65, 66, 70] includes additional graphs to the Hartree terms, but the quality of the results presented below show that they would make a very small contribution.

5.2.3 An Exact Diagonalization Algorithm

For the purpose of practical implementation of the algorithm it is convenient to consider the cluster effective action to arise from a generalized impurity Hamiltonian,

$$H_{imp} = \sum_{\mu\nu\sigma} E_{\mu\nu} c^{\dagger}_{\mu\sigma} c_{\nu\sigma} + U \sum_{\mu} n_{\mu\uparrow} n_{\mu\downarrow}$$

$$+ \sum_{\mu\nu} V_{\mu\nu} n_{\mu} n_{\nu} + \sum_{k\sigma} \epsilon_{k\sigma} a^{\dagger}_{k\sigma} a_{k\sigma}$$

$$+ \sum_{k\sigma,\mu} (V^{h}_{k\sigma,\mu} a^{\dagger}_{k\sigma} c_{\mu\sigma} + V^{h*}_{k\sigma\mu} c^{\dagger}_{\mu\sigma} a_{k\sigma})$$

$$(5.10)$$

Here, $\epsilon_{k\sigma}$ represents the dispersion of an auxiliary non-interacting bath and $V_{k\sigma,\mu}^h$ is the hybridization matrix between the bath and the impurity cluster. The second and third terms include all the intra-cluster interaction terms. In \hat{E} we lump together the cluster hopping matrix and chemical potential, as well as the Hartree terms arising from non-local interactions between clusters. For the EHM

$$E_{\rho\zeta} = E_{\rho\zeta}^{00} + V \,\delta_{\rho\zeta} \sum_{\langle j\rho',0\zeta\rangle} \langle n_{j\rho'} \rangle, \qquad (5.11)$$

where $\langle n_{j\rho'} \rangle$ is computed by using the translational invariance of the system at the level of the superlattice.

In terms of the impurity model, the parametrization of the Weiss field function is readily obtained as,

$$\hat{\mathcal{G}}_0^{-1}(i\omega_n) = i\omega_n - \hat{E} - \hat{\Delta}(i\omega_n), \tag{5.12}$$

where the hybridization function is given by

$$\Delta_{\mu\nu,\sigma}(i\omega_n)[\epsilon_{k\sigma}, V_{k\sigma,\delta}^h] = \sum_k \frac{V_{k\sigma,\mu}^{h*} V_{k\sigma,\nu}^h}{i\omega_n - \epsilon_{k\sigma}}.$$
 (5.13)

Thus the algorithm involves determining the bath parameters $\epsilon_{k\sigma}$ and $V_{k\sigma,\mu}^h$ self-consistently, subject to the condition given by Eq. 5.7. Our implementation relies on the solution of the impurity model using exact diagonalization [59]. Starting with an inital guess for the bath parameters we obtain the cluster self energy $\hat{\Sigma}_c$, and using the self-consistency condition determine a new Weiss field, $\hat{\mathcal{G}}_0^{-1}(i\omega_n)^{\text{new}}$. In turn, this defines a new hybridization function $\hat{\Delta}(i\omega_n)^{\text{new}}$. To close the self-consistency loop we project onto a finite subspace of bath size N_b . This projection is carried out using a conjugate gradient minimization of the following distance function,

$$D = \frac{1}{(n_{\text{max}} + 1) N_b N_c} \sum_{n=0}^{n_{\text{max}}} \left\| \hat{\Delta}(i\omega_n)^{\text{new}} - \hat{\Delta}(i\omega_n)^{N_b} \right\|$$
 (5.14)

where n_{max} is the number of grid points on the Matsubara axis. Although we study the CDMFT equations only at zero temperature, the self-consistency equations are solved on the Matsubara axis.

Note: The parametrization of the bath in terms of an Anderson impurity model of the form discussed above, as we shall see below, provides a powerful tool. But it is to be noted that this parametrization is not the most general one that can be conceived. The matrix hybridization function $\hat{\Delta}(i\omega_n)$ is a function of the parameters $\epsilon_{k\sigma}$ and $V_{k\sigma,\mu}^h$. Strictly speaking, the diagonal and off-diagonal elements of this matrix are independent of each other and should be parametrized with independent variables. So the form chosen above in Eq. 5.13 makes an approximation to the most general form where $V_{k\sigma,\mu}^h$ and $\epsilon_{k\sigma}$ are matrices, rather than vectors. Without loss of generality it is always possible to diagonalize the $\epsilon_{k\sigma}$ matrix. This form for the hybridization and the underlying Anderson impurity model are given by:

$$\Delta_{\mu\nu,\sigma}(i\omega_n)[\epsilon_{k\sigma,\lambda\zeta}, V_{k\sigma,\delta\rho}^h] = \sum_k V_{k\sigma,\mu\gamma}^{h*} [i\omega_n - \hat{\epsilon}_{k\sigma}]_{\gamma\gamma}^{-1} V_{k\sigma,\gamma\nu}^h$$
 (5.15)

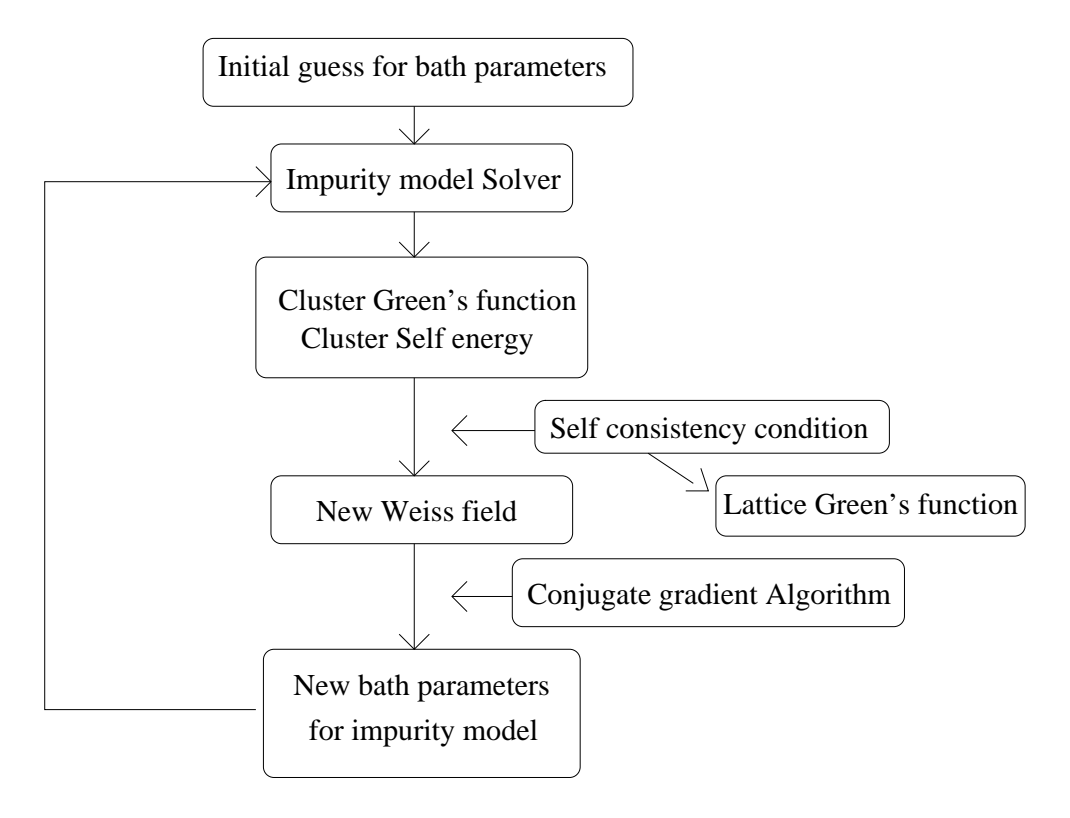


Figure 5.1: A schematic illustration of the cluster dynamical mean field algorithm

$$H_{imp} = \sum_{\mu\nu\sigma} E_{\mu\nu} c^{\dagger}_{\mu\sigma} c_{\nu\sigma} + U \sum_{\mu} n_{\mu\uparrow} n_{\mu\downarrow}$$

$$+ \sum_{\mu\nu} V_{\mu\nu} n_{\mu} n_{\nu} + \sum_{k\sigma,\gamma} \epsilon_{k\sigma,\gamma} \left[a^{\dagger}_{k\sigma,\gamma} a_{k\sigma,\gamma} + \text{h.c.} \right]$$

$$+ \sum_{k\sigma,\mu\nu} (V^{h}_{k\sigma,\mu\nu} a^{\dagger}_{k\sigma\mu} c_{\nu\sigma} + V^{h*}_{k\sigma,\mu\nu} c^{\dagger}_{\nu\sigma} a_{k\sigma\mu})$$

$$(5.16)$$

An exact diagonalization algorithm based on this parametrization involves as many baths as the number of sites on the cluster and is computationally so expensive that it is not feasible in dimensions higher than one. We restrict our study to the parametrization of the bath as specified in Eq. 5.13.

5.3 Determination of the Cluster Self Energy

The first step in the CDMFT iterative scheme is to compute the cluster self energy $\hat{\Sigma}_c$ for an initial guess of the bath parameters. This can be done using Eq. 5.7 by subtracting the inverses of the numerically determined cluster Green's function, $\hat{G}_{imp}(i\omega_n)$ from the exactly known Weiss field. Although this is accurate enough for most purposes,

when the self energy is small, it can introduce numerical errors. To deal with this, an alternative procedure was proposed in the context of the single impurity Anderson model [71]. The idea is to isolate contributions to the self energy coming purely from the hybridization and the interactions. The terms arising from the interactions can be written as ratios of correlation functions of composite operators leading to a more stable numerical procedure. We generalize this procedure to the cluster Anderson impurity model to write the self energy in the form

$$\hat{\Sigma}_c(i\omega_n) = \hat{\Sigma}_U(i\omega_n) + \hat{\Sigma}_V(i\omega_n)$$
(5.17)

where

$$\Sigma_{U\sigma}^{\mu\nu}(i\omega_n) = UF_{\sigma}^{\mu\nu'}(i\omega_n) \left[\hat{G}_{imp}^{-1}\right]_{\sigma}^{\nu'\nu}(i\omega_n)$$
 (5.18)

$$\Sigma_{V\sigma}^{\mu\nu}(i\omega_n) = K_{\sigma}^{\mu\nu'}(i\omega_n) \left[\hat{G}_{imp}^{-1} \right]_{\sigma}^{\nu'\nu} (i\omega_n)$$
 (5.19)

and

$$F_{\sigma}^{\mu\nu} = \ll c_{\mu\sigma}c_{\mu\bar{\sigma}}^{\dagger}c_{\mu\bar{\sigma}}, c_{\nu\sigma}^{\dagger} \gg \tag{5.20}$$

$$K_{\sigma}^{\mu\nu} = \sum_{\nu'} V_{\mu\nu'} \ll c_{\mu\sigma} n_{\nu'}, c_{\nu\sigma}^{\dagger} \gg$$

$$+ \sum_{\nu'} V_{\nu'\mu} n_{\nu'} \ll c_{\mu\sigma}, c_{\nu\sigma}^{\dagger} \gg \qquad (5.21)$$

Here, $\ll A, B \gg$ denotes the Green's function of operators A and B. This method of computing the self energy is particularly robust for small values of U/t, when the self energy is relatively small in magnitude, as compared to the direct approach.

5.4 Results for the Hubbard Model (V = 0)

In order to highlight the differences between the single impurity (LISA) and cluster dynamical mean field schemes, we present results obtained for the local spectral gap as a function of the onsite Coulomb repulsion U. To keep the computational cost similar, we initially fix the total number of sites in the cluster and bath, $N_s = N_c + N_b = 6$, for both schemes. The exact result for the gap is known from Bethe ansatz and is given by [72]

$$\Delta(U) = \frac{16t^2}{U} \int_1^\infty \frac{\sqrt{y^2 - 1}}{\sinh(2\pi t y/U)} dy \tag{5.22}$$

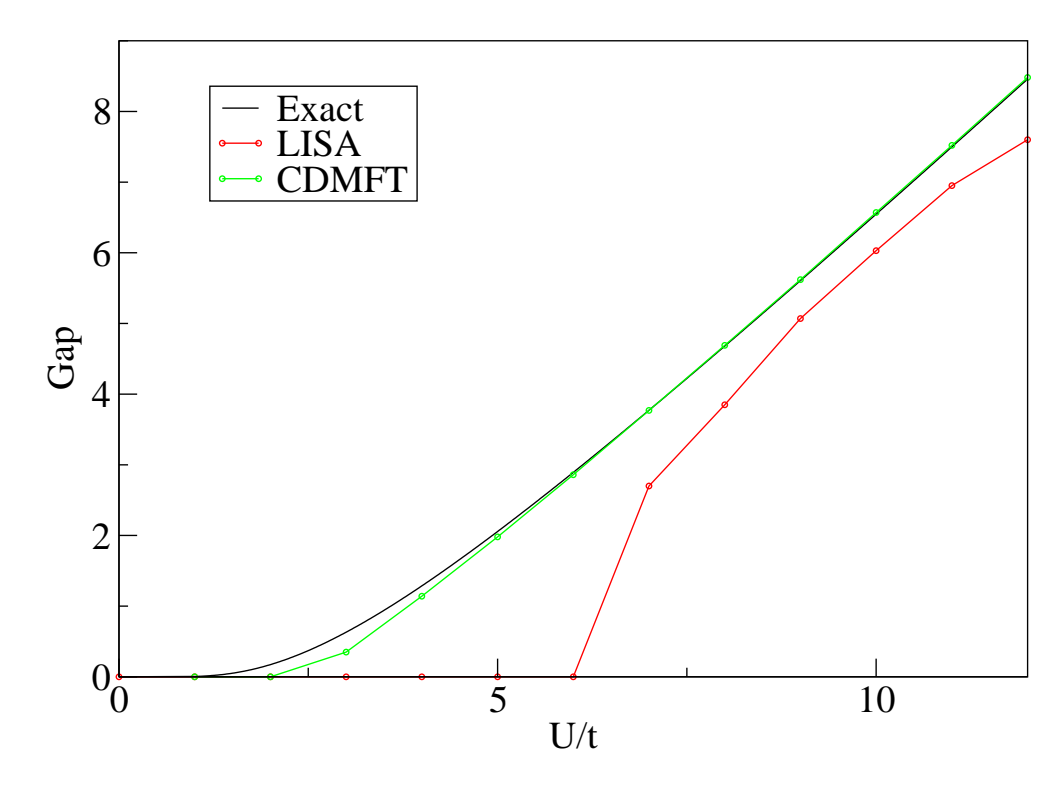


Figure 5.2: Spectral gap as a function of U/t for the half filled Hubbard model.

Fig. 5.2 shows that there is a characteristically different behavior between the single impurity $(N_c = 1)$ and cluster schemes $(N_c = 2)$. In the single impurity case, for U > 7.5t the gap follows the exact result, whereas for U < 7t it reduces to values much smaller than the exact gap and approaches zero. For the range 7t < U < 7.5t we observe a coexistence of the gapless and gapped phases. This transition from an insulating to a metallic phase is an artifact of the mean field approach which incorporates the physics of higher dimensions where the Mott transition is indeed present. On the other hand, CDMFT compares excellently to the exact gap and an insulating solution exists through all finite values of U, in agreement with the well known physics of the one dimensional Hubbard model. We measure the half spectral gap as the point where the strength of the lowest frequency pole falls to 25% of its peak height. This percentage is arrived at by requiring that the gap at strong coupling be fixed at the exact value. We also find, as expected from the cavity construction and noted recently [69], that in the case of CDMFT, the bath only couples to sites on the boundary of the cluster, whereas for

other cluster methods such as the dynamical cluster approximation (DCA), all the sites in the cluster are equivalently coupled to the bath. The self-consistent procedure is robust and generates these two different kinds of solutions regardless of the nature of the starting guess.

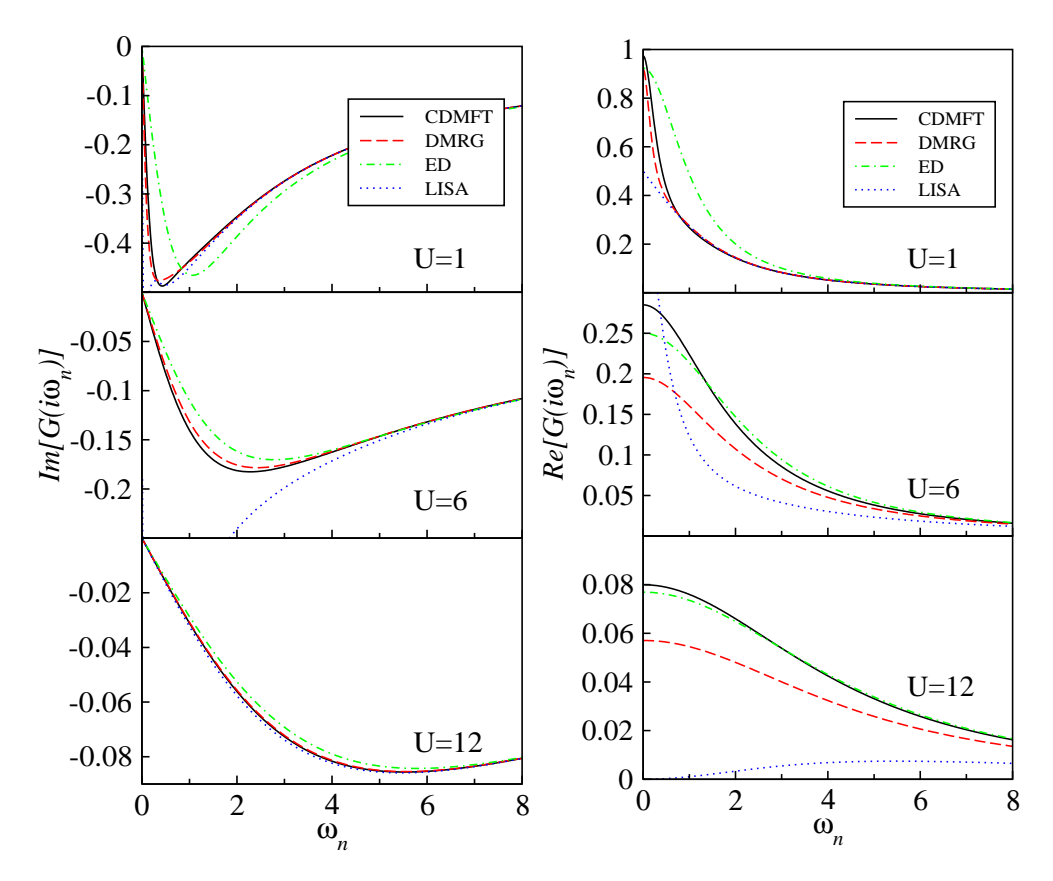


Figure 5.3: Imaginary part of the onsite Green's function (left column) and real part of the nearest neighbor Green's function (right column) on the Matsubara axis for different values of U (in units of t).

To further illustrate the performance of the CDMFT method, in Fig. 5.3 we compare the onsite as well as nearest neighbor Green's functions on the Matsubara axis to those we obtain using the DMRG method. The calculation of dynamical correlation functions within the DMRG method is carried out using the finite size algorithm [9] combined with the Lanczos vector method [12, 13]. The results shown in the figures are those for chains with 18 sites and open boundary conditions. We verify that the results are close to those found by even longer chains and hence representative of the system in the thermodynamic limit. To highlight the role of the bath within the CDMFT method,

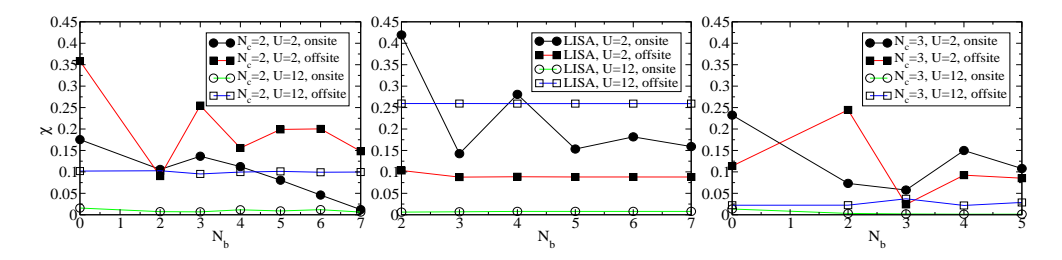


Figure 5.4: Deviation of LISA and CDMFT Green's functions from the DMRG results as a function of the bath size N_b .

we also overlay results obtained from exact diagonalization (ED) of a cluster of size $N_c=2$, but without the bath. As U decreases, we expect the difference between onsite Green's functions from the isolated cluster (ED) and the DMRG to increase, since the physics becomes less local. The contribution of the bath in CDMFT therefore becomes more significant with decreasing U and shows a systematic improvement with bath size as will be discussed later. Throughout the range of U we consider, the imaginary part of the onsite Green's function computed using CDMFT matches remarkably well with the DMRG curve. On the other hand, a comparison for the real part of the nearest neighbour Green's function shows that the self-consistent CDMFT solution achieves only a marginal improvement over the ED calculation for small U and almost none for large U. It can be clearly seen that the single impurity approach (LISA) performs poorly for the onsite Green's function for all U, except when U is large. Likewise, the nearest neighbor Green's function computed using LISA agrees poorly with the exact result throughout the entire range in U.

An important question to address is the issue of convergence and the nature of the self-consistent solution as a function of the size of the effective impurity cluster and the bath. In order to find a satisfactory self-consistent solution, we find that the size of the Hilbert space allotted to the bath has to be at least comparable to that of the cluster itself. For instance, clusters of size $N_c = 2$ require a minimum bath of size $N_b = 4$ for good convergence. Even and odd clusters show qualitatively different types of solutions, as we discuss further below. In Fig. 5.4 we plot χ , a measure of the deviation of the LISA and CDMFT solutions for the onsite and nearest neighbor Green's function from accurate results obtained using DMRG, as a function of the bath size N_b . This measure

 χ is defined as the integrated absolute difference between the CDMFT (or LISA) and DMRG Green's functions.

Let us first discuss the results for the strong coupling case (U=12t). The onsite Green's function computed using LISA compares excellently with DMRG and this continues to be so with the CDMFT method. There is practically no dependence of χ on the bath size. For the offsite Green's function, χ shows a systematic reduction with increasing cluster size, but remains fairly independent of the bath size.

For weak coupling, both LISA and CDMFT become exact. The toughest case is when U is of the order of the bandwidth; so in the following we discuss the results for U=2t. For even clusters, we find that χ for the onsite Green's function shows a systematic decrease with increasing bath size, once a minimum bath size is reached. On the other hand, χ for the offsite Green's function shows no definite trend with increasing bath size.

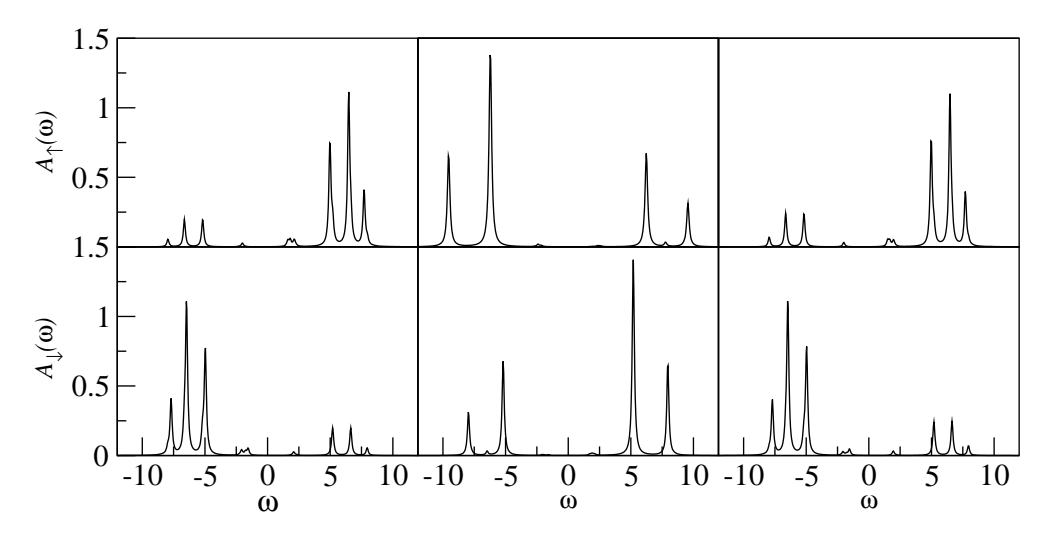


Figure 5.5: From left to right we show the local spectral functions for sites one through three in a cluster of size $N_c = 3$ with U = 12t. The bath size is fixed at $N_b = 6$.

Contrary to the expectations for a mean field solution, even cluster sizes $(N_c = 2, 4)$ show no explicit local spin symmetry breaking. Odd clusters $(N_c = 3, 5)$ show similar behavior for small bath sizes up to $N_b = N_c$. For larger bath sizes, $N_b \ge N_c$, and large enough U, the behavior of the local spectral function is spin dependent as can be seen from Fig. 5.5 for U = 12t. Odd clusters with broken symmetry are clearly inconsistent with cluster periodicty and consequently show poorer convergence. Thus, for all even

clusters and odd clusters with small enough bath sizes, the one dimensional character of the problem is dominant over the role of the bath and prevents the self-consistency from showing explicit spin symmetry breaking. On the other hand, odd clusters (we were able to test only the case $N_c = 3$) with large U and a sufficiently large bath show a symmetry broken solution consistent with the mean field approach.

The effect of the bath for $N_c = 3$ has an even more dramatic consequence at smaller U. As opposed to even clusters which correctly see only an insulating solution in one dimension, we see both a metallic and an insulating solution for $N_b \geq 5$ and $U \leq 3t$. In the region of coexistence, the metallic solution shows a better convergence than the insulating one. Thus, the improvement gained in going from LISA to $N_c = 3$ is that the region of coexistence moves to smaller U's and the insulating solution is present all the way upto U = 0. Small baths, due to the absence of enough degrees of freedom to impose a mean field character to the solution, show an insulating state throughout the range in U. Beyond $N_c = 3$ for sufficiently large odd clusters, we expect to see only an insulating solution for all U > 0.

5.5 Results for the EHM $(V \neq 0)$

In this section we study the performance of cluster mean field methods as applied to the Extended Hubbard Model. This model constitutes a natural test case since the non-local nearest neighbor Coulomb repulsion among different sites within the cluster can be accounted for exactly.

At half filling, for large enough U (strong coupling), the system goes through a first order transition from a spin density wave (SDW) to a charge density wave (CDW) ordered state at roughly V = U/2 [31,39,73]. We work in this regime, by fixing U = 12t and scanning through the nearest neighbor Coulomb repulsion V. The CDMFT method shows a clear signature of this transition with a cluster as small as $N_c = 2$. In Fig. 5.6 we report a comparison of the imaginary part of the onsite Green's function and the real part of the nearest-neighbor Green's function in the SDW phase. As seen in the V = 0 case, the comparison with DMRG is better for the former than the latter. We note

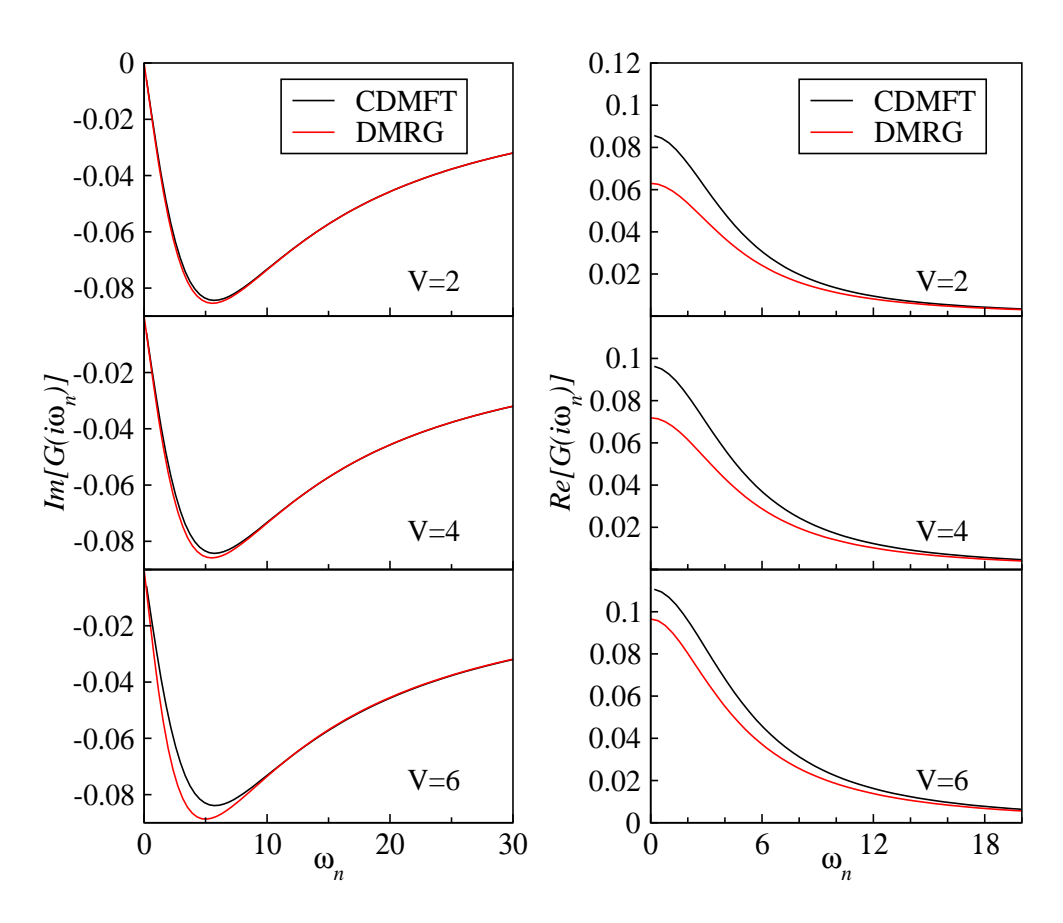


Figure 5.6: Imaginary part of the onsite Green's function (left column) and real part of the nearest neighbor Green's function (right column) on the Matsubara axis for different values of V in the SDW phase.

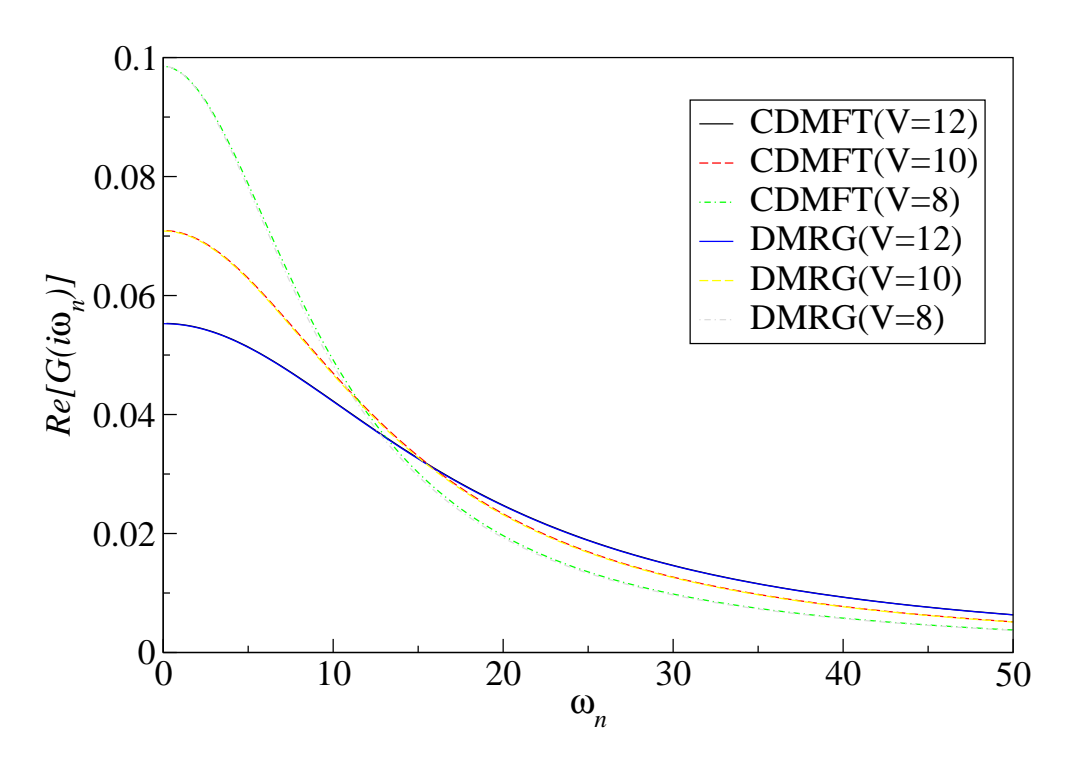


Figure 5.7: Real part of the onsite Green's function in the CDW phase.

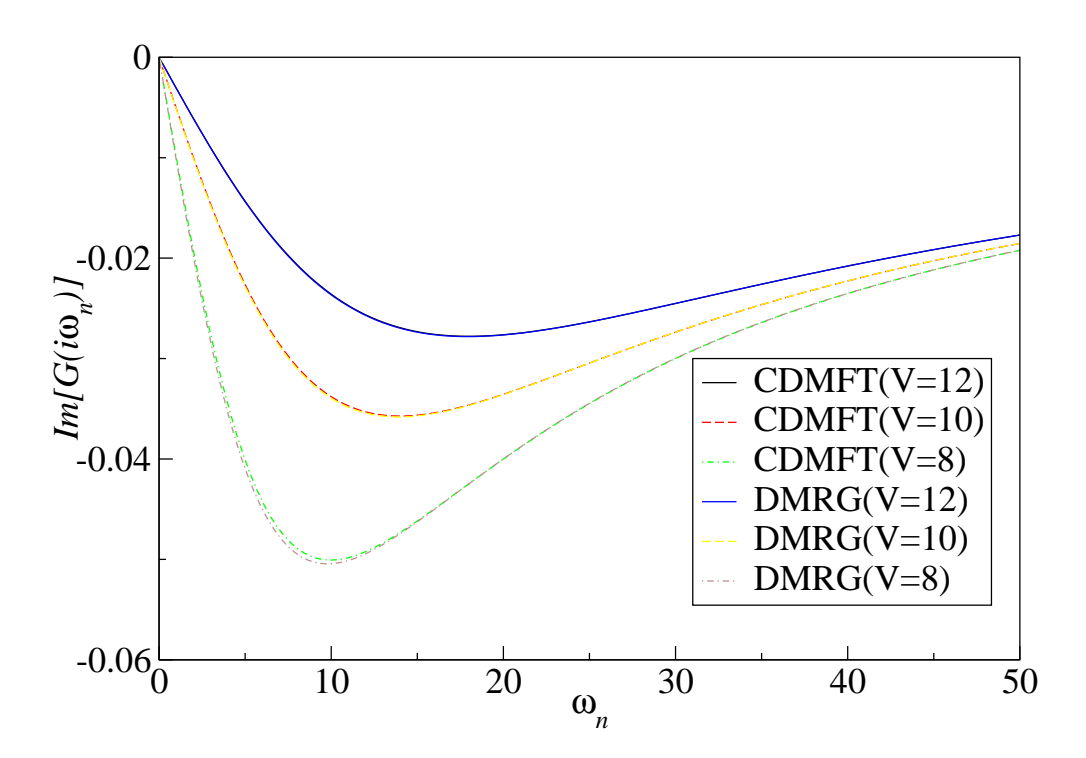


Figure 5.8: Imaginary part of the onsite Green's function in the CDW phase.

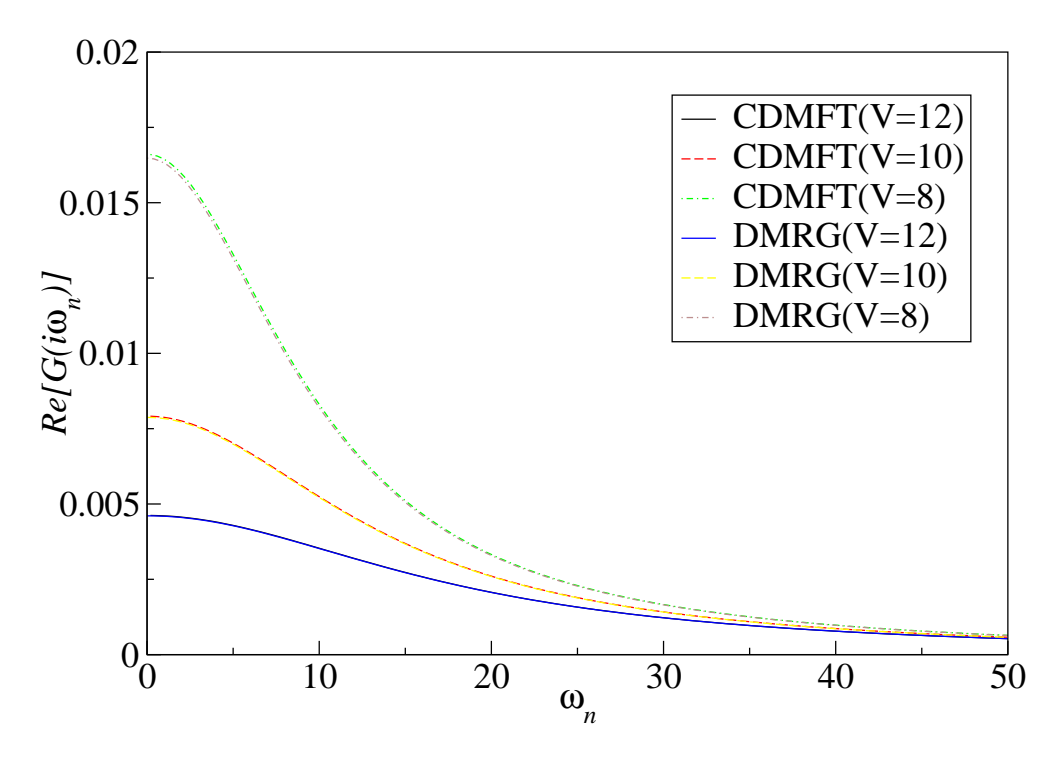


Figure 5.9: Real part of the nearest neighbor Green's function in the CDW phase.

that with increasing V the offsite Green's function compares better with the DMRG result. Figs. 5.7, 5.8 and 5.9 compare the Green's functions within the CDW phase. Across the range in V, the agreement with DMRG is so remarkable that only one set of curves are discernable within the figures. In particular, Fig. 5.7 shows the real part of the onsite Green's function which is zero in the SDW phase but acquires a non-zero value in the CDW phase. This indicates a breaking of local particle-hole symmetry of the system that is now conserved only on the average every two sites. Notice how the curves for different values of V cross, defining a characteristic scale approximately equal to U. The versatility of CDMFT in being able to treat the ordered phase stems from the fact that it only assumes supercell periodicity and consequently allows for complicated ordered states within a cell. This is in contrast to the DCA method that assumes full periodicity of the lattice, and therefore requires a fine discretization in momentum space to adequately capture the discontinuities in the Brillouin zone that appear with the emergence of short range ordered phases.

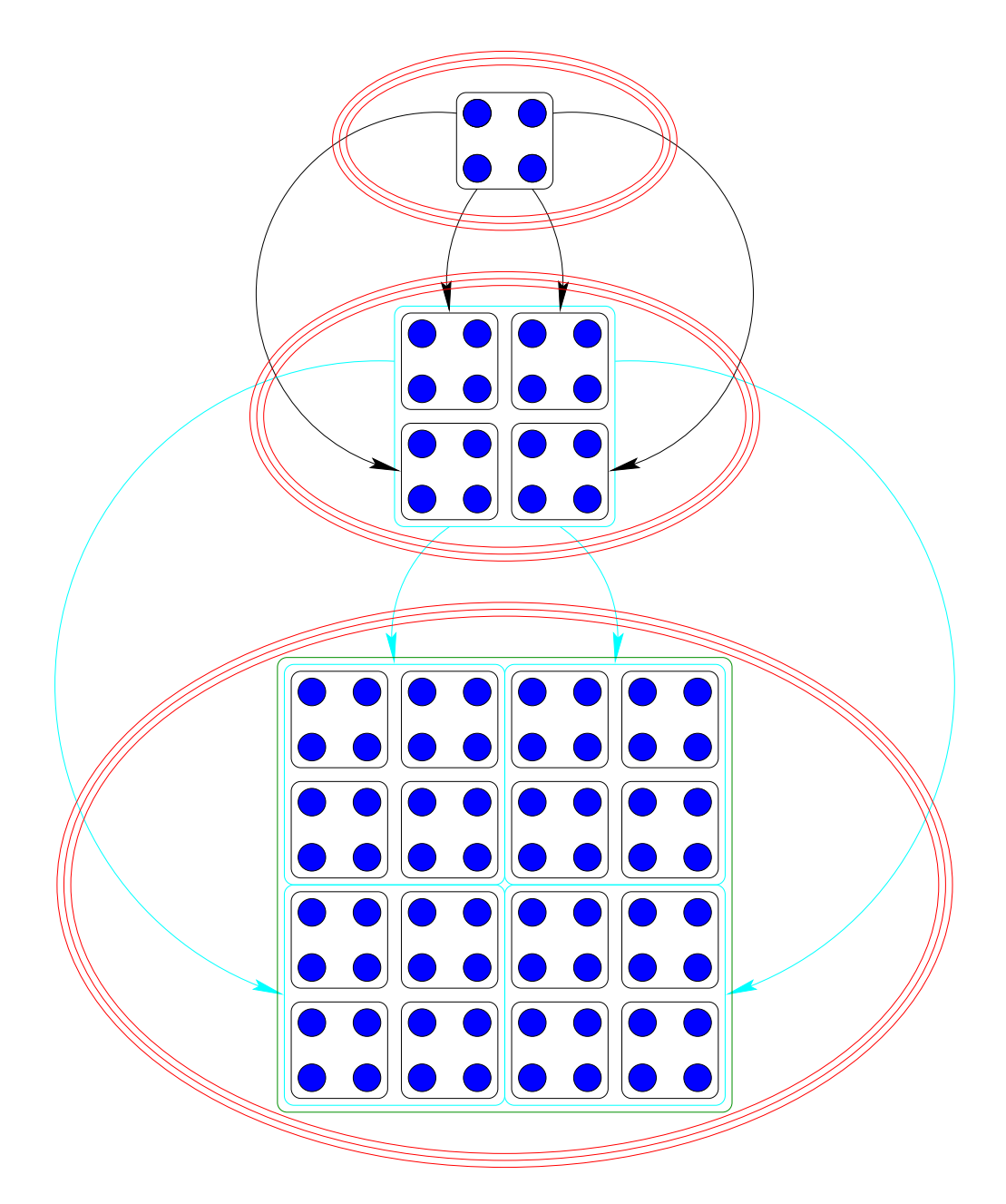


Figure 5.10: Schematic representation of an RG procedure intended to reach large cluster sizes.

5.6 Conclusions and Outlook

We have shown that the CDMFT method produces remarkably good results when tested in one dimensional systems. This is very encouraging, since one would expect mean field methods to perform even better as the dimensionality increases. We saw that even the smallest possible cluster size ($N_c = 2$) along with a self-consistent bath of modest size allows for an accurate determination of onsite correlations, while the offsite quantities improve systematically with increasing cluster size. Furthermore, the success of our extension of the CDMFT equations to describe the discrete broken symmetry of the CDW order clearly demonstrates the power of the method to incorporate short range correlations.

Following the example of the EHM, with the simplest kind of short range correlation, it should be possible to treat the physics of more complicated ordered phases as well as unit cells of realistic materials within the cellular mean field approach. The main obstacle in this program is the computational effort that goes into solving the self-consistent equations for the large clusters required by real world applications. This calls for a systematic approach that blends together cluster dynamical mean field and renormalization group ideas [5, 8, 9] to select the most relevant degrees of freedom to represent a cluster.

We suggest that the CDMFT approach can be used iteratively in complete analogy with the density matrix renormalization group approach. It is useful to compare the similarities and differences between these two methods. In both of them, one improves on the exact diagonalization of a small finite size system by embedding the small system in a larger one; an embedding which can be described by a reduced density matrix. Within DMRG the density matrix is determined by an exact diagonalization of the larger system containing the subsystem of interest. In CDMFT, one can approximate the density matrix by modelling the environment with a Gaussian Weiss field.

The CDMFT assumption of a self-consistent Gaussian bath as the environment, that one can integrate out exactly in order to define a reduced density matrix for the cluster, becomes more and more accurate as the dimensionality increases. This choice of bath is optimal in a dynamical mean field sense (optimized for the computation of the local one particle Green's function of the cluster) and sidesteps the conventional DMRG procedure for building the reduced density matrix out of a few target states. Further, the DMRG prescription [8] of selecting the states for which the reduced density matrix has the largest eigenvalues allows for a truncation of the cluster Hilbert space while retaining the relevant physical information. In Fig. 5.10 we indicate schematically how such a method would proceed by doing CDMFT on small clusters, truncating their Hilbert space using the DMRG prescription and finally using them as building blocks of even larger clusters. This procedure can be repeated until either a desired cluster size or convergence in a certain observable of interest is reached. We believe this scheme should open new vistas for numerical renormalization group calculations of realistic systems in two and three dimensions.

Chapter 6

The CDMFT Program

In this chapter we discuss a computer program to the solve the CDMFT self-consistency equations using the exact diagonalization method. We restrict ourselves to zero temperature and utilize the Lanczos method (discussed in Chapter 3) to solve the Anderson impurity model.

Apart from the routines we discuss below, one needs two programs that can be typically found in Numerical library packages such as LAPACK, NAG or Numerical Recipes. The first program is one that solves for all the eigenvalues and eigenvectors of a real symmetric tridiagonal matrix after the Lanczos step. The second program is one that can invert a general complex matrix. The main routines in our program include:

• global.f90: This module serves the purpose of making global variables available wherever needed with the command USE global. The precision of all real and complex variables in the program can be set by a single variable, which we call DBL, and is initialized here. The key parameters declared in this module include the number of sites in the cluster impurity, Nc, the number of sites on the bath, Nb and the total system size, Ns=Nc+Nb. The total z-component of the spin, S_z is a conserved quantity, and we exploit the block diagonal nature of the Hamiltonian by restricting to sectors with fixed number of up and down spin electrons, denoted by nup and ndo respectively. Nsmax denotes the maximum size of a sector for a fixed system size, Ns. Next, we define the parameters of the Hubbard Hamiltonian, the hopping t, the onsite Coulomb repulsion U, the nearest neighbor Coulomb repulsion V and finally the chemical potential mu. Hopping in real space within the cluster is stored in the array Emat (of size Nc×Nc) and in Fourier space in the array tk, defined on a grid of Nk k-points. The bath is parametrized in

terms of the site energies stored in epsi and the hybridization in Vmat. We allow for these to be determined independently for both up and down spin. Other parameters we define in this module include the maximum number of iterations in the Lanczos procedure, the CDMFT scheme and the conjugate gradient routine. The Hamiltonian is stored in the same sparse matrix notation as described in the DMRG program in Chapter 3. Lastly, we define the hybridization function (Delta and Deltret), the cluster Green's function (Gimp and Gret) and the self energy (self and selfret), on the imaginary and real frequency (retarded) axis with allocatable arrays.

- input.f90: As the name suggests, this routine is used to provide the parameters of the Hubbard Hamiltonian and the starting guess for the bath in the Anderson impurity model. Also assigned here are the values for the size of the cluster, the bath, the maximum number of iterations and tolerances for convergence for the Lanczos and CDMFT procedures, the size of the grid in k-space and on the Matsubara and real axis for the Green's functions and self energies.
- buildbasis.f90: This routine builds the set of basis states given a fixed value of S_z and a fixed system size. The basis states are represented by integers, which is explained in the following example. If we have, say, 2 sites in the cluster and 4 sites in the bath then a typical configuration with, say, 6 electrons would be:

$$\left(\left[1\otimes1\right]\left\{\otimes\ 0\ \otimes 1\otimes 1\otimes\ 0\right\}\right)_{\uparrow}\otimes \left(\left[1\otimes\ 0\right]\otimes\left\{\ 0\ \otimes\ 0\ \otimes 1\otimes\ 0\right\}\right)_{\downarrow}$$

In the above configuration, the square brackets enclose the sites on the cluster and those within curly braces represent sites on the bath. The string of 1s and 0s represent occupied and empty sites, respectively. The left half of the string represents spin-up and the right half the spin-down basis. The string of 12 spinless sites with a 0 or 1 can now be imagined to be the binary representation of an integer, by assigning weights, $(2^0, 2^1 \cdots 2^{11})$. This choice of representing a basis state as an integer is useful because the intrinsic manipulation of bits on the computer is a very fast operation and can be used to achieve highly optimized code. The basis states are sent as output by the routine buildbasis into an array

called Nstock. The sizes of different sectors are themselves stored in an array, Nstates.

- create/destroy: These routines carry out the action of a fermionic creation or a destruction operator on a given basis state. The input constitutes the location of the site, and the basis state represented by an integer. The output is again an integer and a plus or a minus sign resulting from the anticommuting nature of fermionic operators. The actual task is done quite efficiently by using the intrinsic function IBSET (in create) or IBCLR (in destroy) which either raise a bit from 0 to a 1 or lower it from a 1 to a 0 at the appropriate location. These routines are used in both building the Hamiltonian as well in obtaining the starting Lanczos vectors for constructing dynamical correlation functions.
- hamil.f90: This routine builds the Anderson impurity cluster Hamiltonian in a sparse matrix notation (refer to Chapter 3) in a sector with fixed number of up and down spin electrons. It makes calls to create and destroy to build the matrix elements of the Hamiltonian. This is optimized by the use of bit operations on the basis states which are stored as integers. The logical operator BTEST is used to check the value of a bit, to create or destroy a particle on a particular site.
- anderson.f90: This subroutine is the impurity solver. With an outer DO loop over nup and ndo, it builds the basis in a sector with fixed S_z (by calling buildbasis), then builds the Hamiltonian by calling hamil.f90, makes a call to lanczos in order to obtain the ground state eigenvalue and eigenvector in each sector and finally obtains the global ground state gsvec. For each sector, initvec is a complex random vector sent to the Lanczos routine along with the Hamiltonian to obtain the ground state evec. The ground state sector (or sectors) are stored in variables nupgs and ndogs. Once the ground state eigenvector and eigenvalue have been obtained, the next task is to build the cluster Green's function. This is performed for each ground state by calls to diagcorrel.f90 and the results are averaged over the number of ground states, ngs. The Lanczos iterations require the Hamiltonian in the appropriate sector (ground state plus or minus a particle) and hence we call

buildbasis and hamil.f90 before calling diagcorrel.f90.

• diagcorrel.f90: As the name suggests, this routine computes the impurity cluster Green's function within the continued fraction representation. To construct diagonal parts of the cluster Green's function, $\langle TA(t)A^{\dagger}(t')\rangle$, the starting vector to perform Lanczos iterations is alternately $A|GS\rangle$ and $A^{\dagger}|GS\rangle$, for the hole and particle portions, respectively. This starting vector in the program is named actors and building it requires access to both the basis states of the ground state as well as those in sectors with one less or one greater particle than the ground state. The ground state basis is stored in Nstocks and the particle or hole sector is stored in Nstock. To use a continued fraction representation for off-diagonal Green's functions of the type, $\langle AB^{\dagger}\rangle$ (suppressing the time labels for compactness of notation) as well, we construct Green's functions with suitable combinations of A and B. Therefore, if we define,

$$C = A + B$$
 , $G_C = \langle CC^{\dagger} \rangle$, (6.1)

$$D = A + iB$$
 , $G_D = \langle DD^{\dagger} \rangle$, (6.2)

then the off-diagonal Green's function, $\langle AB^{\dagger} \rangle$ can be expressed as:

$$2\langle AB^{\dagger} \rangle = G_C - iG_D - (1 - i)(G_A + G_B)$$
(6.3)

The basic operation involved in the Lanczos procedure is the multiplication of a Hamiltonian matrix with a vector. This task cannot be done by an intrinsic function of Fortran 90 such as MATMUL since the Hamiltonian is stored in sparse matrix notation. It is done by the routine atimex. The coefficients of the continued fraction expansion obtained after a fixed number of Lanczos steps, Nlanc, are stored in arrays Af and Bf and sent to the routine computegreen. This routine actually builds the Matsubara, retarded and advanced Green's functions.

• cluster.f90: This is the main program which controls the sequence of calls to other routines. The first step is to initialize the sizes of various allocatable arrays which store the cluster Green's functions, the hybridization function, the

self energy and lattice Green's functions. Since the self-consistency equations are solved on the Matsubara axis, all the above functions are defined over a grid of Nw points in imaginary frequency. The real frequency information is also stored in corresponding arrays for output. Before the call to input is made for obtaining the parameters of the Hamiltonian as well as the starting guess for a solution, the Fourier transform of the hopping matrix on the cluster, tk, is defined over a grid with Nk k-points. The parameters for a starting guess of the self-consistent solution, epsi (bath site energies) and Vmat (cluster-bath hybridization) are then obtained by a call to the subroutine input. The next step is to obtain the initial hybridization function Delta and call the subroutine anderson to solve for the ground state and impurity cluster Green's function. Subsequent to this, we build the cluster self energy using the Dyson equation. This self energy is then used in the self-consistent CDMFT equations to obtain the lattice Green's function Gloc and the new hybridization function, named Deltanew. The new hybridization function is projected onto a discrete bath using a call to the routine search. These new bath parameters are compared to the starting guess (or a previous iteration) by defining a distance, chisq. This distance, chisq, is defined as the absolute difference between the hybridization functions in consecutive CDMFT iterations. If the distance is smaller than a specified tolerance, the CDMFT selfconsistent solution has been obtained, otherwise we begin the next iteration with a call to the routine anderson with new bath parameters.

• search.f90 This is the routine responsible for the crucial task of projecting the hybridization function obtained from the CDMFT self-consistency condition in cluster.f90 onto a discretized functional subspace with a finite number of bath parameters to start a new iteration. The projection is achieved by using a conjugate gradient routine called minimize to minimize a defined distance between the discrete and continous hybridization functions on the Matsubara axis. This distance is computed by the subroutine energy. The total number of parameters (epsi and Vmat) to be varied is 2Nb(2Nc+1) and is denoted by nbparm. The actual procedure is as follows. First, the existing parameters from a previous iteration stored

in arrays epsi (of size Nb×2) and Vmat (of size Nb×2×Nc) are arranged into a one dimensional array xtemp. This is done efficiently by the intrinsic function PACK. This array xtemp is the starting guess to fit the new hybridization function and is sent as input to the routine minimize. In the subroutine minimize, xtemp is varied to minimize the distance defined in energy with a specified tolerance. The subroutine energy performs the reverse task of rearranging the one dimensional array xtemp after each conjugate gradient iteration into epsi and Vmat, using the intrinsic function RESHAPE and then computing a distance from the hybridization function to be projected. The parameters for a new CDMFT iteration are determined as a weighted average of those found by the conjugate gradient routine and the parameters from a previous iteration to increase the stability of the iterative procedure.

Chapter 7

Summary, conclusions and outlook

Many of the systems of interest in quantum-many body physics are characterized by low dimensionality and strong interaction, rendering the investigation of even the simplest models a difficult task. There is a huge dearth of analytical methods in dimensions higher than one. This circumstance has in the past decade stimulated huge advances in the development and use of computational methods for quantum many-body systems. Numerical methods have come a long way from brute force exact diagonalization of a Hamiltonian on finite clusters [1,4] to elegant renormalization group algorithms [5, 8, 9]. The density matrix renormalization group (DMRG) method and the dynamical mean field theory (DMFT) [2] are probably two of the most powerful numerical quantum many-body methods developed in the past decade and are central to this thesis. The DMRG method has been highly successful in elucidating the properties of one-dimensional quantum many-body systems. The DMFT, on the other hand, is a self-consistent mean field approximation which becomes exact in the limit of infinite dimensions. It has given new insights and predicted various qualitative trends in the redistribution of spectral weight as temperature, pressure and doping are varied in optical and photoemission experiments near the Mott transition.

In recent years, several materials have been discovered that allow the investigation of the properties of the 1D electronic state under the influence of both strong electron-lattice and electron-electron correlation. These quasi one-dimensional systems include materials such as SrCuO₂, Sr₂CuO₃, conjugated polymers and Ni halides [16–18] amongst several others. These systems, well described as Mott insulators, have remained a challenge to existing theoretical methods. Non-perturbative studies of the dynamical response in these systems have largely been restricted to the continuum limit [22,23] and

very little was known about the lattice problem. In this thesis we have presented some insights that have been obtained into the optical response, charge gap and the behavior of excitons in one-dimensional Mott insulators utilizing the DMRG method. We have used the finite size algorithm of DMRG with open boundary conditions to develop our computer program. Dynamical correlation functions were computed by targeting the appropriate Lanczos vectors. We have shown how a Mott-Hubbard exciton, a bound state between a double occupancy and an empty site in a background of singly occupied sites, can be formed in the presence of a nearest-neighbor Coulomb repulsion, V, within the one-dimensional Hubbard model [73]. We compute the current-current (optical response function) and kinetic-kinetic (Raman response function) correlators as a function of the nearest-neighbor Coulomb repulsion as the system undergoes a transition from a spin density wave (SDW) to a charge density wave (CDW) state. We also compute the local spectral function over the same range in V. Within the SDW phase, the spectral gap remains constant until a critical value of V is reached and then rapidly goes to zero near the SDW-CDW phase boundary. At V=0 the optical and Raman response functions show a broad feature representative of the Mott insulating gap centered around U. As V becomes non-zero, an excitonic feature starts to develop in both the optical and Raman response functions around the same critical value of V as in the case of the spectral function. With a further increase in V, the excitonic feature gains in optical weight, reaches a maximum and then vanishes near the SDW-CDW boundary. Although a Mott-Hubbard exciton can be described as a bound pair of excitations with opposite charges, the Coulomb interaction at the same time determines the size of the Mott gap, the exciton properties, and the coupling of the exciton to the other electrons in the system. Therefore, an increase of the Coulomb interaction strength does not simply bind the exciton more tightly, but also renormalizes the gap and couples the particlehole excitation more strongly to the other electrons. This leads to a non-monotonic behavior in the properties of the Mott-Hubbard exciton as a function of the Coulomb repulsion strength, for example, its optical weight, and even to instabilities toward the formation of charge-density wave droplets. The exciton binding energy is comparable to the optical gap itself and hence the problem is highly non-perturbative. This should be contrasted with the excitons in conventional band insulators which exhibit a monotonic behavior as a function of the Coulomb repulsion strength due to the large separation in energy scale between the band gap and the binding energy of the excitons. Due to strong correlation and low dimensionality, electrons within the 1D Hubbard model are known to decouple into new elementary excitations, namely, spinons (a chargeless spin-1/2 object) and holons (a spinless object with unit charge) [43]. This necessitates a careful treatment of the full many-body problem. The Lanczos method combined with the DMRG approach is a powerful non-perturbative tool for computing the dynamical correlation functions of a non-trivial system like this. Our numerical approach and the generality of our computer program permits us to easily include other ingredients such as explicit dimerization and interchain hopping which are present in these materials in order to allow for a detailed quantitative comparison with experiments in the future.

A closely related problem of much interest, on which the DMRG approach may shed light and which is under investigation, is that of the phase diagram of quasi-one-dimensional organic compounds TMTTF and TMTSF and their unusual metallic behavior [44–46]. These materials are believed to be quarter-filled Mott Insulators and close to the Mott transition point. By varying the anistropy of the system and the energy scale at which it is probed, a wide range of behaviors has been reported. The metallic phase shows a broad feature representative of the Mott insulating gap, carrying a majority of the spectral weight and a very narrow Drude peak. Thus, these compounds are very far from being Fermi liquids and present interesting challenges. Also of substantial interest by itself is an understanding of the dynamical properties of the quarter filled one-dimensional extended Hubbard model (EHM) and is being studied at the time of writing this thesis.

In the thesis, we have also considered the limit of infinite dimensionality, in particular, a method wherein clusters of sites are embedded in a self-consistent medium [53]. This method incorporates short range correlations, k-dependence of the self energy as well as dimensionality which are missing in the original single impurity dynamical mean field theory (DMFT) [2]. We solve the self-consistent equations for the cluster-DMFT (CDMFT) in the worst case scenario, viz., the one dimensional extended Hubbard model

using the exact diagonalization approach. We compare with DMRG and find that even the smallest possible cluster size ($N_c=2$) along with a bath of modest size provides an accurate description of the onsite correlations, while the offsite quantities improve systematically with increasing cluster size. This is very encouraging, since one would expect mean field methods to perform even better as the dimensionality increases. We also extend the CDMFT equations to describe broken symmetry and study dynamical correlations in the CDW phase to find an excellent agreement with calculations using the DMRG method. Following the example of the EHM, with the simplest kind of short range correlation, it should be possible to treat the physics of more complicated ordered phases as well as unit cells of realistic materials within the cellular mean field approach. The main obstacle in this program is the computational effort that goes into solving the self-consistent equations for the large clusters required by real world applications. This calls for a systematic approach that blends together cluster dynamical mean field and renormalization group ideas [5, 8, 9] to select the most relevant degrees of freedom to represent a cluster.

We observe that both DMRG and CDMFT involve the embedding of a finite size system in a larger one to describe the smaller system as part of the infinite lattice. Based on this, we have proposed a new approach that blends the CDMFT (derived from the limit of infinite dimensions) and the DMRG (successful in one dimension) ideas to perform calculations for realistic systems in two and three dimensions. The CDMFT assumption of a self-consistent Gaussian bath as the environment, that one can integrate out exactly in order to define a reduced density matrix for the cluster, becomes more and more accurate as the dimensionality increases. This choice of bath is optimal in a dynamical mean field sense (optimized for the computation of the local one particle Green's function of the cluster) and sidesteps the conventional DMRG procedure for building the reduced density matrix out of a few target states. Further, the DMRG prescription [8] of selecting the states for which the reduced density matrix has the largest eigenvalues allows for a truncation of the cluster Hilbert space while retaining the relevant physical information. Schematically, such a method would proceed by doing CDMFT on small clusters, truncating their Hilbert space using the DMRG prescription

and finally using them as building blocks of even larger clusters. This procedure can be repeated until either a desired cluster size or convergence in a certain observable of interest is reached. We believe this scheme should open new vistas for numerical renormalization group calculations of realistic systems in two and three dimensions.

The directions for future work with the CDMFT method are numerous and several investigations are underway. One of the problems being investigated is the nature of the spectral weight as a function of doping. The physics of the Hubbard model in two dimensions at zero temperature is a subject of intense interest and quite an open problem. We are currently studying this model at and away from half-filling. Prominent amongst the questions under investigation is whether there is a correlation driven Mott transition at half-filling as in higher dimensions. Also of interest is the nature of the spectral weight and the closing of the gap in the doped case. Following our extension of the CDMFT equations to incorporate broken symmetry, we are also investigating the competition between antiferromagnetism and d-wave superconductivity in a doped cluster in 2D.

References

- [1] E. Dagotto. Correlated electrons in high-temperature superconductors. Rev. Mod. Phys., 66:763-840, 1994.
- [2] A. Georges, G. Kotliar, W. Krauth, and M.J. Rozenberg. Dynamical mean-field theory of strongly correlated fermion systems and the limit of infinite dimensions. *Rev. Mod. Phys.*, 68:13–125, 1996.
- [3] G. Golub and C. Van Loan. *Matrix Computations*. Johns Hopkins University Press, 1996.
- [4] E.R. Gagliano and C.A. Balseiro. Dynamical Properties of Quantum Many-Body Systems at Zero Temperature. *Phys. Rev. Lett.*, 59:2999–3002, 1987.
- [5] K.G. Wilson. The renormalization group: Critical phenomena and the Kondo problem. Rev. Mod. Phys., 47:773–840, 1975.
- [6] A.C. Hewson. The Kondo Problem to Heavy Fermions. Cambridge University Press, New York, N.Y., 1993.
- [7] S.R. White and R.M. Noack. Real-space quantum renormalization groups. *Phys. Rev. Lett.*, 68:3487–3490, 1992.
- [8] S.R. White. Density matrix formulation for quantum renormalization groups. *Phys. Rev. Lett.*, 69:2863–2866, 1992.
- [9] S.R. White. Density-matrix algorithms for quantum renormalization groups. *Phys. Rev. B*, 48:10345–10356, 1993.
- [10] I. Peschel, X. Wang, M. Kaulke, and K. Hallberg (eds.). Density-Matrix Renormalization A New Numerical Method in Physics. Springer Verlag, 1999.
- [11] R.J. Bursill, T. Xiang, and G.A. Gehring. The density matrix renormalization group for a quantum spin chain at non-zero temperature. *J. Phys. Cond. Matter*, 8:L583–L590, 1996.
- [12] K.A. Hallberg. Density-matrix algorithm for the calculation of dynamical properties of low-dimensional systems. *Phys. Rev. B*, 52:R9827–R9830, 1995.
- [13] T.D. Kuhner and S.R. White. Dynamical correlation functions using the density matrix renormalization group. *Phys. Rev. B*, 60:335–343, 1999.
- [14] S. Liang and H. Pang. Approximate diagonalization using the density matrix renormalization-group method: A two-dimensional-systems perspective. *Phys. Rev. B*, 49:9214–9217, 1994.

- [15] T. Xiang. Density-matrix renormalization-group method in momentum space. *Phys. Rev. B*, 53:R10445–R10448, 1996.
- [16] Y. Mizuno, K. Tsutsui, T. Tohyama, and S. Maekawa. Nonlinear optical response and spin-charge separation in one-dimensional Mott insulators. *Phys. Rev. B*, 62:R4769–R4773, 2000.
- [17] H. Kiess. Conjugated Conducting Polymers. Springer Verlag, 1992.
- [18] H. Kishida, H. Matsuzaki, H. Okamoto, T. Manabe, M. Yamashita, Y. Taguchi, and Y. Tokura. Gigantic optical nonlinearity in one-dimensional Mott-Hubbard insulators. *Nature*, 405:929–932, 2000.
- [19] L. Sebastian and G. Weiser. One-Dimensional Wide Energy Bands in a Polydiacetylene Revealed by Electroreflectance. *Phys. Rev. Lett.*, 46:1156–1159, 1981.
- [20] A. Horvath, G. Weiser, C. Lapersonne-Meyer, M. Schott, and S. Spagnoli. Wannier excitons and Franz-Keldysh effect of polydiacetylene chains diluted in their single crystal monomer matrix. *Phys. Rev. B*, 53:13507–13514, 1996.
- [21] E.L. Lieb and F.Y. Wu. Absence of Mott Transition in an Exact Solution of the Short-Range, One-Band Model in One Dimension. *Phys. Rev. Lett.*, 20:1445–1448, 1968.
- [22] J. Voit. Phase diagram and correlation functions of the half-filled extended Hubbard model in one dimension. *Phys. Rev. B*, 45:4027–4042, 1992.
- [23] D. Controzzi, F.H.L. Essler, and A.M. Tsvelik. Optical Conductivity of One-Dimensional Mott Insulators. Phys. Rev. Lett., 86:680-683, 1998.
- [24] R.M. Fye, M.J. Martins, D.J. Scalapino, J. Wagner, and W. Hanke. Drude weight, optical conductivity, and flux properties of one-dimensional Hubbard rings. *Phys. Rev. B*, 44:6909–6915, 1991.
- [25] W. Stephan and K. Penc. Dynamical density-density correlations in onedimensional Mott insulators. Phys. Rev. B, 54:R17269-R17272, 1996.
- [26] E.R. Chalbaud and J.P. Gallinar. Wannier Stark ladders in the optical absorption spectrum of a 'Hubbard exciton'. J. Phys. C, 1:3325–3336, 1996.
- [27] J.P. Gallinar. Optical-absorption spectrum of a one-dimensional strong-coupling Coulombic Hubbard exciton. *Phys. Rev. B*, 48:5013–5020, 1993.
- [28] J.E. Hirsch. Charge-Density-Wave to Spin-Density-Wave Transition in the Extended Hubbard Model. *Phys. Rev. Lett.*, 53:2327–2330, 1984.
- [29] J.L. Cannon, R.T. Scalettar, and E. Fradkin. Ground-state phase diagram of the one-dimensional extended Hubbard model. Phys. Rev. B, 44:5995-6001, 1991.
- [30] G.P. Zhang. Ground-state phase diagram of the one-dimensional extended Hubbard model: A density-matrix renormalization-group approach. *Phys. Rev. B*, 56:9189– 9192, 1997.

- [31] M. Nakamura. Tricritical behavior in the extended Hubbard chains. *Phys. Rev. B*, 61:16377–16392, 2000.
- [32] B.S. Shastry and B.I. Shraiman. Theory of Raman scattering in Mott-Hubbard systems. *Phys. Rev. Lett.*, 65:1068–1071, 1990.
- [33] E. Jeckelmann, F. Gebhard, and F.H.L. Essler. Optical Conductivity of the Half-Filled Hubbard Chain. *Phys. Rev. Lett.*, 85:3910–3913, 2000.
- [34] F. Gebhard, K. Bott, M. Scheidler, P. Thomas, and S.W. Koch. Optical absorption of strongly correlated half-filled Mott Hubbard chains. *Phil. Mag. B*, 75:47–65, 1997.
- [35] C. Kim, A.Y. Matsuura, Z.X. Shen, N. Motoyama, H. Eisaki, S. Uchida, T. Tohyama, and S. Maekawa. Observation of Spin-Charge Separation in One-Dimensional SrCuO2. Phys. Rev. Lett., 77:4054-4057, 1996.
- [36] R. Neudert, M. Knupfer, M.S. Golden, J. Fink, W. Stephan, K. Penc, N. Motoyama, H. Eisaki, and S. Uchida. Manifestation of Spin-Charge Separation in the Dynamic Dielectric Response of One-Dimensional Sr2CuO3. *Phys. Rev. Lett.*, 81:657–660, 1998.
- [37] A. Luther. Eigenvalue spectrum of interacting massive fermions in one dimension. *Phys. Rev. B*, 14:2153–2159, 1976.
- [38] A.B. Zamolodchikov and Al.B. Zamolodchikov. Factorized S-matrices in two dimensions as the exact solutions of certain relativistic quantum field theory models. Annals of Physics., 120:253–291, 1979.
- [39] F.H.L. Essler, F. Gebhard, and E. Jeckelmann. Excitons in one-dimensional Mott insulators. *Phys. Rev. B*, 64:125119, 2001.
- [40] A.O. Gogolin, A.A. Nersesyan, and A.M. Tsvelik. Bosonization and Strongly Correlated Systems. Cambridge University Press, 1998.
- [41] S. Coleman. Quantum sine-Gordon equation as the massive Thirring model. *Phys. Rev. D*, 11:2088–2097, 1975.
- [42] A. Luther and V.J. Emery. Backward Scattering in the One-Dimensional Electron Gas. *Phys. Rev. Lett.*, 33:589–592, 1974.
- [43] Natan Andrei. Integrable Models in Condensed Matter Physics in Series on Modern Condensed Matter Physics, Vol. 6, Low-Dimensional Quantum Field Theories for Condensed Matter Physicists, S. Lundqvist and G. Morandi and Y. Lu (eds.). World Scientific, 1992.
- [44] C. Bourbonnais and D. Jerome. The normal phase of quasi-one-dimensional organic superconductors, in P. Berner. S. Lefrant and G. Bidan (eds.): Advances in Synthetic metals, Twenty years of Progress of Science and Technology, p. 206. Elsevier, New York, 1999.
- [45] D. Jerome. Organic Superconductos: From (TMTSF)₂PF₆ to Fullerenes. Marcel Dekker Inc., 1994.

- [46] S. Biermann, A. Georges, A. Lichtenstein, and T. Giamarchi. Deconfinement Transition and Luttinger to Fermi Liquid Crossover in Quasi-One-Dimensional Systems. Phys. Rev. Lett., 87:276405, 2001.
- [47] Dieter Vollhardt. Investigation of correlated electron systems using the limit of high dimensions, in Correlated electron systems vol 9., ed. by V. J. Emery. World Scientific, Singapore, 1993.
- [48] Walter Metzner and Dieter Vollhardt. Correlated Lattice Fermions in $d=\infty$ Dimensions. Phys. Rev. Lett., 62(3):324–327, 1989.
- [49] A. Georges and G. Kotliar. Hubbard model in infinite dimensions. *Phys. Rev. B*, 45:6479–6483, 1992.
- [50] M.H. Hettler abd A.N. Tahvildar-Zadeh, M. Jarrell, T. Pruschke, and H.R. Krishnamurthy. Nonlocal dynamical correlations of strongly interacting electron systems. *Phys. Rev. B*, 58:R7475–R7479, 1998.
- [51] S. Moukouri, C. Huscroft, and M. Jarrell. The Dynamical Cluster Approximation: A New Technique for Simulations of Strongly Correlated Electron Systems. arXiv:cond-mat/0004279, 2000.
- [52] A.I. Lichtenstein and M.I. Katsnelson. Antiferromagnetism and d-wave superconductivity in cuprates: A cluster dynamical mean-field theory. *Phys. Rev. B*, 62:R9283–R9286, 2000.
- [53] G. Palsson G. Kotliar, S.Y. Savrasov and G. Biroli. Cellular Dynamical Mean Field Approach to Strongly Correlated Systems. *Phys. Rev. Lett.*, 87:186401, 2001.
- [54] G. Kotliar S. Pankov and Y. Motome. Semiclassical analysis of extended dynamical mean-field equations. *Phys. Rev. B*, 66:045117, 2002.
- [55] P. Sun and G. Kotliar. Extended dynamical mean-field theory and GW method. Phys. Rev. B, page 085120, 2002.
- [56] R.J. Elliott, J.A. Krumhansl, and P.L. Leath. The theory and properties of randomly disordered crystals and related physical systems. Rev. Mod. Phys., 46:465– 543, 1974.
- [57] G. Biroli and G. Kotliar. Cluster methods for strongly correlated electron systems. *Phys. Rev. B*, 65:155112, 2002.
- [58] C. J. Bolech, S. S. Kancharla, and G. Kotliar. Cellular Dynamical Mean Field Theory for the 1D Extended Hubbard Model. *Phys. Rev. B (Accepted for publication)*, 2002.
- [59] M. Caffarel and W. Krauth. Exact diagonalization approach to correlated fermions in infinite dimensions: Mott transition and superconductivity. *Phys. Rev. Lett.*, 72:1545–1548, 1994.
- [60] G. Moeller M.J. Rozenberg and G. Kotliar. The metal-insulator transition in the Hubbard model at zero temperature. *Mod. Phys. Lett. B*, 8:535–543, 1994.

- [61] Q. Si, M.J. Rozenberg, G. Kotliar, and A.E. Ruckenstein. Correlation induced insulator to metal transitions. *Phys. Rev. Lett.*, 72:2761–2764, 1994.
- [62] Goetz Moeller, Qimiao Si, Gabriel Kotliar, Marcelo Rozenberg, and Daniel S. Fischer. Critical Behavior near the Mott Transition in the Hubbard Model. Phys. Rev. Lett., 74(11):2082–2085, 1995.
- [63] F. Ducastelle. Analytic properties of the coherent potential approximation and of its molecular generalizations. J. Phys. C, 7:1795–1816, 1974.
- [64] A. Schiller and K. Ingersent. Systematic 1/d Corrections to the Infinite-Dimensional Limit of Correlated Lattice Electron Models. Phys. Rev. Lett., 75:113– 116, 1995.
- [65] R. Chitra and G. Kotliar. Effect of Long Range Coulomb Interactions on the Mott Transition. Phys. Rev. Lett., 84:3678–3681, 2000.
- [66] R. Chitra and G. Kotliar. Effective-action approach to strongly correlated fermion systems. *Phys. Rev. B*, 63:115110, 2001.
- [67] R. Fukuda, M. Komachiya, S. Yokojima, Y. Suzuki, K. Okumura, and T. Inagaki. Novel use of Legendre transformation in field theory and many particle systems-on-shell expansion and inversion method. *Prog. Theory Phys. Suppl.*, 121:1–428, 1996.
- [68] G. Kotliar. Landau theory of the Mott transition in the fully frustrated Hubbard model in infinite dimensions. *Euro. Phys. J. B*, 11:27–39, 1999.
- [69] T.A. Maier, O. Gonzalez, M. Jarrell, and T. Schulthess. Two Quantum Cluster Approximations. arXiv:cond-mat/0207216, 2002.
- [70] J. L. Smith and Qimiao Si. Spatial correlations in dynamical mean-field theory. *Phys. Rev. B*, 61:5184–5193, 2000.
- [71] R. Bulla, A.C. Hewson, and T. Pruschke. Numerical renormalization group calculations for the self-energy of the impurity Anderson model. J. Phys. Cond. Matter, 10:8365–8380, 1998.
- [72] A.A. Ovichinnikov. Excitation spectrum in the one-dimensional Hubbard model. Zh. Eksp. Teor. Fiz., 57:2137–2143, 1969.
- [73] S.S. Kancharla and C.J. Bolech. Optical response in one-dimensional Mott insulators. *Phys. Rev. B*, 64:085119, 2000.

Vita

Srivenkateswara Sarma Kancharla

1994 Bachelor of Science in Physics,

University of Bombay, Bombay, India.

1996 Master of Science in Physics,

Indian Institute of Technology, Bombay, India.

1996 - present Graduate Studies in Condensed Matter Physics,

Rutgers, The State University of New Jersey, New Brunswick, New

Jersey, USA.

2002 Ph.D in Physics,

Rutgers, The State University of New Jersey, New Brunswick, New

Jersey, USA.

1996 - 2002 Rutgers University Teaching Assistantship.

Publications

2001 Optical response in one-dimensional Mott Insulators.

S. S. Kancharla and C. J. Bolech, Physical Review B. 64, 085119,

(2001).

2002 Cellular Dynamical Mean Field Theory for the 1D Extended Hubbard

Model.

C. J. Bolech, S. S. Kancharla and G. Kotliar, (Accepted for publica-

tion in Physical Review B).